ELECTROMAGNETIC FPCB MICROMIRROR BASED SCANNING LASER RANGEFINDER

by

Vixen Joshua Tan

Bachelor of Mechanical Engineering, Ryerson University, 2017

A thesis

presented to Ryerson University

in partial fulfillment of the

requirements for the degree of

Master of Applied Science

in the program of

Mechanical and Industrial Engineering

Toronto, Ontario Canada, 2020

AUTHOR'S DECLARATION FOR ELECTRONIC SUBMISSION OF A THESIS

I hereby declare that I am the sole author of this thesis. This is a true copy of the thesis, including any required final revisions, as accepted by my examiners.

I authorize Ryerson University to lend this thesis to other institutions or individuals for the purpose of scholarly research.

I further authorize Ryerson University to reproduce this thesis by photocopying or by other means, in total or in part, at the request of other institutions or individuals for the purpose of scholarly research.

I understand that my thesis may be made electronically available to the public.

ELECTROMAGNETIC FPCB MICROMIRROR BASED SCANNING LASER RANGEFINDER

Vixen Joshua Tan

Master of Applied Science

Mechanical and Industrial Engineering

Ryerson University, 2020

Abstract

This thesis presents an electromagnetic FPCB (Flexible Printed Circuit Board) micromirror based scanning triangulation laser rangefinder (LRF). Two configuration designs of the electromagnetic FPCB micromirror have been developed and tested. The FPCB micromirror has a large aperture (8 mm x 5.5 mm) and high flatness (ROC, radius of curvature, ~ 15m), that overcomes conventional MEMS micromirrors' limitation of small aperture (less than 5 mm). Subsequently high power lasers with large beam sizes and good collimation can be used in micromirror based scanning LRF for better performance. As a result, the LRF in this thesis achieved a larger scanning angle and longer detecting distance than those in literature. Both modelling and prototyping are presented. Three lasers (Laser 1: 2 mW; Laser 2: 20 mW; and Laser 3: 100 mW) are used to characterise the LRF. Eye-safety calculation is presented for the three lasers. Achieved performance (measurement distance and FOV, field of view) is: with Laser 1, distance of 15 – 70 cm and FOV of -15° to 10°, error ≤ 4% ; with Laser 2, distance of 15 – 130 cm and FOV of 15° to 15°, error ≤ 5%; with Laser 3, distance 15 – 200 cm and FOV of -15° to (5~9°), error ≤ 5%. Fatigue test indicates 1.2 billion scanning cycles have been reached.

Acknowledgements

Firstly, I would like to thank my supervisor Dr. Siyuan He for his full support and guidance towards my research project. He has provided me with the opportunity to explore and gather great knowledge within my research field.

Secondly, I would like to thank my fellow lab companions Devanshu, Karlmarx, Mehraz, Tim, and Trevor. They have provided me with great company and assistance during my research process.

Thirdly, I would also like to thank CMC Microsystems for their financial support and Fastline Circuits for the fabrication of my FPCB structures. Special thanks to Scott Hagen for providing generous support and encouragement towards my research and academic pursuits.

Lastly, I would like to dedicate this thesis to my mother, Ruchellie Tan, for her support throughout my entire academic career. I would also like to greatly thank her for all the sacrifices she has made for me, as the completion of my research would not have been possible without her.

Table of Contents

List of Figures

List of Tables

Chapter 1. Introduction

1.1 Laser Scanning

1.1.1 Applications

Lasers alone have limited applications such optical alignment and single spot rangefinding. The integration of a scanning mechanism with a laser has broadened the applications to include laser engraving, laser line generation, confocal microscopy, barcode scanning, scanning laser rangefinding, and many more. Laser scanners provide control over the projection of a laser spot, allowing for a greater working range that can be illuminated. Laser scanners also allow for the fast movement of a laser spot within one or two dimensions. Such characteristics are especially favorable within laser rangefinding, allowing for fast distance measurements within a greater field-of-view (FOV).

1.1.2 Laser Rangefinding (LRF)

In the case of laser rangefinding (LRF), laser scanners can be integrated with a single point LRF to increase the detectable Field-of-view (FOV) for gathering range information within an environment. This provides obstacle detection and avoidance, which allows for independent movement of robotics around an environment collision-free [1, 2]. LRF's primarily use the methods of Time-of-flight (TOF) or triangulation to measure distance [3]. TOF uses the round-trip time it takes for a laser spot to go to an object and back to the LRF device. Triangulation uses the geometric relationship between a laser, receiver, and object of interest. LRF's mainly utilize a low to high powered laser with large (≥ 5 mm) collimated beams, depending on the range to be measured. The laser spot is projected towards an object of interest and is diffusely reflected off its surface. A receiver then collects the diffusely scattered light, by means of a lens, and focuses it onto an image sensor. The Image sensor then uses the information on the collected light to generate a distance measurement. The alignment between the laser and receiver is crucial, to ensure the receiver sufficiently collects the diffusely scattered light and is detected by the image sensor. Alignment is particularly significant for triangulation LRF’s, which involve the geometry of the laser and receiver.

Scanning LRF’s are widely used within growing applications of obstacle avoidance/detection in automated guided vehicles (AGV) [4], 3D scanning [5-7], gesture recognition [8-10], and profilometry [11] (shown in Figure 1-1) . The growing popularity of laser scanners for LRF applications are constantly searching to achieve attractive features of compact size and low-cost, whilst maintain good scanning performance. The two main methods of scanning a laser are by rotation (motorized) [12-18] or oscillation (non-motorized) [10, 19, 20].

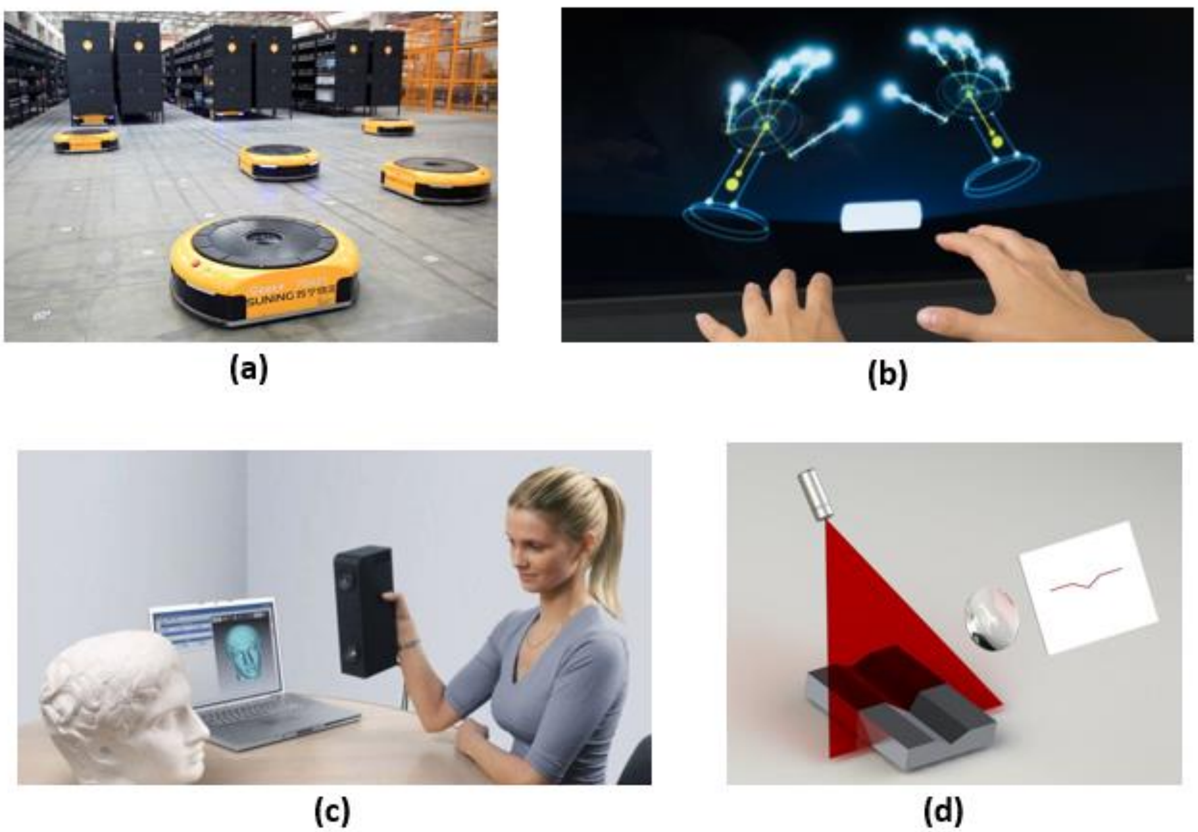

Figure 1-1: (a) Automated Guided vehicles [21] (b) Gesture Recognition [22] (c) 3D Scanning [23] (d) Profilometry [24]

1.1.3 Types of Scanners

Rotation based laser scanners involve a motor which can be used to rotate either the entire laser diode or a mountable mirror for deflection. Rotation of the entire laser involves difficult wire maintenance of the laser terminals and may result in potential damage to the laser, therefore isn't widely used. Alternatively, a motor can be used to rotate a mountable mirror, such as a polygon (multiple facets, shown in Figure 1-2) or monogon (single facet, shown in Figure 1-3) mirror, to scan an incident laser spot projected from a fixed laser. These types of scanners are commonly used within barcode scanners, CD readers, and laser printers.

Similarly, galvanometers (shown in Figure 1-4) also use a mountable mirror and motor for laser scanning, however, are bulkier in size and more expensive compared to polygon and monogon scanners. Galvanometer scanners are suited for applications that require fast, accurate, and precise laser scanning, with a relatively smaller field-of-view. Such applications include laser marking, cutting, and welding. These rotation based laser scanners are currently being used for laser rangefinding applications, however the overall size cannot be further reduced due to the limiting size of the motor.

A smaller and compact laser scanner is favored for scanning laser rangefinders, because it allows for better mobility and reduced overall size. In addition, motors require regular maintenance [25] such as the cleaning and lubrication of gears, windings, brushes, and bearings. Such maintenance results in increased costs and is required for the motor to prevent failure and perform optimally. Furthermore, the cost of the motor itself could potentially be expensive depending on the requirements of scanning performance (RPM, Torque, etc.). Other means of scanning a laser without a motor have been developed (Oscillation based), which removes the costs of regular maintenance, costs of the motor, and further reduces overall size [26, 27].

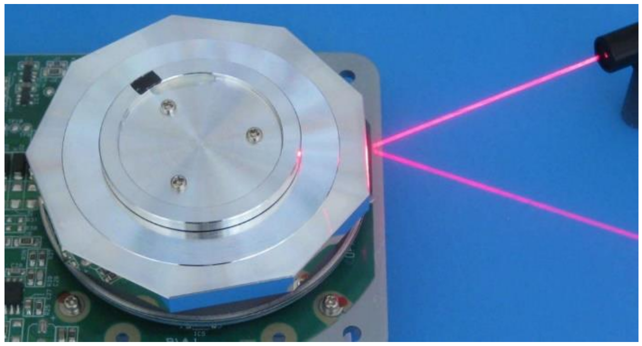

Figure 1-2: Polygon Scanner [28]

Figure 1-3: Monogon Scanner [29]

Figure 1-4: Galvanometer Scanner [30]

Oscillation based laser scanners are currently favored for their smaller and compact size, since no motor is required. Additionally, oscillation based laser scanners consists of less moving parts that require little to no maintenance, yielding a higher reliability and durability. Furthermore, non-linearity is present at high speed scanning with a motor, due to the larger moment of inertia from a mounted mass. Oscillation based laser scanners do not require a motor but instead use 1) Electrostatic (ES), 2) Magnetic (M), 3) Electromagnetic (EM), 4) Piezoelectric (PZT), or 5) Thermal actuation (T). The traditional material of silicon is primarily used for these types of scanning actuation, due to its semiconducting properties. A mirror plate is bonded or integrated to silicon-based scanning actuator, providing a reflective surface for laser spot scanning.

Microelectromechanical (MEMS) micromirrors (shown in Figure 1-5) are currently the traditional option for oscillation based laser scanners [31-34], offering the smallest size and cost-effectiveness for large unit production. MEMS micromirrors are fabricated from a limited sized silicon wafer using the photolithographic process. MEMS micromirrors with the mirror plate integrated, have difficulty in achieving a large aperture size (> 1 mm) and high surface flatness (ROC > 1 m) [35-39]. The fabrication process of an integrated large aperture (4~5 mm) mirror plate [40, 41] involves a more complex and costly fabrication process in order to maintain good mirror quality with high flatness. The production of larger aperture size MEMS micromirrors is less cost effective due to the resulting lower unit production from a limited size silicon wafer. This lower unit production from the fabrication of larger aperture mirrors results in a higher overall cost per unit, for the same fabrication process.

Alternatively, bonding of a micromirror plate onto a silicon actuator can be used to achieve a larger aperture (5~7 mm) with a high flatness, however with a low bonding yield and increased cost (e.g. >$500) [42-44]. This is due to the brittle nature of the material silicon [45], which requires careful handling. Consequently, the low bonding yield rate, results in an increase in the overall cost per unit. In the case of scanning laser rangefinding, a larger aperture size with high flatness will yield easier alignment, better measurement accuracy, better collimation, and better accommodation for high-powered large laser spot sizes [41, 46, 47]. Although MEMS micromirrors have the advantage of compact size, it doesn't offer a cost effective fabrication and bonding process in producing highly flat large aperture mirrors at high yields. Such features are ideal for laser rangefinding applications. Furthermore low cost is required for micromirror based laser rangefinders since its market is not as pronounced as other successful MEMS devices, such as the micro-accelerometer [48], micro-pressure sensor [49], and microphone [50]. Low cost has been achieved with those MEMS devices due to their extremely high volume.

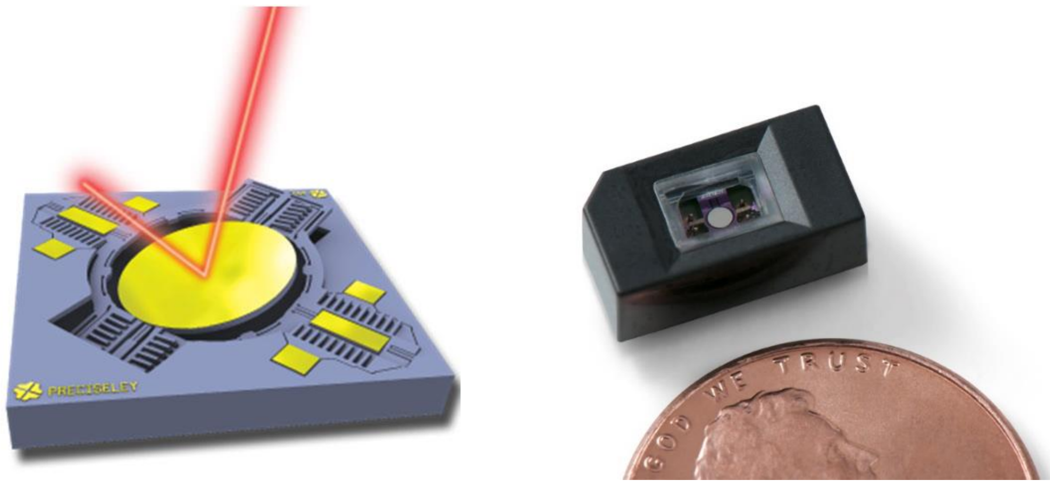

Figure 1-5: (Left) Micromirror Scanner [51] (Right) Compact Micromirror Scanner with small coin for scale [52]

Flexible printed circuit board (FPCB) micromirrors are a newly developed and proposed oscillation based laser scanner alternative, which involves easier bonding of a highly flat mirror plate onto a FPCB actuator (comprised of polyimide and copper layers). The mirror plate is fabricated independently using a simple dicing process, yielding highly flat mirrors. The fabrication of the FPCB actuator involves a mature process that is cheap and cost effective, even for low unit production. The flexible properties of the FPCB material results in a higher yield bonding compared to MEMS micromirrors. FPCB micromirrors can achieve a larger aperture, high mirror flatness, and high bonding yield, all at a low cost (especially at low volume production) [20, 39, 53-55]. FPCB micromirrors are proposed as a more suitable alternative laser scanner for the application of scanning laser rangefinding.

1.2 FPCB Micromirror

In order to address the primary limitations of MEMS micromirrors, i.e., large aperture and low cost, FPCB micromirror technology has been developed and pursued. FPCB Micromirrors have the advantage of utilizing the flexible material properties of polyimide and copper to achieve easier bonding of a micromirror plate and great scanning performance. MEMS micromirrors are primarily fabricated from silicon, which has a strain strength of < 1%, making it a brittle material. The strain strength of FPCB is 3 to 5% higher than silicon, making it less resistant to deformation during handling and bonding process of a micromirror plate. This results in a higher production yield. Moreover, the fabrication of FPCB involves a mature process that is inexpensive and cost effective, when compared to the microfabrication process of MEMS micromirrors. The FPCB fabrication process is simple and easy, primarily involving the laser cutting of a sheet of FPCB. The number of units produced and aperture size is not limited by a working area size, as in the case of MEMS micromirrors that use a limited size silicon wafer. Therefore, large aperture actuators can be fabricated using FPCB, while remaining cost efficient. The FPCB fabrication cost per unit can be as low as $10 or less, further decreasing for bulk unit production. The micromirror plate, bonded onto the FPCB actuator, is independently fabricated using a cheap and simple dicing process from a silicon wafer, which is coated for better reflectivity for a desired wavelength. Additionally, the independent fabrication of the micromirror plates yield a higher flatness when compared to integrated MEMS micromirrors, which are subjected to multiple coating and etching processes that continually degrade the quality of the micromirror. Overall when compared to traditional MEMS micromirrors, FPCB micromirrors can achieve a large aperture size with high flatness, from a low-cost fabrication and high-yield boding process.

Current FPCB micromirrors have been developed and proposed as a potential scanner for laser rangefinding. Such FPCB micromirrors are: 1) Double stage FPCB (DS-FPCB) micromirror [39] (shown in Figure 1-6) and 2) FPCB magnetic micromirror [53] (shown in Figure 1-7).

The first proposed DS-FPCB micromirror has an aperture size of 2 mm x 2 mm (square) and is capable of achieving an optical angle of ±5.4°. The overall footprint of the DS-FPCB scanner is small with dimensions of 10.3 mm × 8.8 mm × 2.0 mm. The DS-FPCB micromirror scans by using electrostatic actuation from two parallel stages (double stage), to attract and repel the FPCB actuator, bonded with a mirror plate. The parallel stages are separated from the FPCB actuator with a gap of < 1 mm, to increase the magnitude of the electrostatic force between them. To achieve the optical scan angle of ±5.4^{o}, a high driving voltage of 150 V at the resonant frequency of the mirror is needed. To achieve greater angles a higher driving voltage (>150 V) is required. Such a high voltage isn't readily available by current voltage suppliers and requires a voltage amplifier. The DS-FPCB micromirror optical scan angle is also limited by the "pull-in effect" [56], which is the eventual constant contact of the FPCB actuator plate with one of the parallel stages. This effect stops the scanning of the DS-FPCB micromirror and may potentially cause failure or damage to the FPCB actuator. The "pull-in effect" can be resolved be increasing the gap between the FPCB actuator and parallel stages, however this will require an even higher driving voltage to achieve the same angle. Furthermore, the optical angle achieved by the micromirror is too small (narrow) to provide an adequate detectable field-of-view for applications in laser rangefinding. At least an optical scan angle of ±10° or greater is desired, to provide sufficient detection of small-medium sized objects at relatively closer ranges. To avoid the need of a high driving voltage and susceptibility to the "pull-in effect" for larger optical scan angles (as in the case of electrostatic actuation), other actuation methods have been used. From all the methods of scanning actuation (mentioned in section 1.1.3), magnetism and electromagnetism provide the greatest optical scan angle potential, however with the cost of increased size from the use of permanent magnets (PM) or electromagnets (EM).

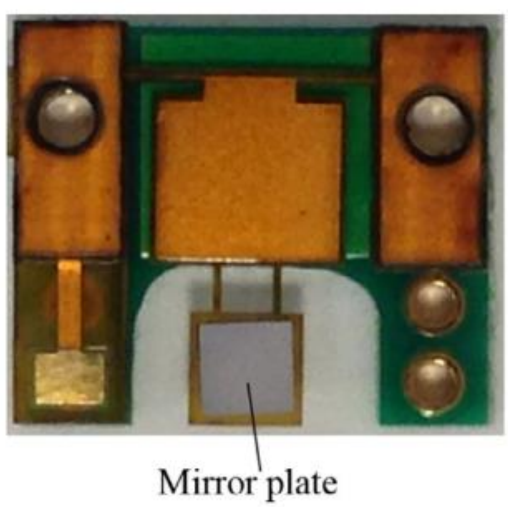

Figure 1-6: Double-Stage FPCB Micromirror [39]

The second proposed alternative is the FPCB magnetic micromirror (shown in Figure 1-7), which uses the Lorentz force to achieve a greater optical scan angle of ±13.5°. Compared to the DS-FPCB micromirror, the FPCB magnetic micromirror uses a larger aperture of 4 mm x 4 mm, beneficial for better total reflection and alignment of larger laser spot sizes. The FPCB micromirror consists of internal copper coils allowing for current to flow. The presence of two magnets on either side of the FPCB, introduces a magnetic field that rotates the FPCB micromirror (Lorentz Principle), depending on the direction of the current supplied. However, the size and optical scan angle of this FPCB micromirror scanner is limited by the required external magnets positioned on either side of the FPCB micromirror. The two external magnets result in a wider footprint of the laser scanner, which increases size and difficulty in positioning with laser rangefinding components (laser and receiver). Furthermore, the magnets limit the achievable optical angle due to the blocking of the scanned laser spot during wider optical scan angles. The potential covering of the scanned laser spot during scanning, especially at wider angles, will yield error detections within laser rangefinding applications. A wider angle is achieved using the FPCB magnetic micromirror (compared to the DS-FPCB micromirror), however the magnets results in a larger (wider) overall size and limits the achievable optical scanning angle due to blocking.

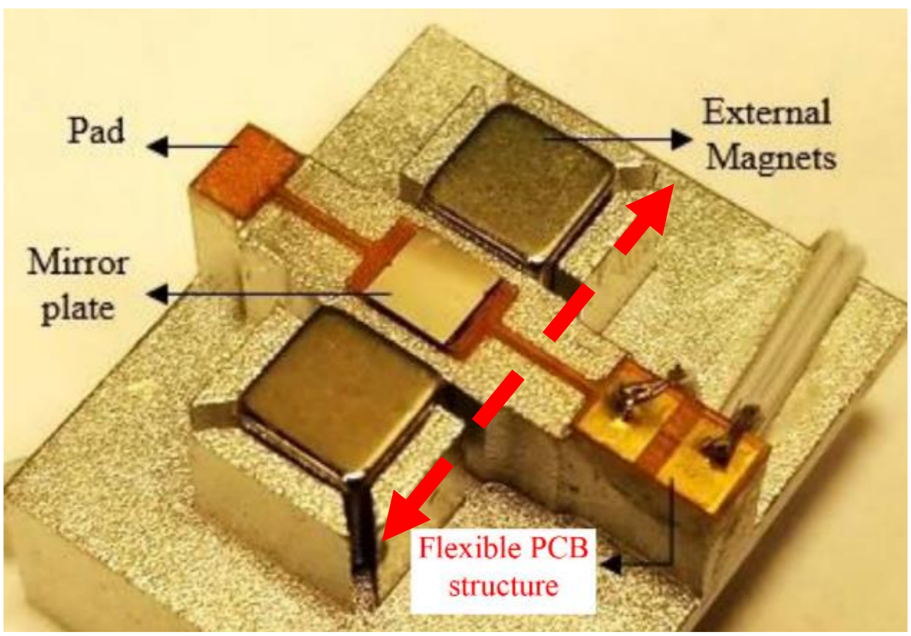

Figure 1-7: FPCB Magnetic Micromirror [51]

The DS-FPCB micromirror achieves an attractively small device footprint and slightly larger mirror aperture size (2 mm x 2mm) compared to MEMS micromirrors (< 1 mm). However, the DS-FPCB micromirror is limited to a narrow optical scanning FOV (±5.4°), which requires a very high driving voltage (≥ 150 V) for electrostatic actuation. In addition, the DS-FPCB micromirror is limited by the "pull-in effect". A FPCB magnetic micromirror has been proposed, which achieves a larger aperture (4 mm x 4 mm) and utilizes the Lorentz force to achieve a greater optical scanning FOV (± 13.5°) than the DS-FCPB micromirror. However, the FPCB magnetic micromirror has an overall larger footprint size, due to the requirement of two magnets on either side of the FPCB micromirror. The magnets pose a risk in damaging nearby electronics and also blocks the scanning laser spot when achieving a larger optical scanning FOV.

The current proposed FPCB micromirrors are limited in their achievable optical scanning FOV, due to either a high driving voltage required or the blocking of neighboring components (magnets). In the case of the FPCB magnetic micromirror, the magnets increases overall size and difficulty integrating as a laser scanner. These problems will affect the overall performance for scanning laser rangefinding applications, such as size and detectable FOV.

1.3 Objectives

The objectives of this thesis is as follows:

1) Propose and develop a FPCB micromirror with the following features:
    a. Larger optical scan angle compared to the current traditional MEMS micromirrors and developed FPCB micromirrors. Ideally, an optical scan angle of ± 15° or greater for close to resonance operation or static operation.
    b. Larger mirror aperture size (> 5 mm) with high flatness
    c. Smaller scanner device footprint, less than the developed FPCB magnetic micromirror
2) Establish the static and dynamic model of the FPCB micromirror
3) Assembly of a FPCB micromirror scanner prototype for testing
4) Application and testing of the FPCB micromirror scanner for scanning laser rangefinding

1.4 Organization

The thesis is organized as follows:

- Chapter 2 presents the design and principle of the external electromagnetic FPCB micromirror
- Chapter 3 presents the modelling of the FPCB micromirror
- Chapter 4 presents the FPCB micromirror scanner prototype
- Chapter 5 presents the scanning laser rangefinder prototype using the proposed and developed FPCB micromirror scanner porotype
- Chapter 6 presents the conclusion and future work

Chapter 2. External Electromagnet FPCB micromirror Design & Principle

2.1 Design

An external electromagnet FPCB micromirror (named EEM-FPCB micromirror hereafter) is proposed as an alternative FPCB based micromirror laser scanner. The EEM-FPCB micromirror achieves a greater optical scan angle and larger aperture size compared to both previously mentioned FPCB micromirror scanners, DS-FPCB and FPCB magnetic micromirror. In addition, the EEM-FPCB micromirror scanner achieves a smaller overall footprint compared to the FPCB magnetic micromirror scanner. The problems associated with neighboring permanent magnets and limited optical scan angles have been solved by using external electromagnets (solenoids) for scanning actuation. The external electromagnets provide great optical scanning potential and is not limited by the problems faced by other proposed FPCB micromirror scanners, i.e. a high driving voltage required, the "pull-in effect", large (wider) scanner footprint, and blocking of the scanned laser spot. The proposed EEM-FPCB micromirror still provides the advantages of the use of the material FPCB. These advantages include a larger achievable aperture size, easy and high yield bonding of the micromirror plate (high strain strength), and low-cost using a mature FPCB fabrication process. Similar to the other proposed FPCB micromirror scanners, an inexpensive low-cost dicing process is used to independently fabricate highly flat and large aperture micromirror plates, easily bonded onto the FPCB actuator with high-yield. Two configurations of the proposed EEM-FPCB micromirror have been designed, developed, and tested. Both configurations are similar in design, and the differences will be explained in this chapter. This thesis primarily focuses on the design, modelling, testing, and laser rangefinding application using the first configuration of the EEM-FPCB micromirror. The scanning performance of the second configuration has been tested with results documented in a published journal paper titled, "External Electromagnet FPCB Micromirror for Large Angle Laser Scanning". The second configuration will also be briefly explained in this chapter.

2.2 Electromagnetic Actuation

The previously mentioned FPCB micromirrors use electrostatic actuation and magnetic actuation, for the DS-FPCB and FPCB magnetic micromirrors, respectively. Electrostatic actuation is limited to small optical angles due to the required high voltage and pull-in effect. Alternatively, magnetic actuation provides greater optical scan angles by the use of Lorentz force. Magnetic actuation does not face the problem of the pull-in effect, nor does it require a high driving voltage to achieve the same or larger optical scan angle. However, magnetic actuation requires the presence of a magnetic field provided by permanent magnets. These magnets are placed on either side of the FPCB micromirror, as seen in Figures 1-6. This results in a larger footprint size for the scanner, due to the excess space required beyond the mirror plate, particularly along the width direction (shown by red arrow in Figure 1-7). Furthermore, the permanent magnets limit the achievable optical scan angle, due to the blocking of the scanning laser spot at larger angles. Also, the permanent magnets pose a magnetic hazard (unwanted attraction or repulsion) between closely integrated components (laser or screws) during application.

The EEM-FPCB micromirror uses electromagnetic actuation to solve the problem of limited optical scan angle achievable and large footprint size. A solenoid (shown in Figure 2-1) has been used to provide an electromagnetic force used to actuate the scanning motion of the FPCB structure. A solenoid produces a magnetic field controlled by the electric current supplied to tightly-packed copper helix coils wrapped around a cylindrical rod composed of a ferrous material (commonly iron). The FPCB structure alone is not affected by the solenoid's magnetic field, therefore small permanent magnet discs (≤ Ø 1.5 mm) have been bonded onto either sides of the FPCB structure. The solenoids attract and repel these bonded small magnet discs, providing rotation for scanning.

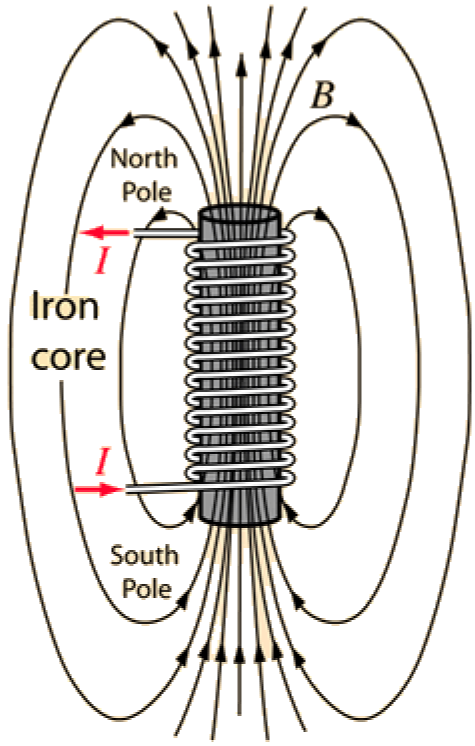

Figure 2-1: Solenoid working principle [57]

2.3 First Configuration (Copper in Torsion Beam)

The design of the EEM-FPCB micromirror scanner for the first configuration is shown in Figure 2-2. Preliminary results of the first configuration design have been reported in a conference paper for IEEE OMN 2019 [58]. Deeper study and results have been further reported in a submitted paper (under review) to the “Journal of Micromechanics and Microengineering”. Additionally, the second configuration design (described in the following section 2.4) has been reported in a published journal paper [54] in “Journal of Micromachines”. The first configuration is similar to the second configuration, except with the main difference of a copper film added in the torsion, which can be seen in Figure 2-2. The addition of a copper film within the torsion beams allowed for the flexibility of adjusting beam stiffness, ultimately determining the scanning performance of the EEM-FPCB micromirror, i.e., resonant frequency and optical scan angle. The EEM-FPCB micromirror scanner consists of the following components: FPCB structure, elliptical mirror plate, two permanent magnet (PM) discs, and two solenoids (electromagnets). The FPCB structure is made of two polyimide layers sandwiching a thin middle copper layer. The FPCB structure consists of the following sections: flame retardant 4 (FR4) clamping pads, torsion beams, and elliptical middle seat. The torsion beams serve as the rotational axis for scanning actuation and provides a connecting support between the elliptical middle seat and FR4 clamping pads. The middle seat is the area for the bonding of an elliptical mirror plate, used for laser reflection. The FR4 clamping pads are used to fasten the torsion beams onto a mechanical part. The two PM discs are bonded (using adhesive glue of Loctite 401) on the backside of FPCB structure, close to the tips of elliptical middle seat, as shown in Figure 2-2. Too large of a PM disc will result in an increase load on the FPCB scanning actuator, potentially causing it to bend or deform due to the gravitational weight of the PM discs. Therefore, the size of the PM disc was chosen to be relatively small and light having dimensions of less than 2 mm for both the diameter and thickness. A solenoid (electromagnet) is positioned directly below each of the bonded PM discs. The solenoids consist of an relatively small iron rod core (size explained in Chapter 3) wrapped with insulated thin copper coils of 0.254 mm in diameter The attractive and repulsive force produced by the solenoids on the PM discs is used to rotate the FPCB micromirror about its torsion beams, as shown in Figure 2-3.

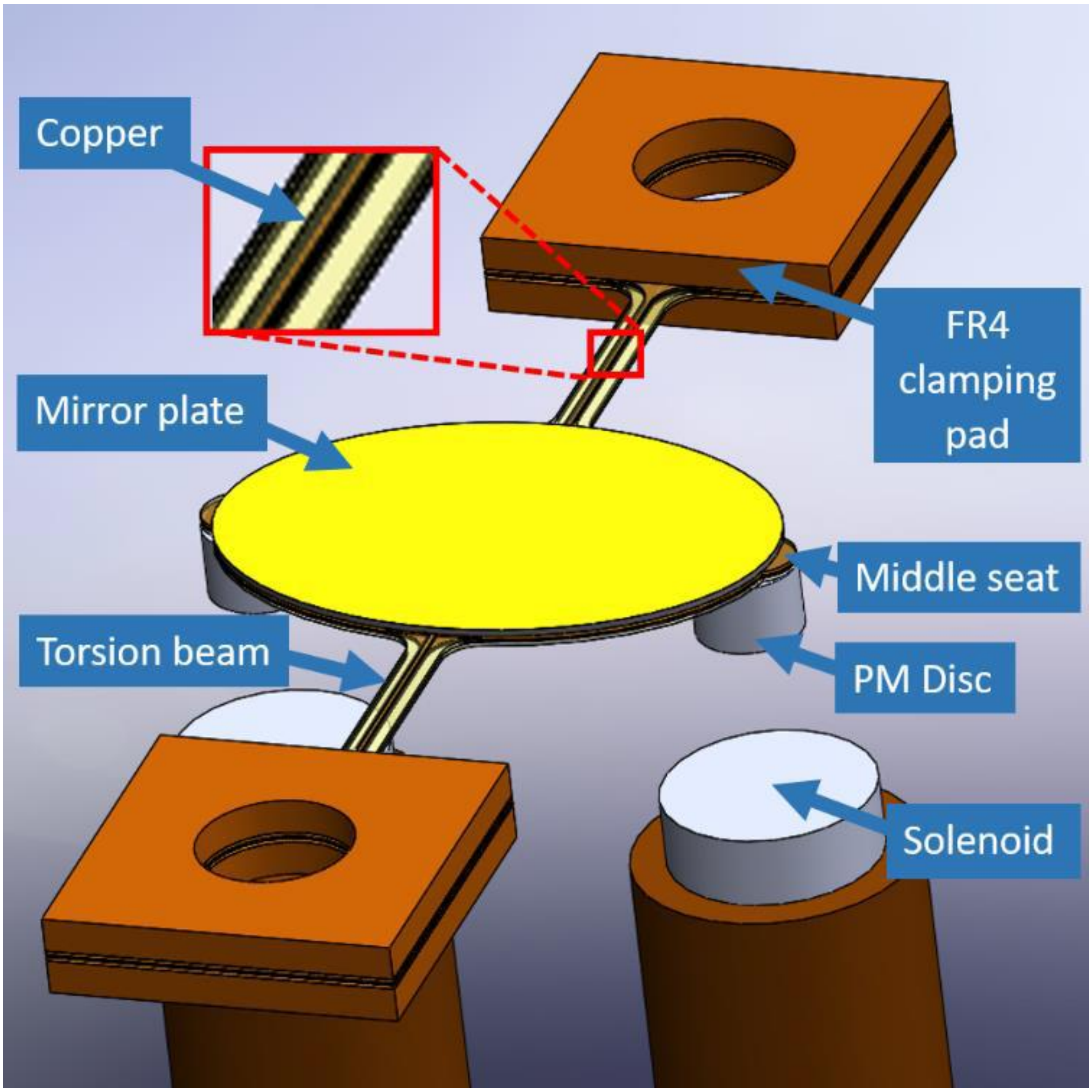

Figure 2-2 External Electromagnet FPCB Micromirror Scanner (Configuration 1)

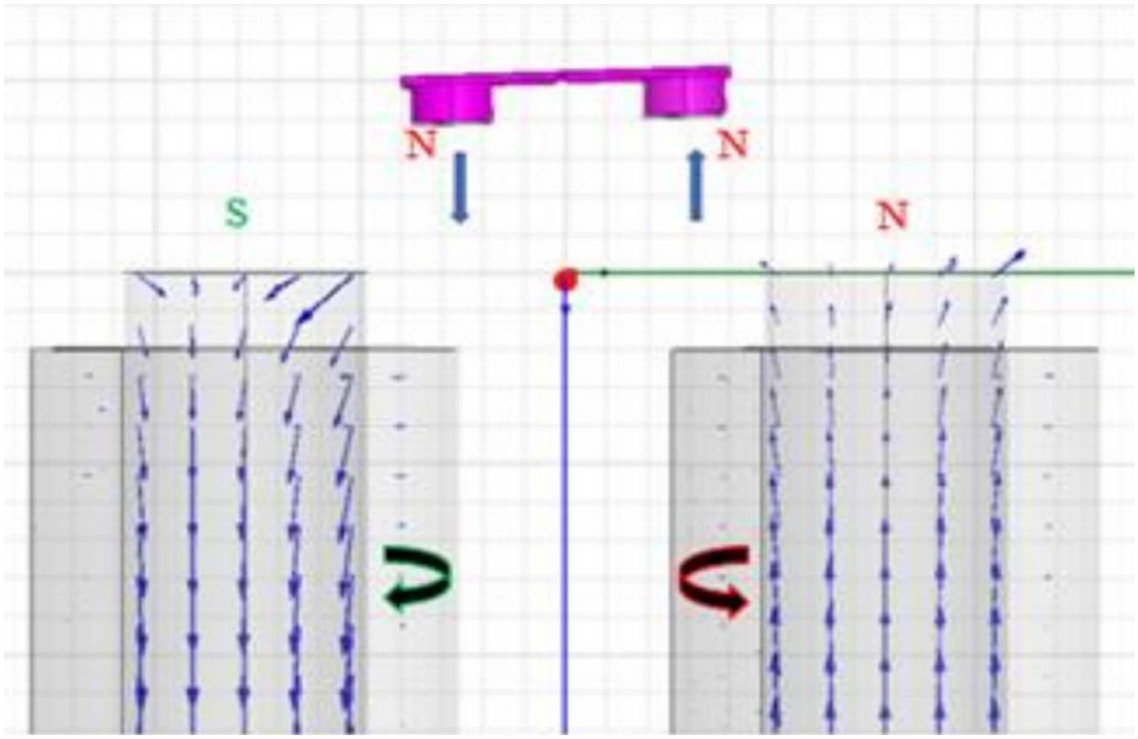

Figure 2-3: Electromagnetic scanning actuation of the EEM-FPCB micromirror [54]

Compared to the FPCB magnetic micromirror, this FPCB micromirror does not have the problem of relatively large permanent magnets blocking the scanning FOV. Instead, solenoids are placed beneath the FPCB micromirror, away from its scanning FOV. Therefore, larger optical scanning angles can be achieved without interruption and limitation. In addition, the use of solenoids poses little to no immediate magnetic hazard when placed near neighboring electronic. As opposed to the large PM magnets, which may result in damages from unexpected magnetic attraction. Furthermore, the overall footprint using solenoids results in a smaller width beyond the mirror plate, compared to the FPCB magnetic micromirror. This allows for a more compact design of the EEM-FPCB micromirror scanner and permits closer placement of additional neighboring electronics. In the case of scanning laser rangefinding, the laser and receiver can be easily placed closer to the EEM-FPCB micromirror scanner to reduce overall device size.

2.4 Second Configuration (No Copper in Torsion Beam)

The second configuration of the EEM-FPCB micromirror shown in Figure 2-4. As mentioned earlier, further results of the second configuration design can be found in a published journal [54]. The design of the second configuration is similar to the first configuration, with the main difference of the second configuration having shorter and wider torsion beams with no copper. Copper has been excluded from the torsion beams in 2nd configuration design in order to increase the achievable maximum optical angle allowable. This is due to the higher young's modulus of copper compared to polyimide (explained in Chapter 3). Copper being a stiffer material than polyimide, experiences greater stress than during rotation, thus limiting the maximum achievable rotation angle without plastic deformation. In addition, the second configuration uses larger (stronger) solenoids and smaller bonded PM discs. The differences in beam, solenoid, and PM disc dimensions will be discussed in section 3.

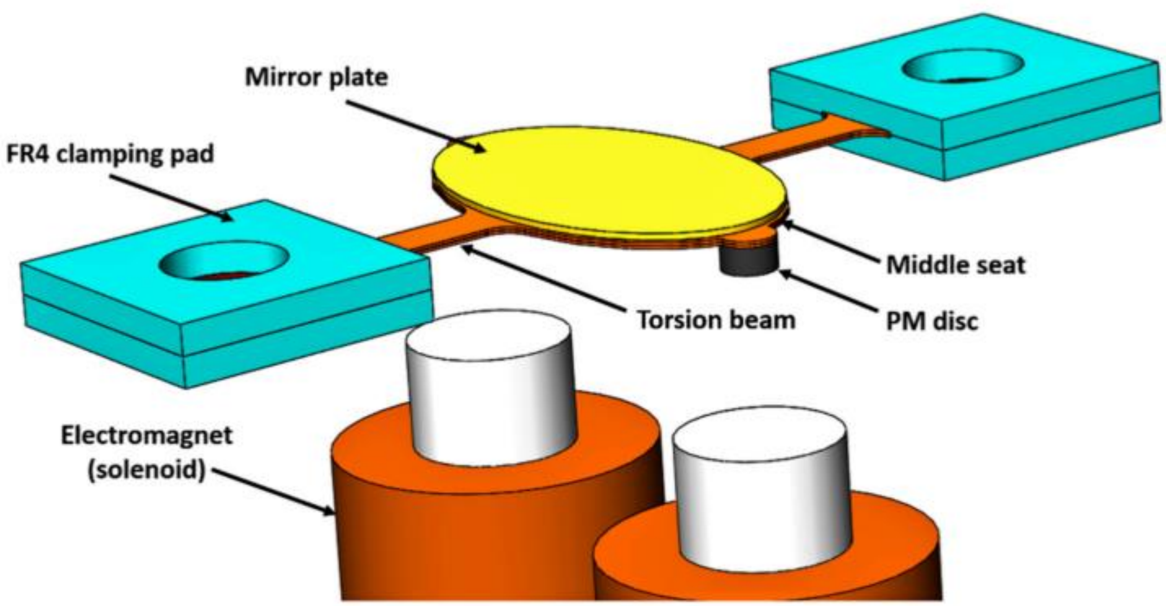

Figure 2-4: External Electromagnet FPCB Micromirror Scanner (Configuration 2)

Chapter 3. Modelling of External Electromagnetic FPCB micromirror

The program ANSYS [59] has been used for finite element analysis (FEA) to simulate the static and dynamic response of the first and second configuration of the proposed EEM-FPCB micromirror. The solenoids are the main component for generating the electromagnetic force for rotation of the EEM-FPCB micromirror. The magnitude of the electromagnetic force is influenced by the current supplied to the solenoids. This relationship is shown in Equation 1 having the following variables: Electromagnetic force in Newtons (F), Number of copper coil turns (N), Current in Amps (I), Area in m^2 (A), Permeability of air ($\mu_o = 4\pi 10^{-7}$), Relative permeability of an iron core ($k = 200$), Gap between solenoid and ferromagnetic material in meters (g). The rotation of the EEM-FPCB micromirror is indirectly related to the current supplied to the solenoids. However, for practical testing, voltage is more convenient to supply and regulate than current. Thus, voltage has been used to model the response of the rotational response of the EEM-FPCB micromirror. The static response simulation will show the relationship of the optical angle of the micromirror with respect to voltage supplied. The dynamic simulation response will show the resonant frequencies (Modes) of the EEM-FPCB micromirror.

$$F = \left(\frac{(N \cdot I)^2 \cdot k \cdot \mu_o \cdot A}{2 \cdot g^2}\right) \tag{1}$$

The primary focus of this thesis is on the design and application of the first configuration. Both configurations will follow the same modelling process and parameters which will be further elaborated within this chapter. The modelling results of the first configuration will be mainly discussed and the second configuration will be briefly summarized.

3.1 Parameters of the EEM-FPCB micromirror

The FPCB structure is primarily composed of two polyimide sandwiching a copper layer. The respective thicknesses of the polyimide and copper layers are 57 µm and 36 µm. The bonded micromirror plate is elliptical in shape with dimensions of 8 mm x 5.5 mm x 0.1 mm. The elliptical micromirror plate is coated (on one side) with a layer of 100 nm of gold, which provides excellent reflectivity (≥ 98%) for infrared wavelengths (≥ 700 nm) [60]. The relatively thin gold-coating (nanometers) on the elliptical micromirror plate has been ignored within simulation, due to its insignificant contribution to overall mass. The FR4 clamping pads are 5 mm x 5 mm x 0.5 mm, and have been modelled as the fixed boundary conditions of the EEM-FPCB micromirror for both static and dynamic simulations. The only differences between the designs of both configurations (1st and 2nd) are beam layering, beam size, solenoid size, and PM disc size. These differences are listed in Table 1. These differences are further illustrated in *Figure 2-2* and Figure 2-4, for the 1st and 2nd configuration respectively.

Table 1: Design differences between the 1st and 2nd configuration

	1st Configuration	**2nd Configuration**
Copper beam	4 x 0.1	N/A
Polyimide beam	4 x 0.5	3 x 1
Solenoid	Ø 4 x 19 (534 coil turns)	Ø 6 x 19 (1600 coil turns)
PM disc	Ø 1.5 x 1	Ø 1 x 1

The torsion beams of the FPCB structure consist of a polyimide layer and, depending on the design configuration, with or without a sandwiched copper layer. The 1st configuration has a slimmer and longer polyimide beam, which contains a thin sandwiched copper layer between the two polyimide layers of the torsion beam. A copper layer within the polyimide beams was not added in the 2nd configuration. These design changes in the torsion beam composition (Copper or No Copper) and size (Length and Width) have been made to adjust the torsion beam stiffness, thus changing the static and dynamic response of the EEM-FPCB micromirror. Furthermore, a stiffer beam would yield a higher resonant frequency and require a higher driving voltage for the same rotational angle.

The solenoid and PM disc size also differ between the 1st and 2nd configuration. The 1st configuration uses smaller solenoids (in terms of diameter) and a slightly larger PM disc, to compensate for a weaker solenoids. The 1st configuration solenoid (smaller solenoid) consists of

534 turns of copper coils and has a resistance of 29 Ω. The second configuration solenoids (bigger solenoids) consists of 1600 copper wire turns and has a resistance of 87 Ω.

The densities used for copper, polyimide, micromirror plate and PM disc of the FPCB micromirror structure are 8970 ${}^{kg}/_{m^3}$, 1420 ${}^{kg}/_{m^3}$, 2330 ${}^{kg}/_{m^3}$, and 7500 ${}^{kg}/_{m^3}$ respectively. The respective Young's Modulus used for copper and polyimide are 110 GPa and 4 GPa. Lastly, the Poisson ratio used for both copper and polyimide is 0.34. The copper wire used for the coils in both solenoids is AWG #30 and has a maximum current rating of 0.142 A [61]. Therefore, the maximum allowable voltage that can be supplied to the 1st and 2nd configuration solenoids are 4.1 V and 12.4 V respectively. The maximum current rating for the copper wire is the limit before overheating of the wire occurs, causing melting and damage of the insulation or conductor. The effects of inductance from current flow within the solenoids have been ignored, since the solenoids will be driven at relatively high frequencies (≥ 100 Hz).

3.2 First Configuration

3.2.1 Static Performance

The static rotation angle of the EEM-FPCB micromirror is actuated by the electromagnetic force generated by the solenoids, which is controlled by a voltage supply. The static performance of the EEM-FPCB micromirror will be simulated showing the relationship between voltage supplied to the solenoids and optical scan angle of the FPCB micromirror. The two solenoids will be supplied with a driving voltage with opposite polarity, resulting in each of the solenoids having opposite magnetic fields at all times. Furthermore, the PM discs are bonded beneath the FPCB structure such that their magnetic poles (north and south) face the same direction (shown in Figure 2-3). Therefore, each PM magnet disc will experience the opposite electromagnetic force (attraction or Repulsion) than the other PM disc, thus producing torque for scanning actuation.

The repulsive force of the solenoids will always be weaker compared to the attractive force experienced by the PM discs. This is due to the inverse square relationship of distance between the solenoids and PM discs have with the strength of the electromagnetic force. This unequal attraction and repulsion of the PM magnet discs will cause rotation of the FPCB micromirror with translation (towards the solenoids). Translation during rotation for the 1st configuration of the EEM-FPCB micromirror has been simulated using a driving voltage of 5 V for an initial offset of 2 mm and 3 mm between the PM discs and solenoids. The initial offset is the distance between the solenoid and PM disc before rotation of the FPCB micromirror.

Table 2 shows the attractive and repulsive force experienced by the PM discs from the solenoids for a driving voltage of 5 V for initial offsets 2mm and 3 mm. Furthermore, the optical angle achieved, translation of the FPCB micromirror, and relative change of the FPCB micromirror offset are shown in Table 2. Since the attraction force is always greater than the repulsive force, the translation of the FPCB structure is always going to be towards the solenoids. Simulations show that the translation during rotation of the FPCB micromirror is significantly smaller than the initial offset and considered negligible. Therefore, pure rotation (without translation) of the FPCB micromirror can be assumed during simulations.

The following steps have been used in determining the static response of the FPCB micromirror. The 1st step involves obtaining a graph relation between the pure mechanical rotation angle of the FPCB micromirror and the required torque. This step utilizes the ANSYS workbench for static structural analysis. The 2nd step involves obtaining a graph relation between the mechanical rotation angle of the FPCB micromirror and the required torque, for a given voltage supplied to the solenoids with the PM discs positioned according to the mechanical rotational angle. This step utilizes ANSYS Maxwell for electromagnetic field simulations. The 3rd and last step involves finding the intersections or interpolated points between the two graph curves obtained from steps 1 and 2. Finally, from step 3, a graph of the relation between mechanical rotation angle of the FPCB micromirror and voltage is generated. The previously mentioned 3 steps are used in determining the response of driving voltage and mechanical rotation angle of the first configuration of the EEM-FPCB micromirror. The results for the 1st step are tabulated in Table 3 and illustrated by a graph shown in Figure 3-1. The results for step two are tabulated in Table 4 and illustrated by a graph shown in Figure 3-2.

Table 2: Translation during rotation of the 1st configuration FPCB micromirror

Voltage (V)	5	5
Offset (mm)	2	3
Attractive Force (mN)	12.73	5.96
Repulsive Force (mN)	6.59	4.38
Translation (μm)	6.6	25.7
Optical rotation angle (º)	28	15
Relative change of initial offset due to translation (%)	0.22 %	1.29 %

Table 3: Results of pure mechanical rotation and required torque

Pure Mechanical Rotation Angle (º)	**Torque (mN*mm)**
0	0
0.5	2.8
1	5.5
2	11.0
3	16.5
4	21.9
5	27.4
6	32.9
7	38.4
8	43.8
9	49.3
10	54.8

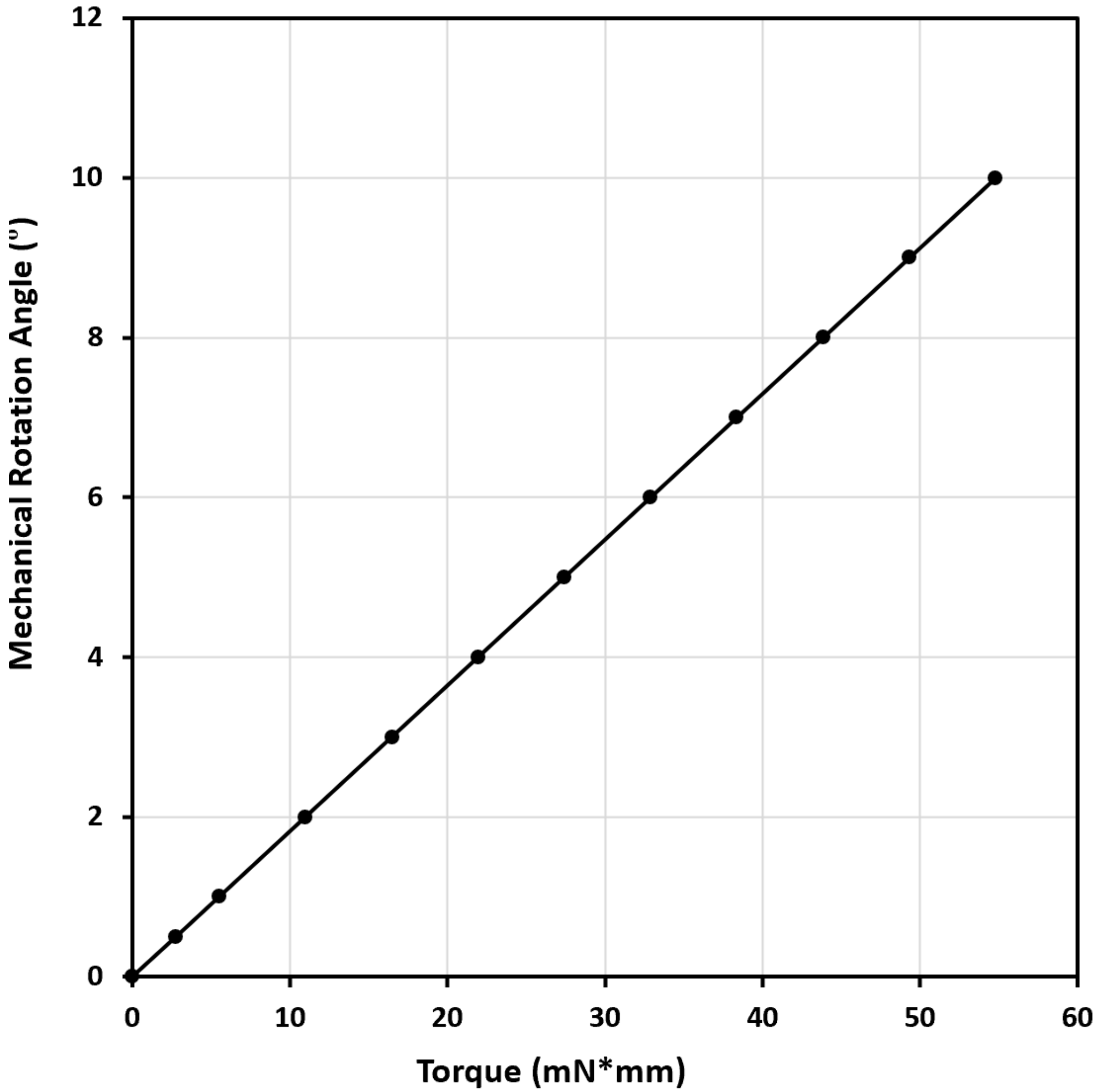

Figure 3-1: Graph of pure mechanical rotation versus Torque

Table 4: Results of Mechanical rotation angle and torque produced from the electromagnetic field of the solenoids for a specific driving voltage

Mechanical Rotation Angle (º)	**Torque (mN*mm)**							
	Using 0.58 V	**Using 1.16 V**	**Using 1.74 V**	**Using 2.32 V**	**Using 2.9 V**	**Using 3.48 V**	**Using 4.64 V**	**Using 5.8 V**
0.5	4.5	8.9	13.6	17.3	21.4	24.2	30.6	41.7
1	4.8	9.2	13.7	17.3	21.6	25.1	31.0	42.4
2	5.2	9.3	13.7	17.7	21.9	26.0	32.4	43.2
3	5.3	9.8	13.5	18.2	22.0	27.0	33.6	44.2
4	5.7	10.1	13.8	18.4	22.7	28.0	35.4	45.2
5	6.3	10.6	14.8	19.1	23.4	29.2	36.2	46.3
6	6.9	11.2	16.0	19.8	24.0	30.0	37.4	47.0
7	8.0	12.2	18.1	21.0	25.4	30.8	38.4	49.2
8	8.6	13.2	19.9	22.0	26.5	31.6	38.6	49.6
9	9.6	14.4	21.8	23.2	27.8	32.6	39.4	50.4
10	10.7	15.3	23.5	24.4	28.9	33.1	40.2	51.7

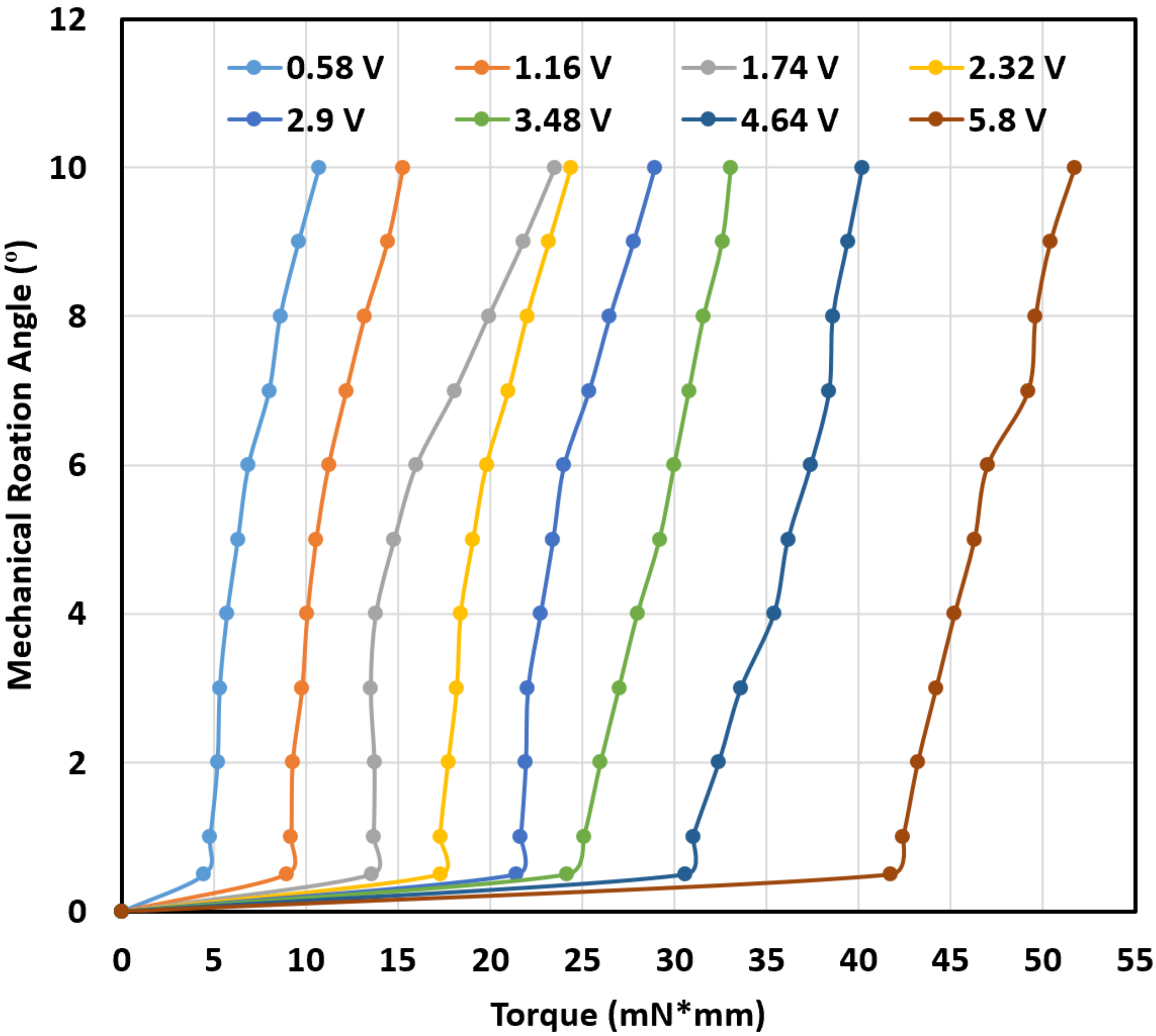

Figure 3-2: Graph of mechanical rotation angle versus torque for a specific solenoid driving voltage.

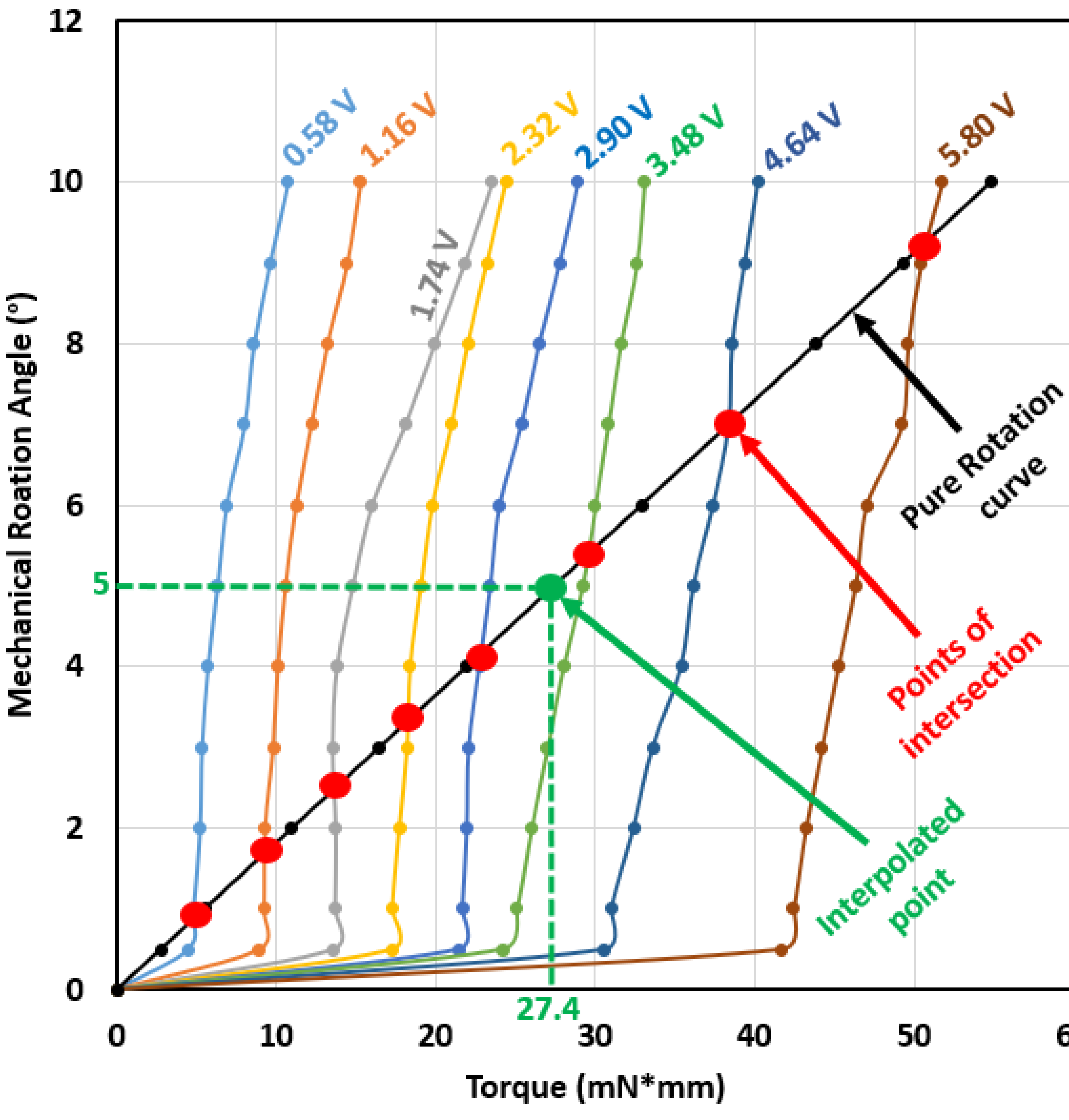

Figure 3-3 Graph of both curves from graphs shown in Figure 3-1 and 3-2, with the intersections from both curves shown by red circles

The points of intersection between curves obtained from step 1 and 2 are shown in Figure 3-3 with red circles. Interpolation was used to determine the voltage for a mechanical angle falling in-between two curves with different respective driving voltages, shown as a green circle in Figure 3-3. The following equation is used for interpolation,

$$V = V_{lower} + \left(\frac{T_{middle} - T_{lower}}{T_{upper} - T_{lower}}\right)\left(V_{upper} - V_{lower}\right) \qquad (2)$$

Table 5: Results of Optical rotation angle and corresponding required driving voltage.

Optical rotation angle (°)	Driving Voltage (V)
-12	-3.93
-10	-3.30
-8	-2.79
-6	-2.11
-4	-1.38
-2	-0.67
0	0
2	0.67
4	1.38
6	2.11
8	2.79
10	3.30
12	3.93

The green circle shown in Figure 3-3 shows the pure mechanical rotation angle of 5° with a required torque of 27.4 mN*mm (T_{middle}), which falls between curves of driving voltages 3.48 V (V_{upper}) and 2.90 V (V_{lower}) with respective torques of 29.2 mN*mm (T_{upper}) and 23.3 mN*mm (T_{lower}). Using equation 2 and the mentioned corresponding values, the voltage required to achieve a mechanical rotation angle of 5° is calculated to be 3.3 V. Table 5 shows the calculated values of voltage for a corresponding optical rotation angle using Equation 2 and Tables 3 & 4. The optical rotation angle is double (2x) the mechanical rotation angle. Only positive mechanical rotation angles have been considered in Tables 3 and 4. Due to rotational symmetry, the negative mechanical rotation angles have been determined as having the opposite driving voltage as the positive mechanical rotation angle of equal magnitude, i.e., 3.3 V to achieve 5° and -3.3 V to achieve -5°.

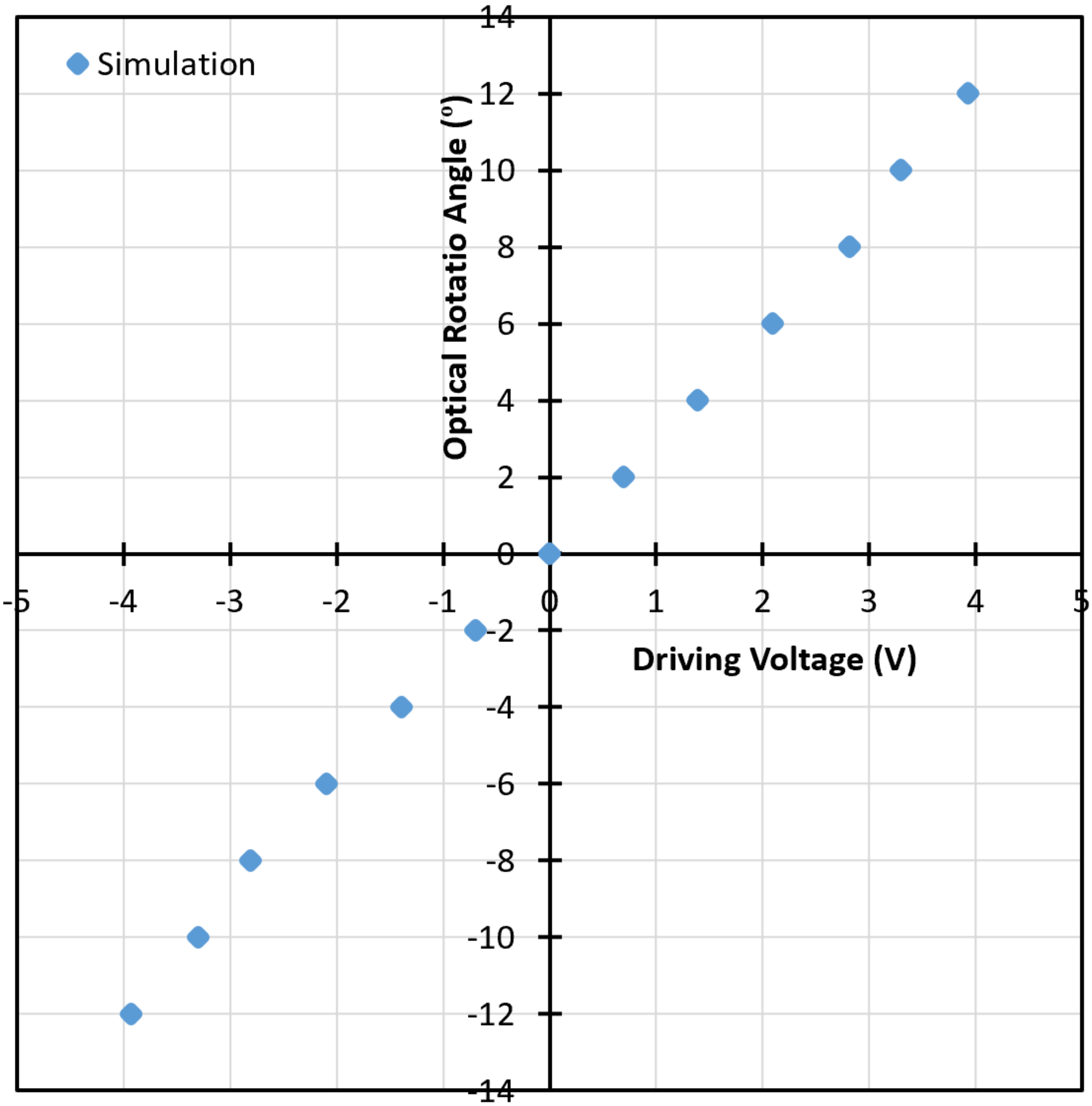

Figure 3-4: Graph of Optical rotation angle versus driving voltage.

Figure 3-4 shows the graph relation of the simulated static response of the EEM-FPCB micromirror for optical rotation angle and driving voltage. As expected, the optical rotation angle of the EEM-FPCB micromirror follows a linear relationship with the driving voltage supplied to the solenoids. The maximum optical angle simulated is 12°, which requires a driving voltage of 3.93 V, close to the maximum voltage rating (4.1 V) of the solenoids. Therefore, static simulations were stopped for an optical angle of 12°.

3.2.2 Dynamic Performance

Modal analysis on ANSYS is used to simulate the dynamic response of the EEM-FPCB micromirror. The first three modes (resonant frequencies) of the EEM-FPCB micromirror have been simulated for both configurations.

The first mode of the first configuration has a resonant frequency of 117 Hz, with rotation about the torsion beams, shown in Figure 3-5. The 2^{nd} and 3^{rd} modes have respective resonant frequencies of 293 Hz and 1149 Hz. The 2^{nd} mode resonates with vertical translation shown in Figure 3-6. The 3^{rd} mode resonates with lateral translation shown in Figure 3-7. The resonant frequency of the first mode is the primary dynamic response that will potentially provide the largest optical angle rotation of the EEM-FPCB micromirror during scanning.

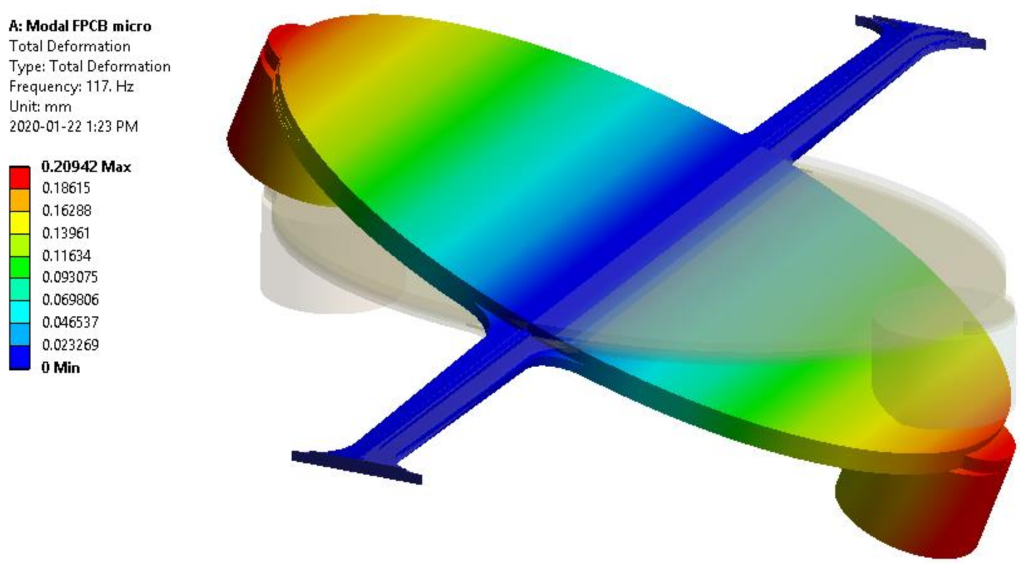

Figure 3-5: 1st Mode.

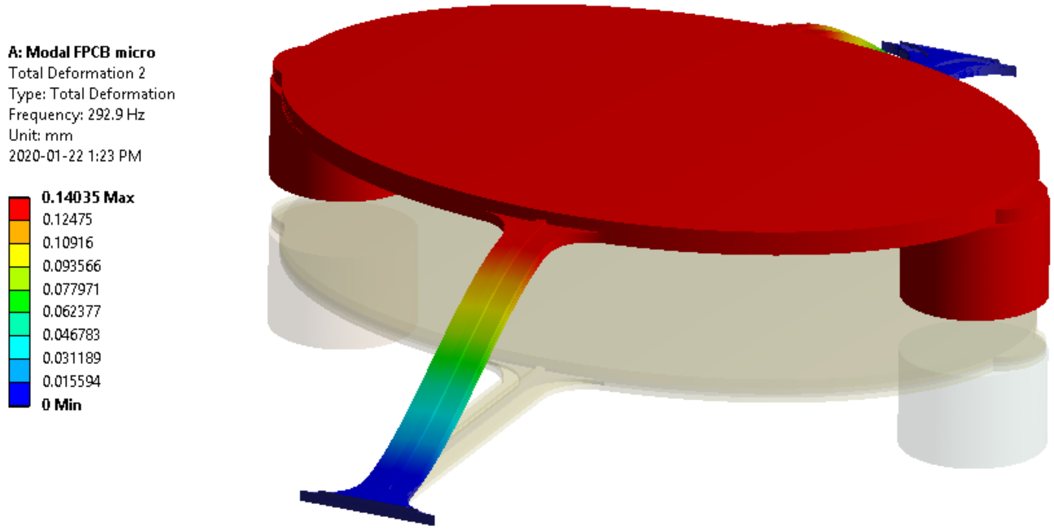

Figure 3-6: 2nd Mode.

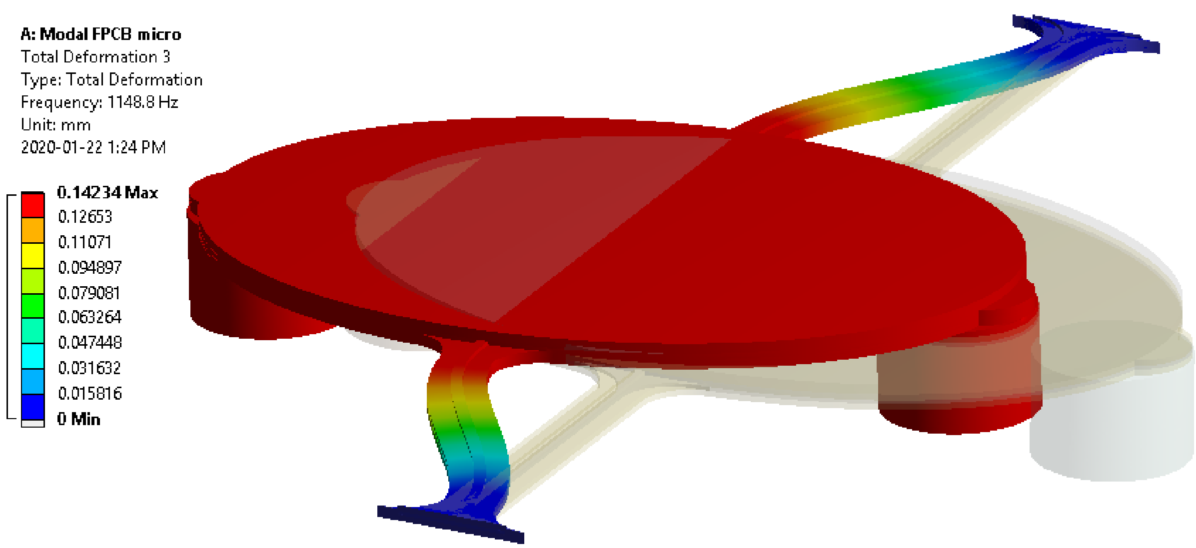

Figure 3-7: 3rd Mode

3.2.3 Stress Analysis

The stress experienced by the FPCB material during the mechanical rotation of the EEM-FPCB micromirror has been simulated using ANSYS workbench for static structural analysis. FPCB is comprised of copper and polyimide, which have different yield strengths. The yield strength of copper is determined using the journal paper titled, "The yield strength of thin copper films on Kapton" [62]. The following equation is a function of material layer thickness and is used to determine the yield strength of copper,

$$\sigma_y = 116 + 355t^{-0.473} \qquad (3)$$

The thickness of the copper layer used within the design of the EEM-FPCB micromirror is 36 µm. Using Equation 3, and the yield strength of copper was calculated to be 181.2 MPa. The yield strength of polyimide is 86-89 MPa, which was determined using the material properties of Kapton Polyimide listed in the site titled "Dielectric Manufacturing" [63]. The following Table 6 lists the maximum stress experienced by polyimide and copper for a mechanical rotation of ±10^{o} (±20^{o} optical angle).

Table 6: Stress analysis of Polyimide and Copper

	Polyimide	**Copper**
Maximum stress (MPa)	10 MPa	119 MPa
Yield stress (MPa)	86-89	181.2
Location	Torsion Beam	Torsion Beam

Furthermore, using the limiting yield stress of copper and polyimide, the simulated maximum angle that the EEM-FPCB micromirror can achieve is ±10^{o} mechanical rotation angle (±20^{o} optical angle), without experiencing plastic deformation. The maximum stress is experienced by the thin copper in the FPCB structure torsion beam during mechanical rotation, as shown in Figure 3-8. Furthermore, from simulated stress analysis a maximum optical rotation angle of ±30° (60° Field-of-View), without exceeding the yield stress limits of polyimide and copper. Failure during the scanning motion about the torsional axis will be attributed to the shear stress experienced by copper (primarily) within the torsion beams. This is due to its relatively larger young's modulus compared to polyimide, making it stiffer material that is more resistant to deformation (torsion or bending). The high concentration of stress from torsional rotation is justified in Figure 3-8.

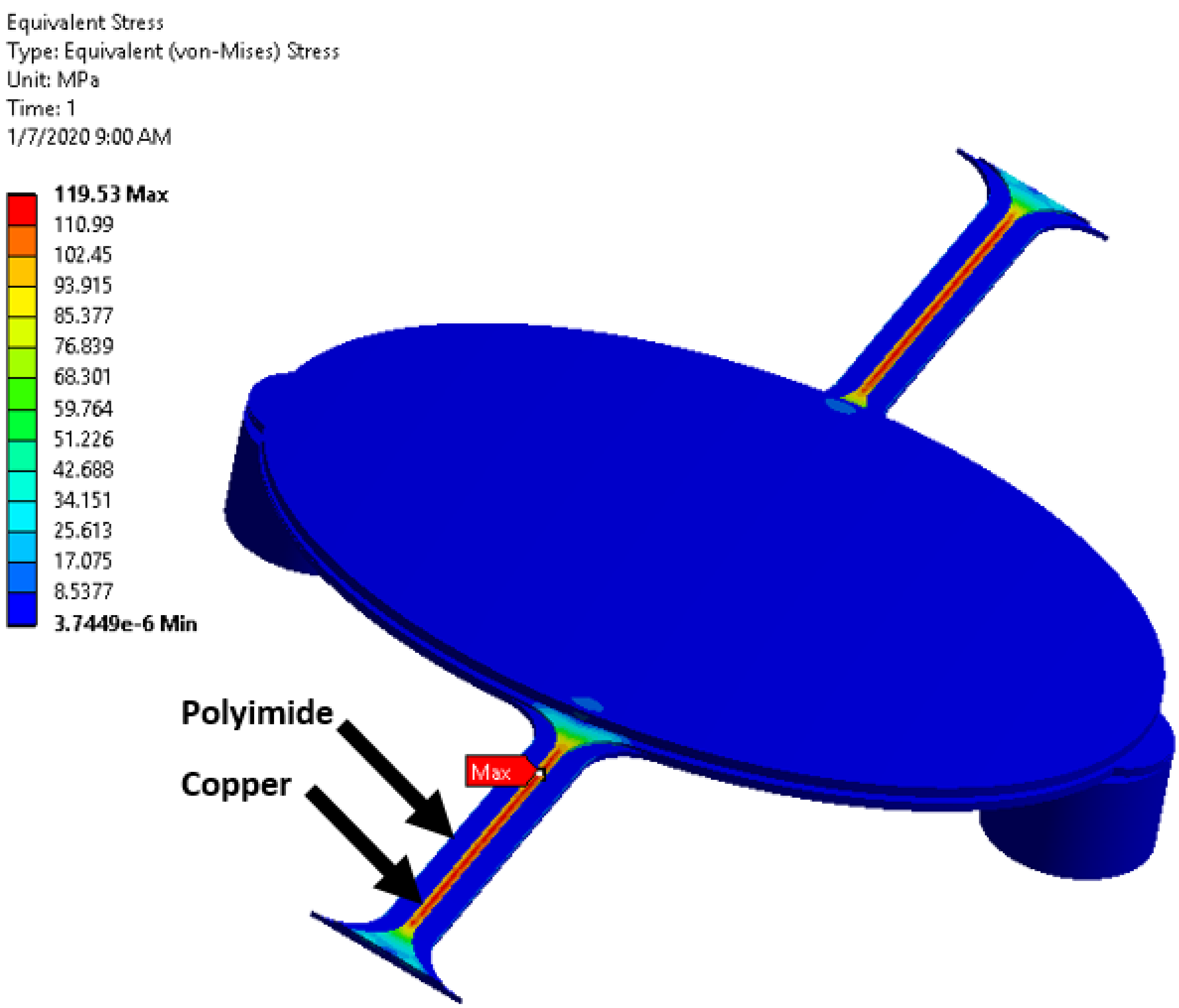

Figure 3-8: Stress analysis of EEM-FPCB micromirror for ±10° mechanical rotation.

3.3 Second Configuration

3.3.1 Static Performance

The second configuration follows the same process (steps 1-3) for simulating static response as the first configuration, explained in the previous section (3.2). The final results of optical angle versus driving voltage (step 3) for the second configuration is shown in Figure 3-5.

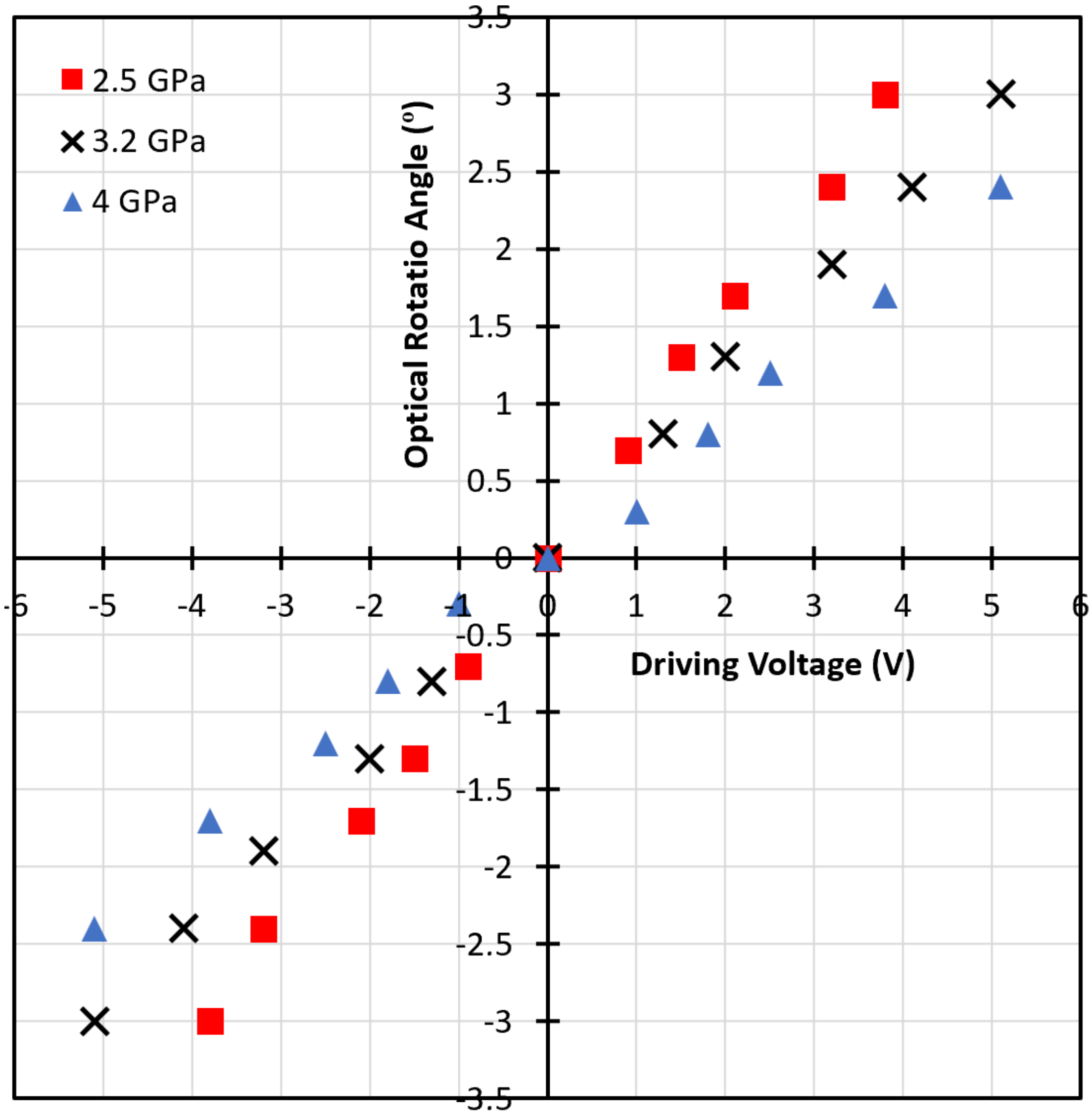

Figure 3-9: Graph of optical rotation angle versus driving voltage [54]

The second configuration only comprises of polyimide within the torsion beams, therefore the parameters used for polyimide during simulations significantly affect the simulation results. Due to the viscoelastic properties of polyimide, the young's modulus of polyimide can vary within the range from 2-4 MPa and is further affected by other factors such as humidity, which will be explained in chapter 4. Therefore, multiple young's moduli of polyimide (2.5, 3.2 & 4 GPa) have been used for static simulation. A non-high static angle (±3^{o} optical angle) was simulated for the second configuration since the application for this configuration is intended for large angle scanning using resonant rotation.

3.3.2 Dynamic Performance

The first three modes of the second configuration have also been simulated and shown in Figure 3-9 (a)-(c) respectively. The first mode has a resonant frequency of 207 Hz, having rotation about the torsion beams. Similar to the first configuration, the 1st mode is of most significance as it will provide the greatest mechanical rotation angle during scanning. The 2nd and 3rd modes have respective resonant frequencies of 437 Hz and 1480 Hz. The 2nd mode translates vertically and the 3rd mode rotates about the width axis of the elliptical micromirror.

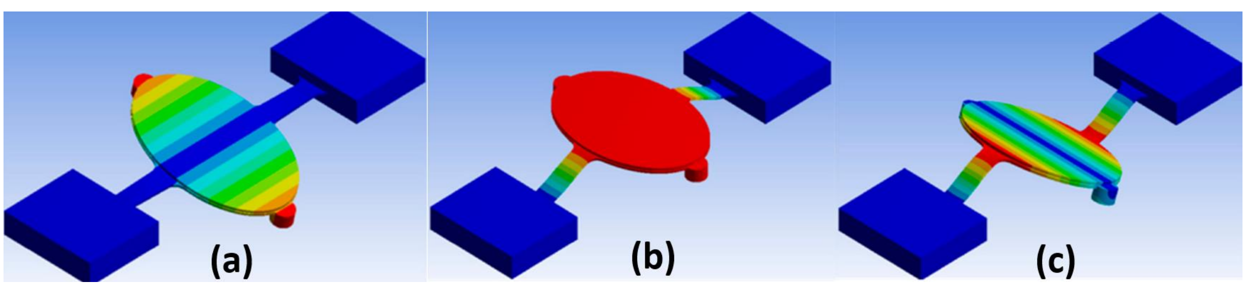

Figure 3-10: (a) 1st mode (b) 2nd mode (c) 3rd mode [54]

3.3.3 Stress Analysis

The maximum rotation angle (about the torsion beams) of the second configuration depends mainly on the yield strength of polyimide, since no copper layer was added into the torsion beams. The yield strength of polyimide used is 86-89 MPa, same as the first configuration. Using this yield strength of polyimide, the maximum optical scan angle of the second configuration of the EEM-FPCB micromirror is limited to ±50^{o} (±25^{o} mechanical rotation angle). The second configuration was designed in having no copper in the torsion beams, to achieve a greater optical scan angle at resonance than the first configuration. This is because copper has a higher young's modulus (stiffer or less flexible) compared to polyimide.

Chapter 4. EEM-FPCB Micromirror Prototype & Testing

Two Prototype scanners have been made, one for the first configuration and another for the second configuration. The static and dynamic performance have been experimentally tested by an optical setup using a laser (for illumination) and a PSD (position sensitive detector) for tracking of the optical rotation angle of the EEM-FPCB micromirror during laser spot scanning. Multiple gold-coated elliptical micromirror plates (of the same design, 8 mm x 5.5 mm) were fabricated and used for both configuration designs of the EEM-FPCB micromirror scanner, shown in Figure 4-1. These mirror plates are bonded using an adhesive to the middle elliptical seat for both configurations. The flatness of the gold-coated elliptical micromirror plate is measured on a Zygo 3D optical profiler. Its ROC (Radius-of-Curvature) is measured to be ~15 m, which varies between 10 ~ 20 m. The variation could be caused by non-uniform metal coating on the micromirror plate during fabrication. These highly flat mirror plates were used for both configurations. The static & dynamic testing of the 1st and 2nd configurations (in that order) will be discussed in the following sections, 4.1 and 4.2 respectively.

Figure 4-1: Gold-coated elliptical (8 mm x 5.5 mm) micromirror plates.

4.1 First Configuration Prototype

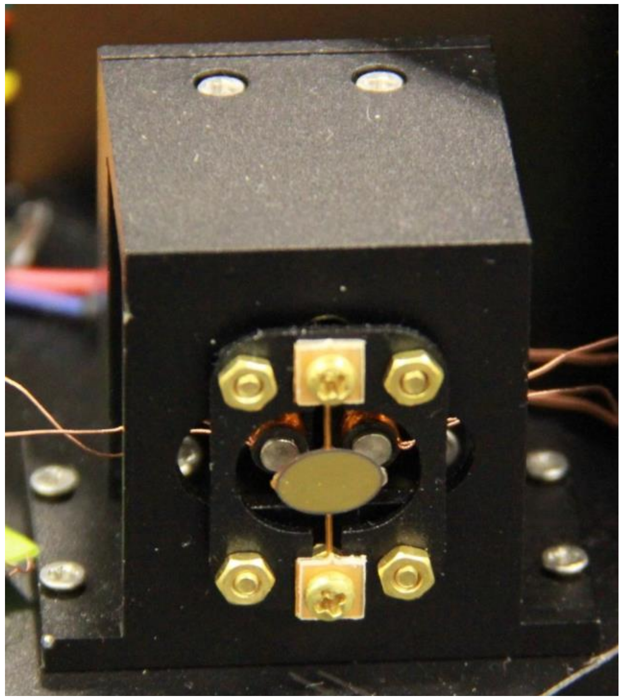

Figure 4-2: Assembled 1st configuration EEM-FPCB micromirror scanner.

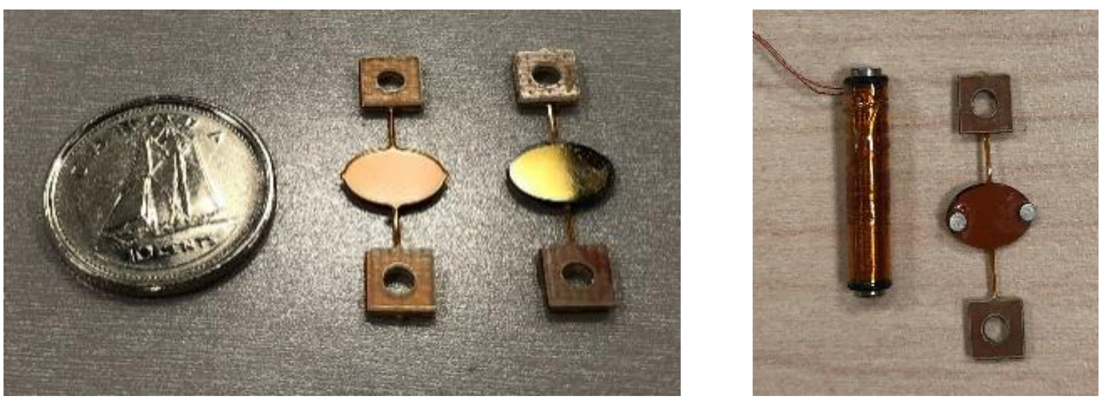

Figure 4-3: 1st configuration FPCB micromirror structure (Left) FPCB micromirror front side with & without bonded mirror plate. (Right) Solenoid and backside of FPCB micromirror.

The dimensions of the assembled 1st configuration of the EEM-FPCB micromirror scanner is 3 cm x 3 cm x 3.5 cm, shown in Figure 4-2. Figure 4-3 (Left) shows the 1st configuration FPCB micromirror structure with and without the bonded micromirror plate. A small coin (Ø18 mm) has been included in the figure for scale. Figure 4-3 (Right) shows the solenoid (external electromagnet) used and the backside of the FPCB structure with two bonded PM discs at the tips of the width of the elliptical middle seat. The FPCB micromirror is assembled with a gap of approximately 2.5 – 3 mm between the centers of the solenoids and bonded PM discs on the backside of the FPCB micromirror structure. This gap was difficult to accurately measure after assembly. In addition the solenoids were assembled approximately 8mm apart. The setup of testing the FPCB micromirror's static and dynamic performance response is shown in Figure 4-4, which consists of a laser and PSD.

Figure 4-4: Setup for testing optical rotation angle of the EEM-FCPB micromirror.

4.1.1 Static Response

The experimental and simulated static response of the first configuration design EEM-FPCB micromirror scanner is shown in Figure 4-5. The variance between the experimental and simulated static performance results could be attributed to the offset between the PM discs and solenoids. Furthermore, for higher angle scans the centers of the PM discs are not aligned with the centers of the solenoids. During simulations, the PM discs and solenoids were assumed to have their centers perfectly aligned. The experimental testing of the static performance of 1st

configuration EEM-FPCB micromirror was stopped for an angle of 12°, since the voltage required to achieve such angle surpasses the voltage rating of the solenoid of 4.1 V.

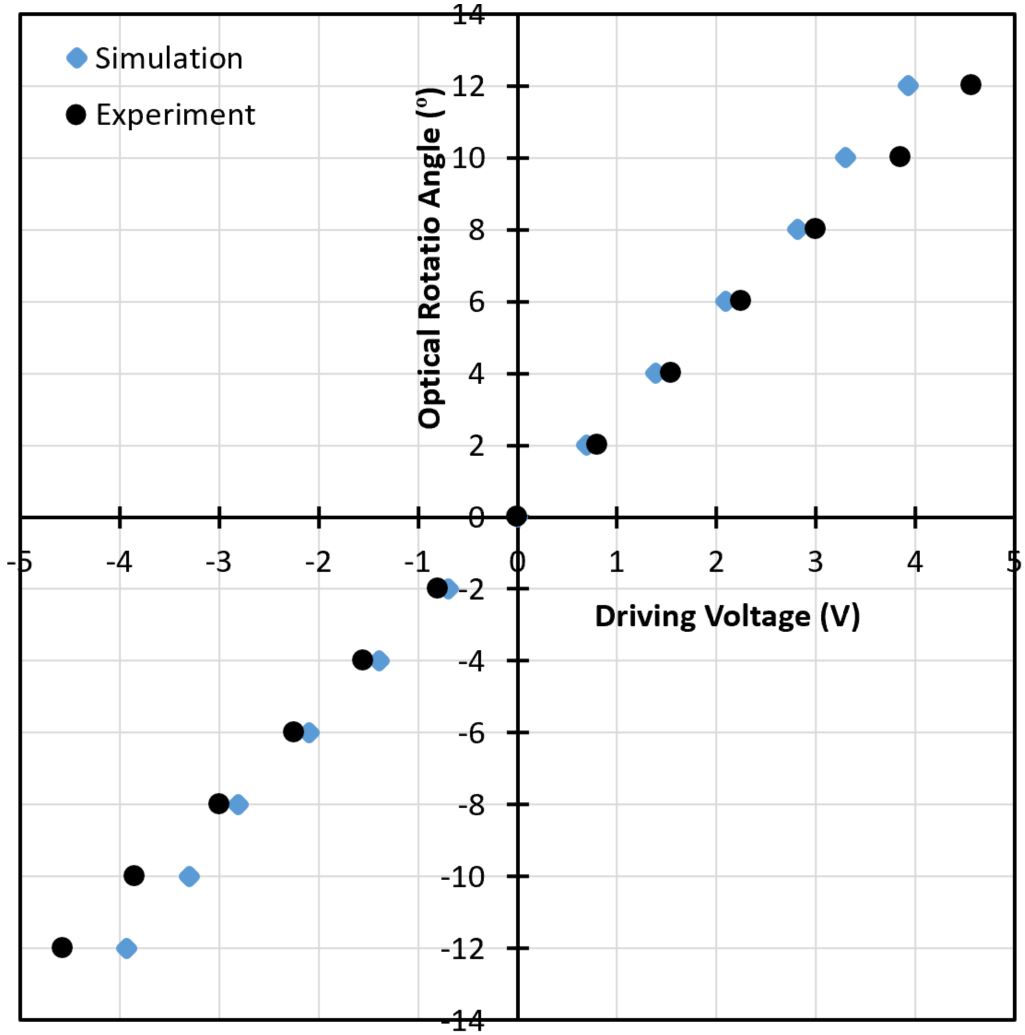

Figure 4-5: 1st configuration EEM-FPCB micromirror's static performance.

4.1.2 Dynamic Response

Figure 4-6 shows the experimental results of total optical scan angle (will be referred to as FOV, for Field-of-View) versus driving frequency at various driving voltages. The rotation resonant frequency (1st mode) of the 1st configuration EEM-FPCB micromirror was tested to be 111 Hz, which is marginally lower than the simulated value of 117 Hz. The variance between experimental and simulated values of the rotational resonant frequency could be attributed to the perfect clamping conditions assumed during simulations. In addition, humidity has been observed to affect the scanning performance of both configurations of the EEM-FPCB micromirror. Further details on the effects of humidity will be discussed in the following section, 4.1.3.

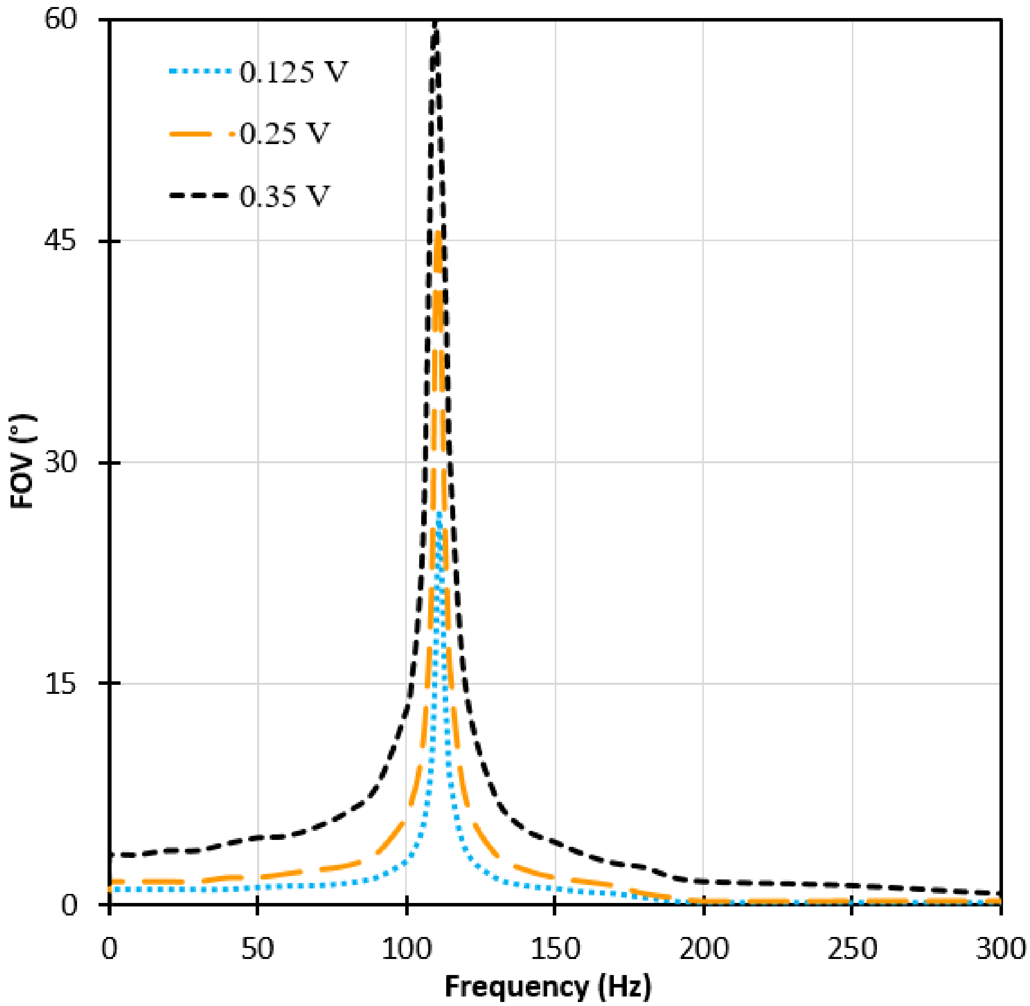

Figure 4-6: Dynamic performance of 1st configuration EEM-FPCB Micromirror

A sinusoidal driving voltage with amplitudes of 0.125 V, 0.25 V, and 0.35 V have been used to test the dynamic performance of the 1st configuration EEM-FPCB micromirror for a frequency range from 0 Hz to 1000 Hz. However, frequencies greater than 300 Hz weren't included in Figure 4-6, since the optical scan angle for all driving voltage amplitudes, settled to 0°. In addition, a second resonant frequency peak should've been detected at approximately 293 Hz (according to simulations in chapter 3), however the setup shown in Figure 4-4 can only detect the first mode of scanning rotation about the torsion beams. Each sinusoidal driving voltage amplitude yielded a resonant frequency of 111 Hz. In addition, the FOV at resonance for the driving voltages of 0.125 V, 0.25 V, and 0.35 V are 27°, 46°, and 60° respectively. Recalling back to the stress analysis in section 3.2.3, the simulated maximum optical angle achievable by the 1st configuration EEM-FPCB micromirror (without exceeding the yield stress limits of polyimide and copper) is 60°FOV. Therefore, the testing driving voltage was stopped at 0.35 V which achieves a maximum FOV of 60° at resonance. Testing of a driving voltage greater than 0.35 V could potentially damage the FPCB structure due to plastic deformation.

4.1.3 Fatigue Testing

The reliability and durability of the 1st configuration EEM-FPCB micromirror scanner has been tested at 100 Hz at a FOV of 40°. The fatigue testing has been performed by having the scanner run in 24/7 mode, which currently has lasted a couple months. Thus far the prototype has endured approximately 1.2 billion cycles with the fluctuation in FOV mainly caused by the changes in humidity of the testing environment. Figure 4-7 shows the Field-of-View of the 1st configuration EEM-FPCB micromirror scanner versus the numbered of cycles endured. Additionally, Figure 4-8 shows the correlation between changes in scanning FOV and humidity. The dashed lines in the figures are the regions where no data was recorded due to a technical accident of the computer not recording data. However, during this technical accident, the fatigue test was continuously running without interruption.

Polyimide is a viscoelastic material that behaves as both a fluid and elastic solid at the same time, this is due to its long molecule strands of polymer. Furthermore, humidity affects the material properties of FPCB such as its stiffness and/or flexibility [64-66]. As observed from Figure 4-8, the fluctuations in humidity caused a proportional fluctuation in the scanning FOV of the EEM-FPCB micromirror scanner, i.e., as humidity increased, scanning FOV decreased and vice versa. Furthermore, the greater the change in humidity, the greater the change in scanning FOV.

The problem of humidity affecting the scanning performance of the EEM-FPCB micromirror scanner can be solved by vacuum sealing the FPCB micromirror using a transparent glass or plastic contraption.

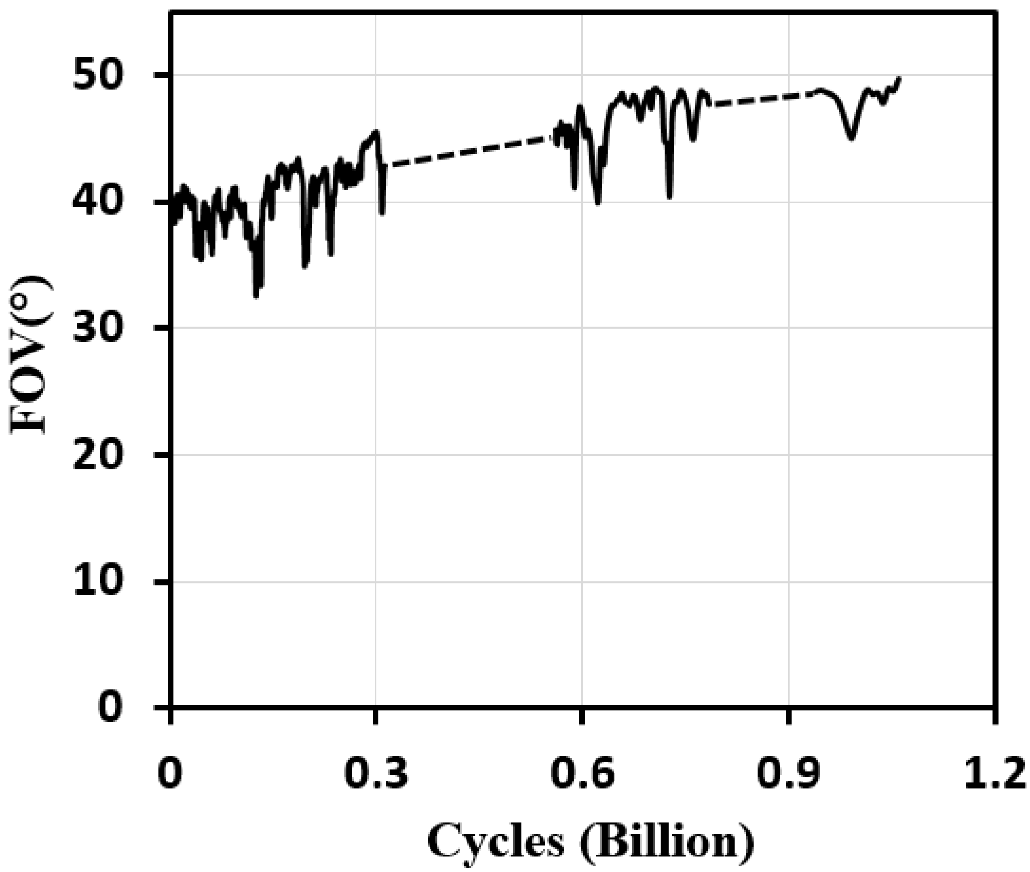

Figure 4-7: Total optical angle (FOV) versus number of oscillation cycles for the 1st configuration.

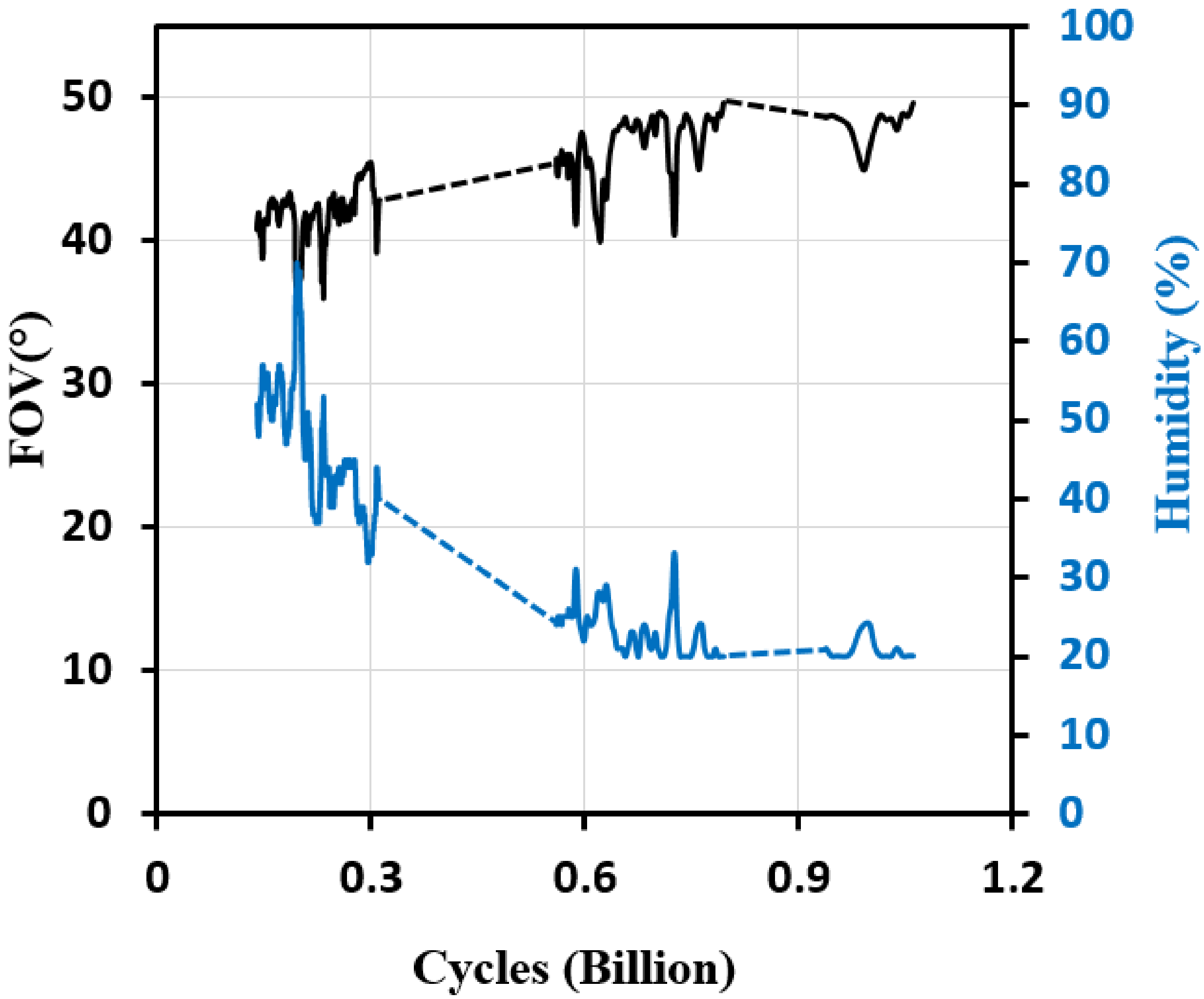

Figure 4-8: Correlation between scanning angle and humidity for the 1st configuration

4.2 Second Configuration

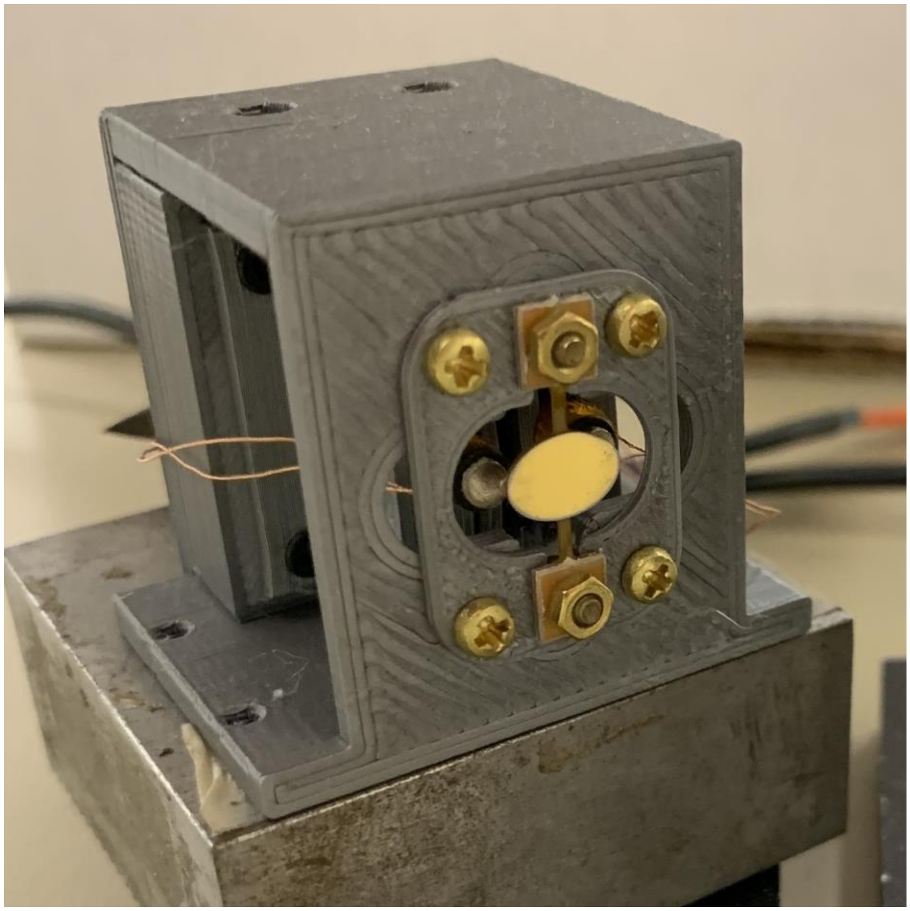

Figure 4-9 Assembled 2nd configuration EEM-FPCB micromirror scanner.

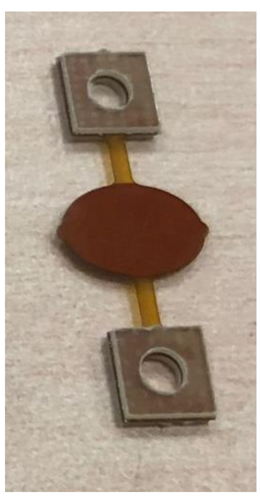

Figure 4-10: 2nd configuration FPCB micromirror structure (Left) Front side of FPCB micromirror without bonded mirror plate. (Right) Solenoid

Figure 4-9 shows the assembled 2nd configuration of the EEM-FPCB micromirror scanner. The dimensions of the assembled scanner is the same as the 1st configuration, since it uses the same mechanical housing part designs, however 3D printed (thus the grey color). Figure 4-10 (Left) shows the front side of the 2nd configuration FPCB micromirror structure without the bonded micromirror plate. Furthermore, compared to the first configuration (see Figure 4-3 (Left)), the 2nd configuration has relatively shorter and wider torsion beams that consists of no copper layer. In addition, Figure 4-10 (Right) shows the relatively larger solenoid used for the 2nd configuration. Two relatively smaller PM discs are also bonded to the backside of the FPCB structure, similar to the 1st configuration shown in Figure 4-3 (Right). The gap between solenoids to PM discs and solenoids to solenoids, are assembled similar to the 1st configuration (refer to section 4.1). The differences between the 1st and 2nd configurations have already been explained and can be referenced in chapter 3 of Modelling.

The experimental testing of the 2nd configuration EEM-FPCB micromirror scanner uses the same setup of a PSD and laser as shown in Figure 4-4.

4.2.1 Static Response

The experimental testing and simulated results of the static performance of the 2nd configuration EEM-FPCB micromirror is shown in Figure 4-11. As mentioned prior, multiple young's moduli of polyimide have been simulated. From Figure 4-11, the simulated results for a polyimide young's modulus of 3.2 GPa best fits the experimental results. This shows that the discrepancy in the material properties of FPCB polyimide, especially young's modulus, can cause a variance between simulated and experimental results. Only the general material properties of FPCB polyimide before the FPCB fabrication process is available. Furthermore, after the FPCB fabrication process, the material properties of FPCB polyimide can potentially change and vary, which wasn't available by the manufacturer.

As mentioned in chapter 3, non-high optical scan angles (±3°) has been tested for the 2nd configuration because it is intended for the application of large angle laser scanning at its resonant frequency, as opposed to quasi-static scanning.

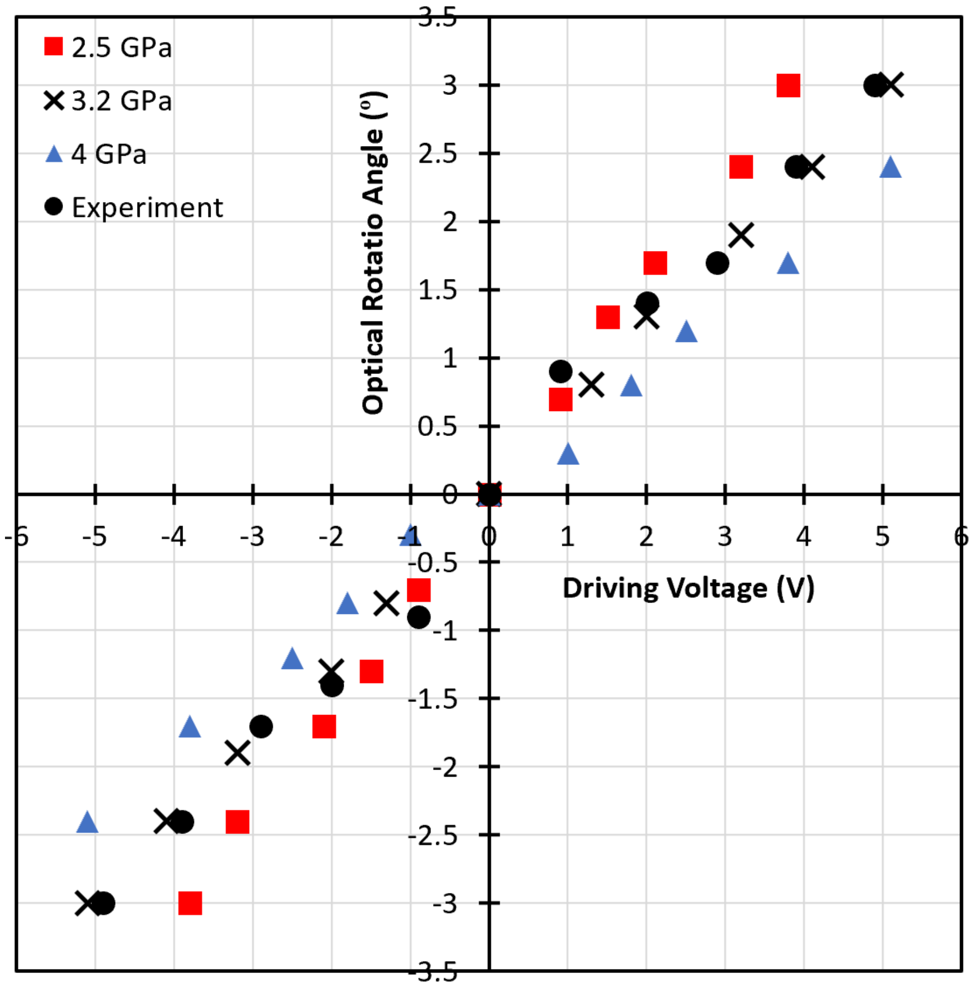

Figure 4-11: 2nd configuration EEM-FPCB micromirror's static performance.

4.2.2 Dynamic Response

The dynamic performance of the 2nd configuration of the EEM-FPCB micromirror scanner has been experimentally tested using a sinusoidal driving voltage of ±3 V over the frequency range of 0 Hz to 1000 Hz. Figure 4-12 shows the experimental dynamic performance results of the 2nd configuration EEM-FPCB micromirror scanner. The experimental resonant frequency was tested to be 191 Hz, providing a FOV of 62°. Similar to the 1st configuration, the experimental resonant value is lower than the simulated value of 226 Hz. This variance again can be attributed to the imperfect clamping boundary conditions during assembly, which is assumed as perfectly fixed (without tension or slack on the FPCB micromirror structure) during simulations. Furthermore, experimental tests revealed that when slack or tension was evident in the FPCB micromirror structures torsion beams, the resonant frequency varied by 20-30 Hz higher and vice-versa.

A FOV of 100° was simulated as the maximum limit (refer to chapter 3) that can be achieved without exceeding the yield stress of the polyimide torsion beams. However a safety margin was considered by having the prototype not exceed 70° FOV. Therefore a higher driving voltage than ±3 V (providing 62° FOV) wasn't pursued for greater optical scan angles.

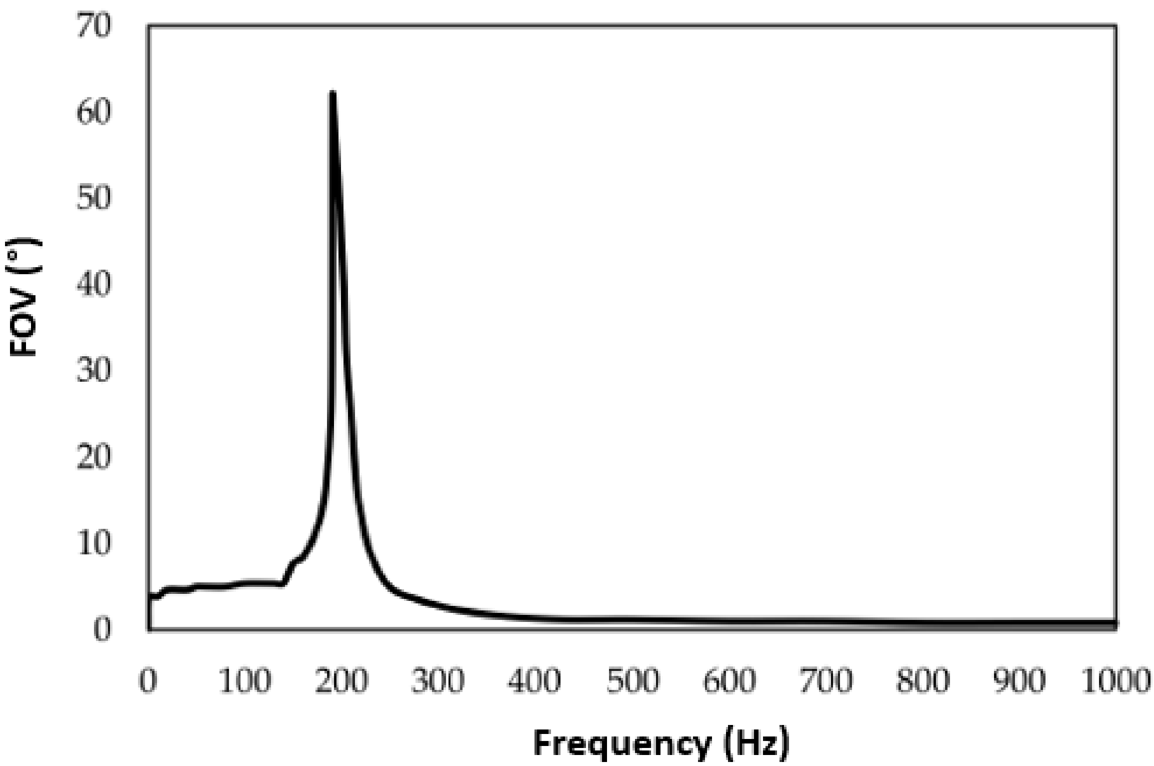

Figure 4-12: Dynamic performance of 2nd configuration EEM-FPCB Micromirror

4.2.3 Fatigue Testing

The reliability and durability of the 2nd configuration EEM-FPCB micromirror scanner has been tested at 200 Hz at a FOV of 70°. The fatigue testing has been performed by having the scanner run in 24/7 mode, which currently has lasted a couple months. Thus far the prototype has endured approximately 800 million cycles (almost 1 billion) with the fluctuation in FOV mainly caused by the changes in humidity of the testing environment. Figure 4-13 shows the Field-of-

View of the 2nd configuration EEM-FPCB micromirror scanner versus the numbered of cycles endured. Additionally, Figure 4-14 shows the correlation between changes in scanning FOV and humidity. Similar to the 1st configuration fatigue testing results, humidity affects the material properties of FPCB such as its stiffness and/or flexibility.

Again, the problem of humidity affecting the scanning performance of the EEM-FPCB micromirror scanner can be solved by vacuum sealing the FPCB micromirror using a transparent glass or plastic contraption.

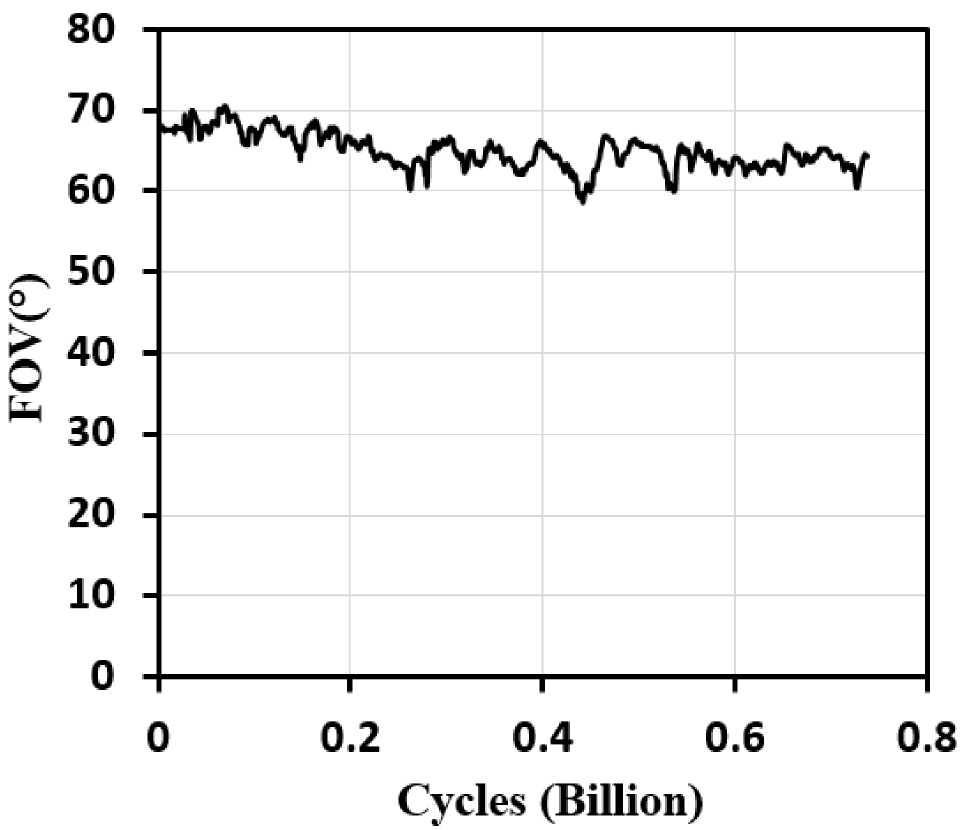

Figure 4-13 Total optical angle (FOV) versus number of oscillation cycles for the 2nd configuration.

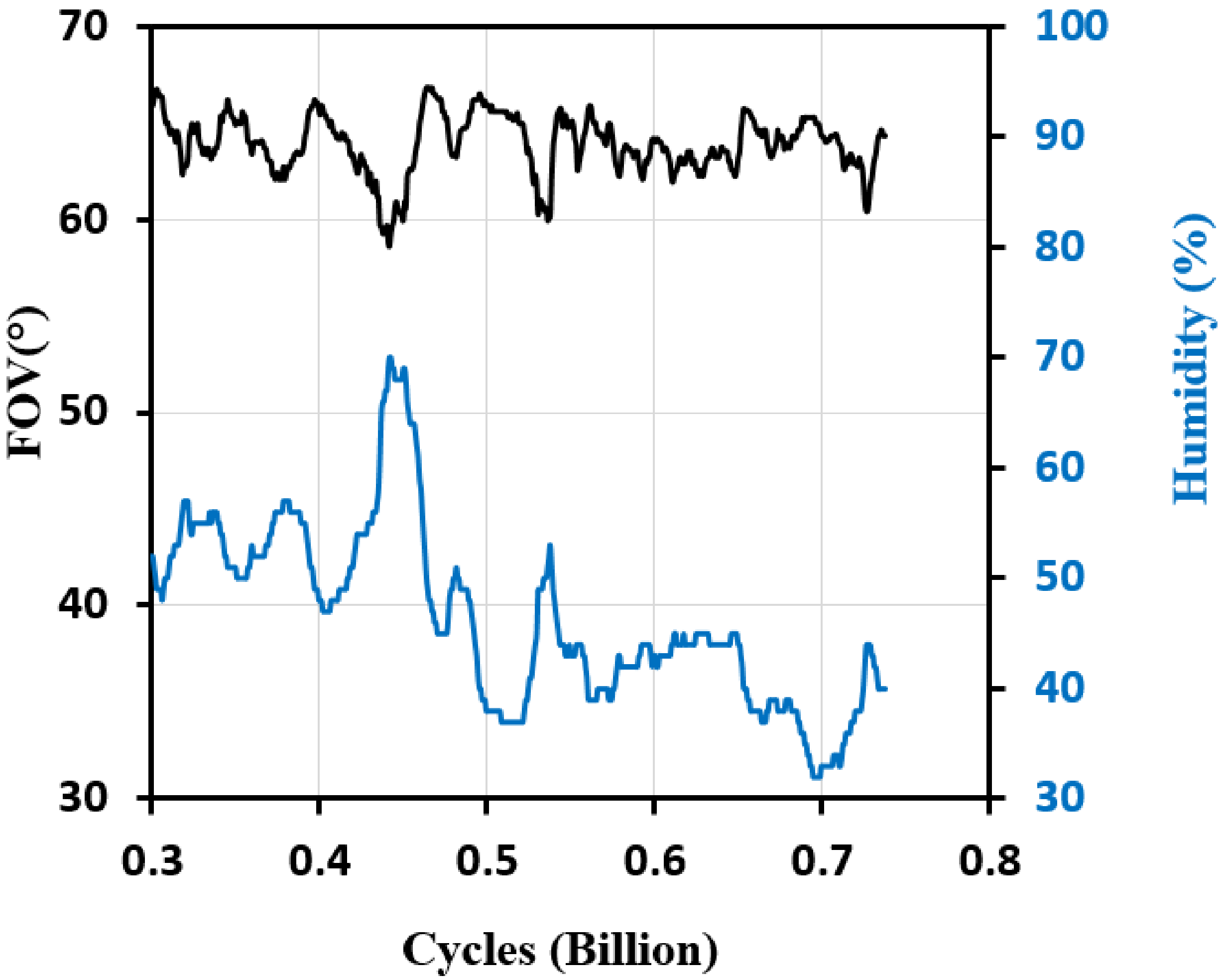

Figure 4-14: Correlation between scanning angle and humidity for the 2nd configuration.

Chapter 5. Scanning Laser Rangefinder

The EEM-FPCB micromirror scanner has been used to realize scanning for the application of laser rangefinding. The developed scanning laser rangefinding prototype is intended for the integration within low-speed automated guided vehicles (AGV), profilometry, 3D scanning, facial and gesture recognition. These application favor a scanner that will provide ample scanning resolution and FOV at moderately high speeds. From the two configurations, the 1st configuration is chosen for this application due to its better suited scanning characteristics. The 1st configuration design of the EEM-FPCB micromirror scanner achieves a greater angle at lower driving voltages and achieves large angle scanning at a relatively lower resonant driving frequency. These scanning characteristics are tabulated and highlighted in Table 7.

Table 7: Scanning performance comparison between 1st & 2nd configuration designs.

	1st Configuration	2nd Configuration
FOV for ±3 V (static)	**16°**	3.4°
Resonant Frequency (1st Mode)	**≈ 100 Hz**	≈ 200 Hz

For a lower voltage, the 1st configuration provides adequate scanning FOV at moderately fast speeds for scanning laser rangefinding. Furthermore, the relatively lower resonant scanning frequency (≈ 100 Hz) provides a sufficient refresh rate and better resolution for scanning laser rangefinding. In contrast, the 2nd configuration is intended for scanning at higher speeds, due to its relatively higher resonant frequency. This results in the sacrifice of lower scanning resolution for scanning laser rangefinding, i.e., for any given range measurement sampling rate, the faster the scanning frequency, the sparser the amount of range measurements per scan becomes.

Although the 1st configuration was chosen due its previously mentioned ideal scanning characteristics, the 2nd configuration has advantages of its own. The 2nd configuration is capable of achieving a larger scanning FOV at high speeds (≈ 200 Hz). This is due to the absence of a copper within the torsion beams, allowing for a greater maximum optical rotation angle whilst not exceeding the yield stress of the polyimide beam. In addition, the 2nd configuration has a maximum optical scanning FOV limit of 100° (±50), compared to the 1st configuration which is limited to 60° (±30°). In general, the 2nd configuration has the advantage of large angle scanning, however only at high speeds (high driving frequency) and higher driving voltage. Such characteristics are advantageous for applications that require a high speed refresh rate and wide angle scanning. Such applications include unmanned aerial vehicles (UAV), high-speed AGV's, and LiDAR.

This chapter will explain the working principle (method) used in to determine range by the use of laser spot illumination. Furthermore, the design and assembly of the mechanical parts, components, and data acquisition (DAQ) program utilized to construct the EEM-FPCB micromirror scanning laser rangefinder prototype will be described. Lastly, the testing and experimental results will be presented.

5.1 Design & Working Principle

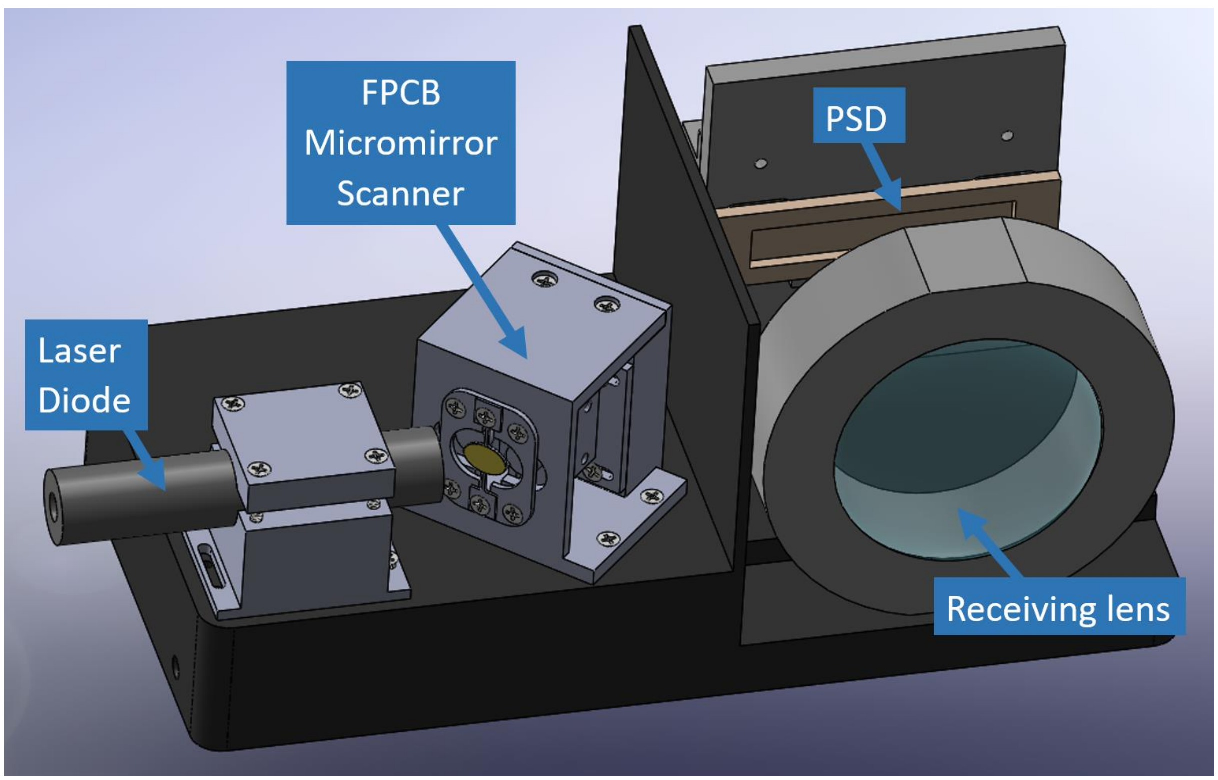

Figure 5-1: FPCB micromirror based laser scanning rangefinder.

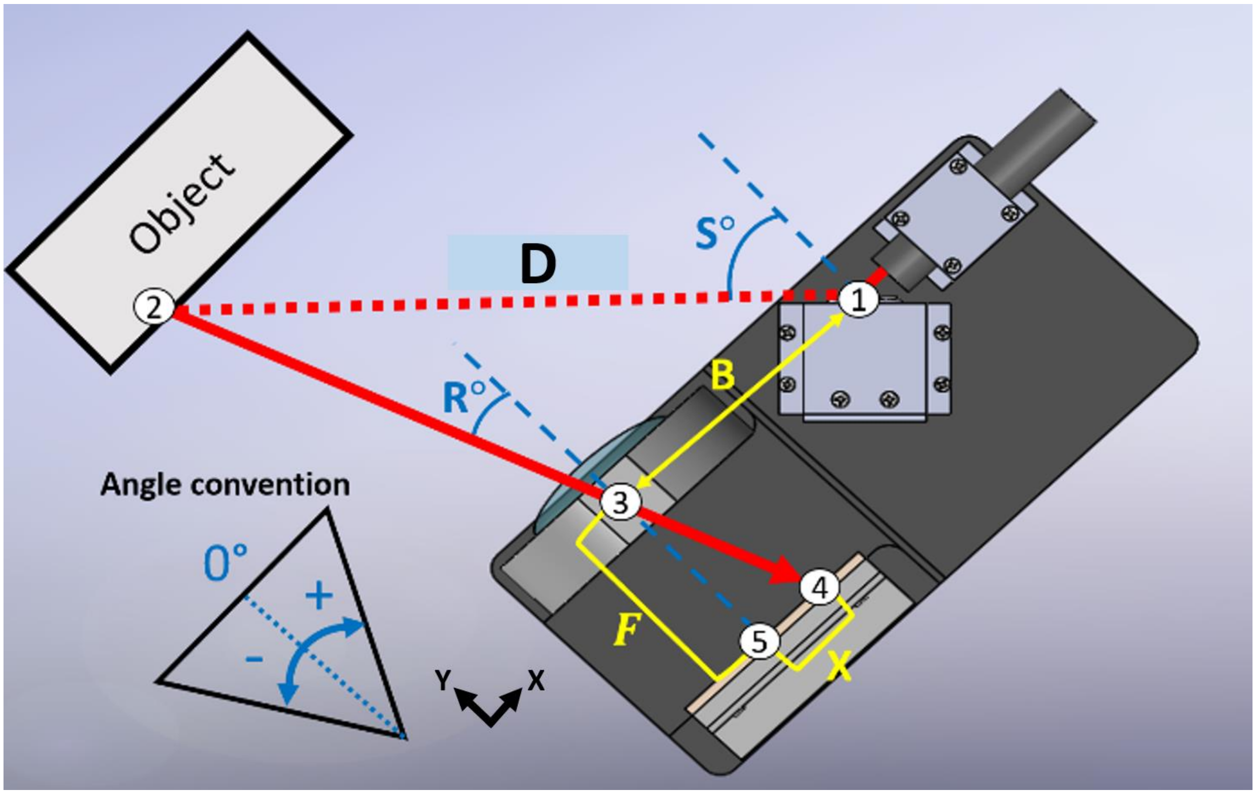

Figure 5-2: Laser triangulation working principle.

The two main methods of laser rangefinding are Triangulation and Time-of-flight. In comparison to TOF, triangulation method was chosen for its advantage of great accuracy for short (mm range) to medium ranges (≤ 15 m), simple hardware, simple processing, and low-cost [12, 67-69]

Figure 5-1 shows the major components of the FPCB scanning laser rangefinder. These components include the EEM-FPCB micromirror scanner (1st configuration), laser diode, receiving lens, and PSD. A PSD has been chosen for its simple signal processing and fast response [70, 71], when compared to other traditional image sensors such as CCD (Charged Coupled Device), CMOS (Complementary Metal-Oxide-Semiconductor), & PD (Photo Diode).

Figure 5-2 shows the working principle of using the triangulation method to measure range and/or distance. The variables shown in the figure are as follows: laser spot distance on PSD (X), focal length (F), receiving angle (R°), optical scanner angle (S°), base length (B), and diagonal distance between the object and micromirror center (D).

The laser diode spot projection is illuminated towards the reflective surface of the micromirror plate of the EEM-FPCB micromirror scanner. The EEM-FPCB micromirror then reflects and scans the incident laser spot laterally along a line in the x-direction (refer to Figure 5-2), illuminating objects and/or obstacles within the scanned environment. The scanned laser spot incident onto the surface of an object, is diffusely reflected and collected by the receiving lens. The receiving lens then focuses the diffusely reflected light onto the PSD (image sensor), which produces a voltage output proportional to the received laser spot position on the PSD.

The path of the laser spot from point 1 to 3 (refer to Figure 5-2) creates a triangle, whose parameters (sides and angles) can be solved using trigonometric relations and equations. In order to solve all parameters of the triangle, at least any three of the triangles parameters must be known. The first known parameters is the base length (B), which is the measured fixed center-to-center distance between the micromirror plate of the EEM-FPCB micromirror scanner (Point 1 in Figure 5-2) and receiving lens (Point 2 in Figure 5-2).

Secondly, the scanning angle is known, which is determined using the sinusoidal driving signal supplied to the solenoids. This method saves both space and cost of a sensor to be used for tracking the rotation of the FPCB micromirror during scanning. The scanning laser rangefinding prototype has the EEM-FPCB micromirror operating at 30° optical FOV at 100 Hz, using a sinusoidal driving voltage. The optical rotation scan angle of the EEM-FPCB micromirror is qualitatively assumed to follow a sinusoidal response, shown in Figure 5-3. Therefore EEM-FPCB micromirror's optical rotation scan angle (S°) was modelled using the following equation:

$$S^{\circ} = \theta_o \sin(2\pi f t + \varphi) + \beta \qquad (4)$$

The following variables in Equation 4 are as follows: driving frequency (f), optical scan angle amplitude (θ_o), phase shift between the driving signal and response rotation (φ), initial optical angle of the laser spot before scanning (β), and time (t). An external PSD was used to determine and calibrate those variables (see Figure 4-4) for an optical scanning FOV of 30° at 100 Hz (near resonance) of the EEM-FPCB micromirror scanner. Those values are: θ_o = 15°, φ = 0.44 rad (shown in green in Figure 5-3), f = 100 Hz, and β = 0°.

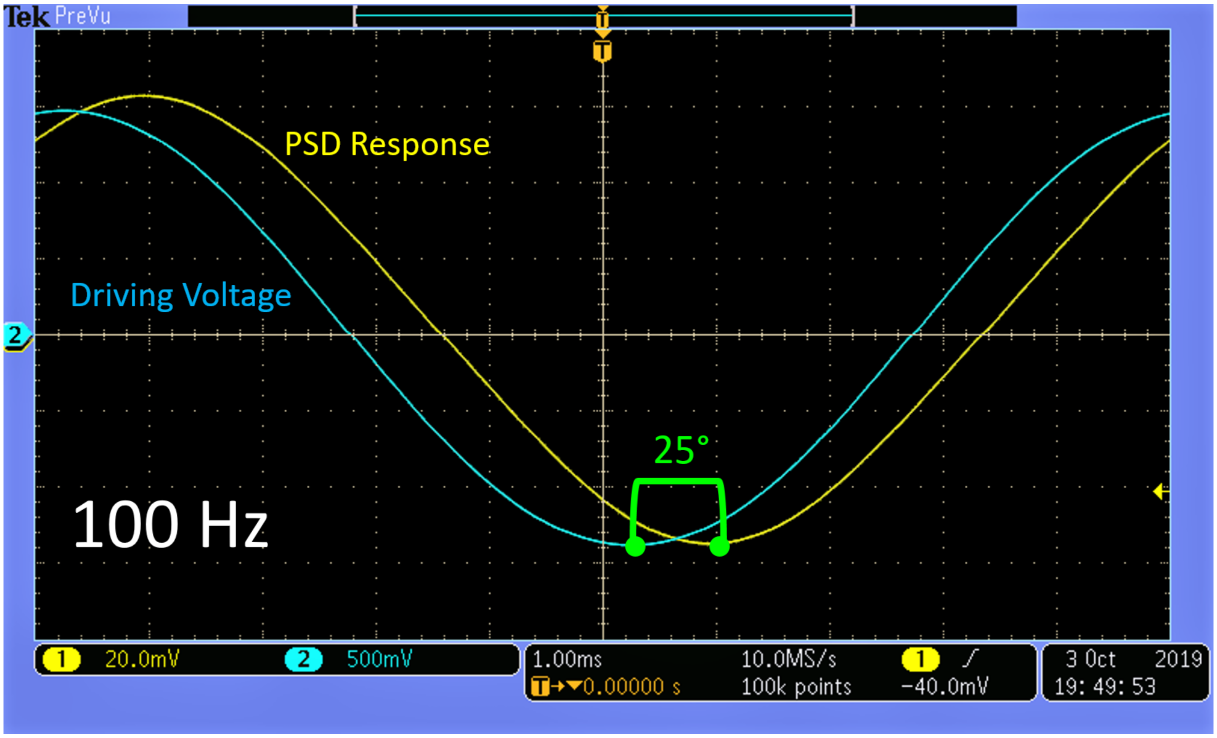

Figure 5-3: Sinusoidal driving voltage (blue) and EEM-FPCB micromirror scanner optical rotation response (yellow)

Lastly, the third known parameter is the receiving angle (R°), which indirectly determined using the focused laser spot position on the PSD (X). The value of X is determined using the voltage output of the PSD. Using the value of X and the know focal length of the receiving lens (F), the receiving angle (R°) is calculated using the following equation,

$$R° = tan^{-1}\left(\frac{X}{F}\right) \tag{5}$$

Since, distance (D) is simply one of the side of the triangle formed by the laser path from points 1 to 3, it can be solved using trigonometric equations (specifically sine law) and the three previously mention determined parameters B, S°, and R°. Finally, once all three parameters of are determined, distance (D) is calculated using the following equation,

$$D = B\left(\frac{\cos{(R°)}}{\sin{(R° - S°)}}\right) \tag{6}$$

5.2 Testing of the Scanning Laser Rangefinding Prototype

5.2.1 Prototype Assembly

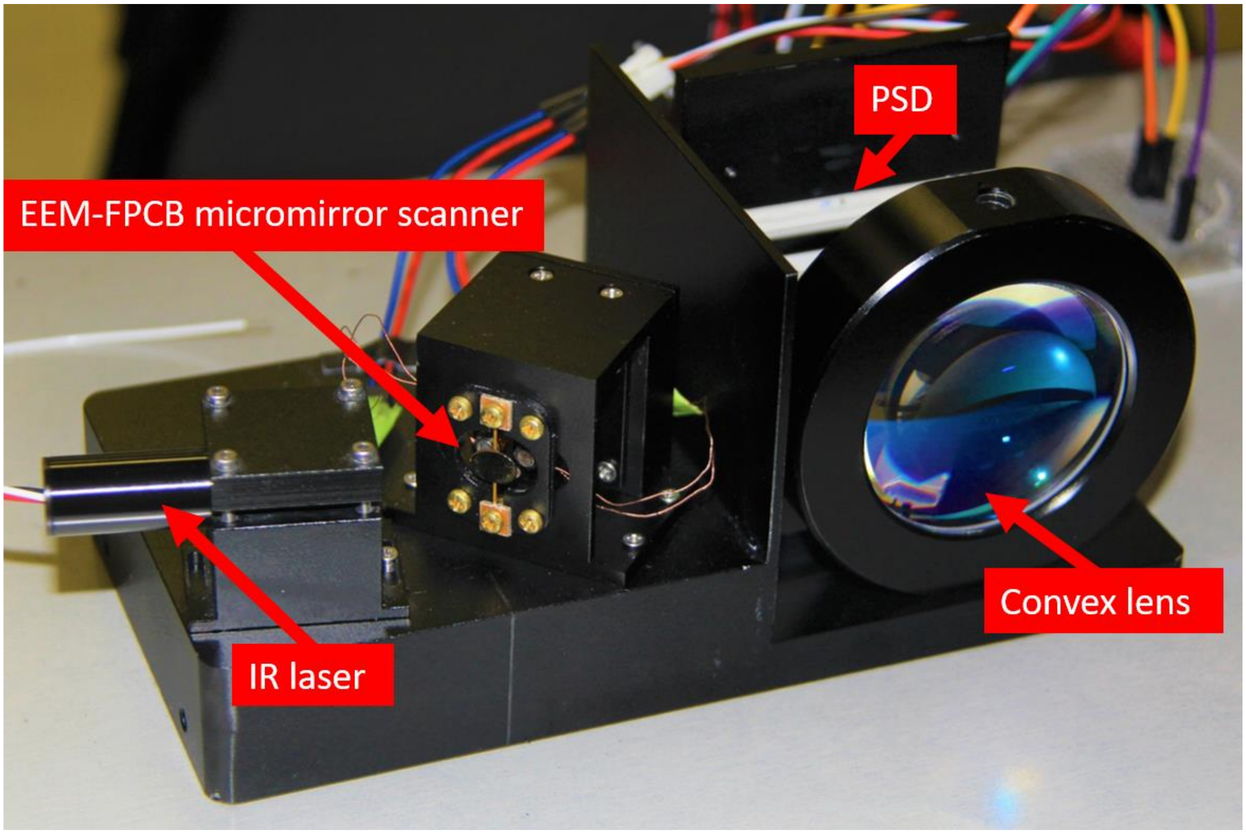

Figure 5-4: Electromagnetic FPCB micromirror based laser rangefinder

Figure 5-4 shows the assembled scanning laser rangefinder prototype with the EEM-FPCB micromirror scanner. The following components used are: infrared (IR) laser, 45 mm 1D PSD, 50 mm convex lens (F = 50 mm), IR long pass filter and EEM-FPCB micromirror scanner. The overall dimensions are 16 cm x 8 cm x 7 cm and the base length (B) is 8.3 cm. A convex lens is chosen for a simple optical setup for imaging the diffusely reflected scanned laser spot onto the PSD for processing.

Figure 5-5 shows the hardware used for the scanning laser rangefinding, which are as follows: 1) PSD amplifier, 2) Function generator, 3) Voltage supplier, 4) Field-programmable gate array, and 5) Scanning laser rangefinding prototype.

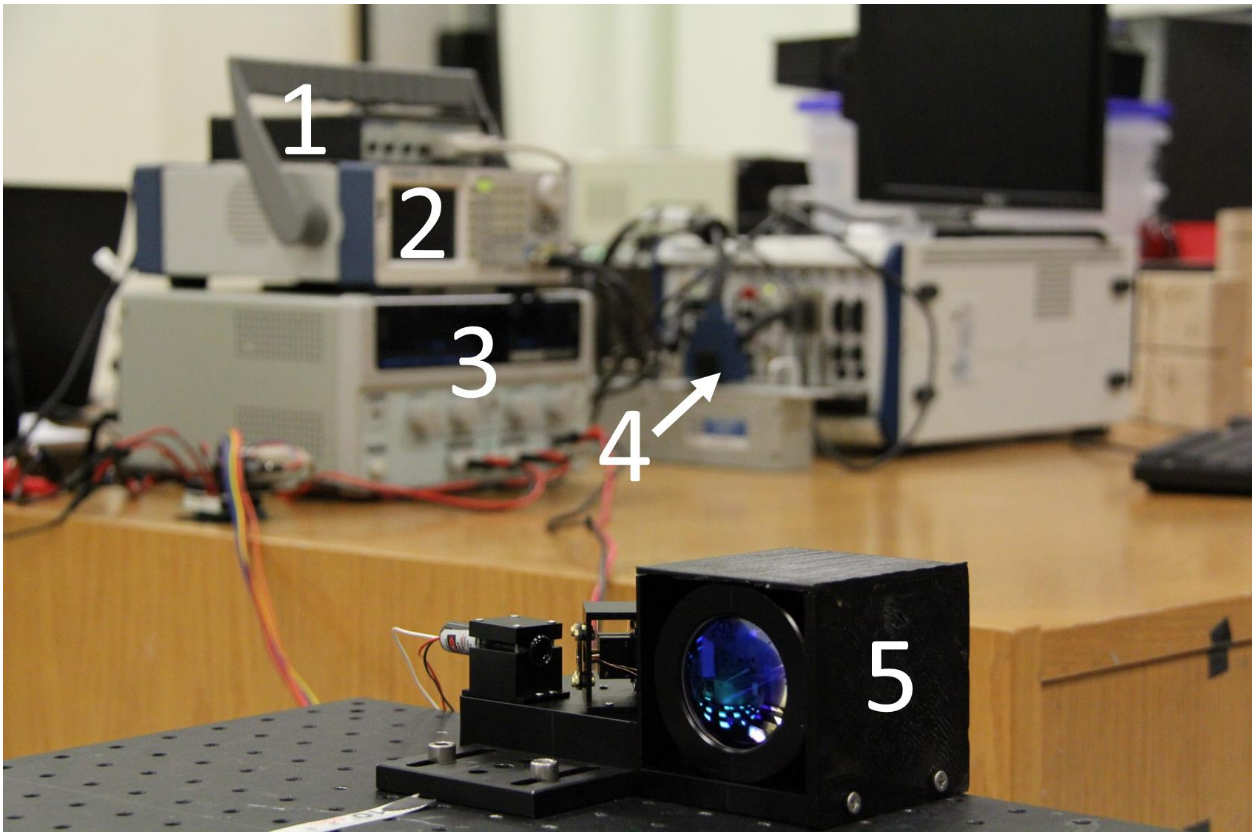

Figure 5-5: Hardware used with the scanning laser rangefinding prototype.

Vibrational influence can potentially affect the scanning response of the EEM-FPCB micromirror especially for frequencies close its resonant scanning frequency or for relatively large vibrational magnitudes. In additional, changes in scanning performance will influence the repeatability and accuracy of range measurements generated during testing. Therefore during scanning LRF prototype testing, environmental conditions were performed on a stable platform that had little to no influence from vibrational forces. Furthermore, the EEM-FPCB micromirror is still suitable for scanning LRF applications that involve low vibrational influence, such as low-speed indoor AGV's, gesture recognition, and profilometry.

The surface of the object being detected also affects the accuracy of measurements. The receiver relies on the imaging of a diffusely scattered reflection of the scanned laser spot. Therefore, specularly reflective objects (mirrors, shiny metals, etc.) will potentially result in range measurement inaccuracies due to insufficient collection of the laser spot illumination by the receiving lens. In addition, the color of the object also affects the power intensity of the diffusely reflected scanned laser spot. White color surfaces have a higher diffuse reflectivity compared to black surfaces which absorbed a majority of incident laser power (especially for infrared wavelengths). The diffusely reflected power intensity imaged onto the PSD, greatly influences its response accuracy. To avoid these inaccuracies within scanning LRF measurements, the materials chosen for testing have little to no specular reflectivity and have surface with relatively bright colors with great diffuse reflectivity.

5.2.2 Laser Eye Safety

The prototype is intended for potential applications in gesture recognition and close-range obstacle detection. Therefore, the laser must be eye-safe during operation. Laser safety calculations (see appendix) are performed using the international laser safety standard "IEC 60825-1" [72] and "Eye-safety for scanning laser projection systems" [73].

Three IR lasers of 2-mW (Laser 1), 20-mW (Laser 2), and 100-mW (Laser 3) are used in the experiment tests. The laser spot sizes are 2 mm, 5 mm, and 2.5 mm respectively. The sizes of the laser spots for each laser are what was currently available by the manufacturer and required customization (with increase cost) for different sized laser spots. All divergence angles are less than 1.5 mrad. The laser classes for all three lasers are 3B, which are considered non-hazardous to the skin and diffuse viewing, however hazardous to direct continuous-wave (CW or non-modulated) beam viewing [74]. The lasers are scanned at 100 Hz with 30° FOV. In order to achieve a Laser class of 1 (eye-safe), modulation is required. For example, all lasers need to be modulated at a repetition frequency of 1 kHz with required pulse durations of ≤170 µs, ≤3.2 µs, and ≤650 ns for Laser 1, 2, and 3 respectively. Safety calculations can be found in the appendix.

The overall response time of the current PSD and its signal processing circuit, i.e., the amplifier, combined is tested to be 125 µs. This response time can satisfy the requirement of detecting a laser pulse duration of 170 µs (using Laser 1), a faster overall response time is required for measurements using Laser 2 and Laser 3. The current 45 mm 1D PSD alone has a response time of 2.7 µs for a reverse voltage of 15 V, which can be further halved (i.e., 1.3 µs) by doubling the reverse voltage according to the PSD manufacturer. With this response time, the required amplifier response time should be ≤1.9 μs for processing a 3.2 μs pulse duration required by the measurement using Laser 2, which can be achieved by a customized amplifier according to the PSD manufacturer.

For the measurement using Laser 3, a 20 mm 1D PSD with a faster response time of 250 ns can be achieved, but with the sacrifice of a smaller receiver FOV; e.g. reduced to 23° from 48°. In this case the required amplifier response time must be ≤400 ns for processing a 650 ns pulse duration required by measurements with Laser 3. Such a high speed amplifier can be customized according to the PSD manufacturers. In this paper we use Laser 2 & 3 without modulation (i.e., laser on continuous mode) to conduct the experiments. It is believed that the testing results without modulation should be equivalent as those with modulation. This is because the modulated pulse duration (3.2 μs and 650 ns) is long enough for the PSD to respond.

5.2.3 Experimental Results 1 (Eye-Safety Considered – With Modulation)

A FPGA LabVIEW program (see appendix) has been made to acquire data from the scanning laser rangefinder prototype and generate distance measurements. As mentioned earlier, the EEM-FPCB micromirror scans at 100 Hz for 30° scanning FOV.

For each scanning cycle, 10 distance measurements are recorded. These 10 distance measurements are recorded for 10 scanning cycles, producing one frame of distance measurements along the scanned line. This results in a total of 100 measurements each frame with a refresh rate of 10 Hz. The 100 distance measurements are evenly distributed within the 30° FOV. A flat white boards is used for distance measurement testing, shown in Figure 5-6

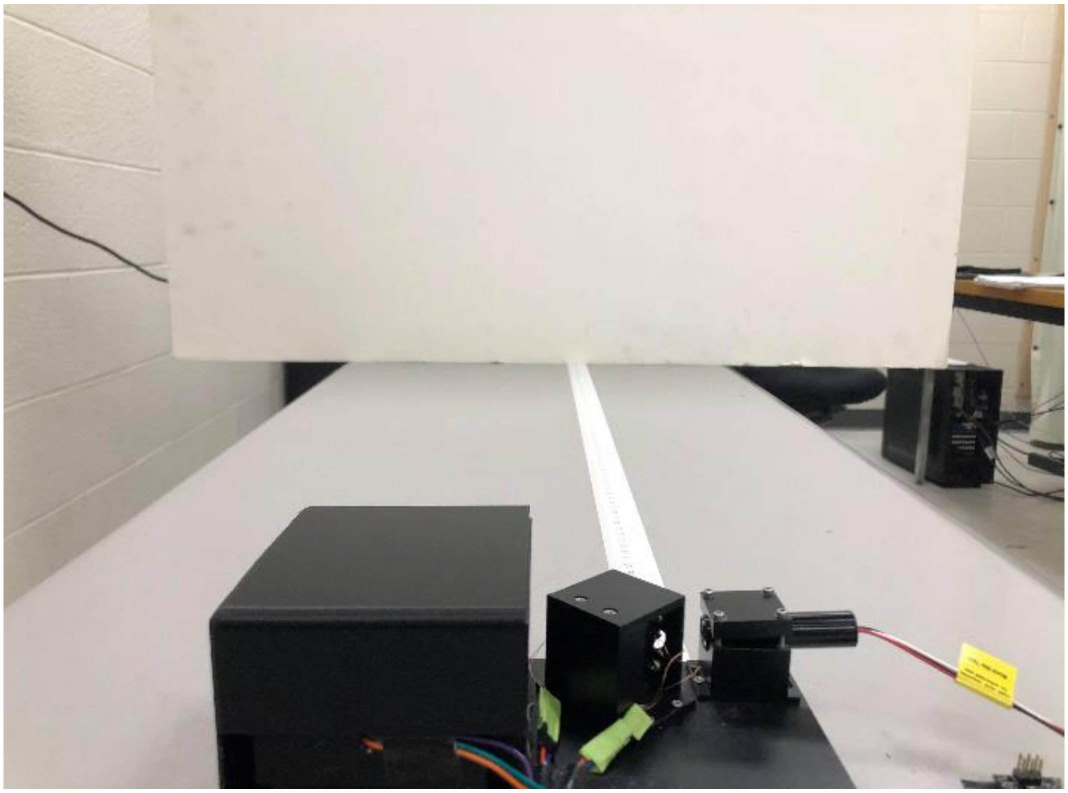

Figure 5-6: Testing setup using a flat white board.

Laser 1 is used for testing with the flat white board placed at 15 cm and 20 – 60 cm with the increment of 10 cm, which is the perpendicular distance ($D_{\perp}$) between the base line B (see Figure 5-2) to the white board, while *D* is the diagonal distance from the FPCB micromirror center to the object (Figure 5-2).

Laser 2 is used for testing with the flat white board placed at 15 cm and 20 – 130 cm with the increment of 10 cm (perpendicular distance $D_{\perp}$). Laser 3 is used for testing using the flat white board placed at 15 cm and 20 – 200 cm with the increment of 10 cm (perpendicular distance $D_{\perp}$). Figures 5-7, 5-8, and 5-9 shows the experimental results of measuring the diagonal distance *D* (as shown in Figure 5-2) using Laser 1, 2, and 3 respectively. White board at perpendicular distances 15 – 30 cm are partially detected, because at close ranges the scanned laser spot doesn't fall completely within the field of view of the receiver. The long dashed and small dashed square region in Figures 5-7 to 5-9, show where experimental measured diagonal distances had an error of ≤10% and ≤5% relative to the real distances respectively.

Measurements using Laser 1 provide a measuring range of 15 – 60 cm (≤ 10% error) for -15° to -3° and 15 - 60 cm (≤ 5% error) for -15° to -6°, shown in Figure 5-7. Measurements using Laser 2 provide a measuring range of 15 – 130 cm (≤ 10% error) for -15° to 10° and 15 - 110 cm (≤ 5% error) for -15° to 8°, shown in Figure 5-8. Measurements using Laser 3 provide a measuring range of 15 – 180 cm (≤ 10% error) for -15° to 11° and 15 – 140 cm (≤ 5% error) for -15° to 9° shown in Figure 5-9. Laser 3 is to be hypothetically used with a smaller 1D PSD of 20 mm in order to achieve a faster overall response time explained in section 5.2.2. Therefore, the detectable field of view of the receiver decreases. The measurements within the green border shown in Figure 5-9 are the values that would be detected using the smaller 1D PSD of 20 mm. The raw laser scanning range measurement performance of each laser is tabulated in Table 8.

Table 8: Raw laser scanning range measurement performance

Laser	Measuring Range	FOV	Relative Error
1	15 – 60 cm	-15° to -3°	≤ 10%
		-15° to -6°	≤ 5%
2	15 – 130 cm	-15° to 10°	≤ 10%
	15 – 110 cm	-15° to 8°	≤ 5%
3	15 – 180 cm	-15° to 11°*	≤ 10%
	15 – 140 cm	-15° to 9°**	≤ 5%

*becomes -15° to 9°, due to smaller PSD

**becomes -15° to 8°, due to smaller PSD

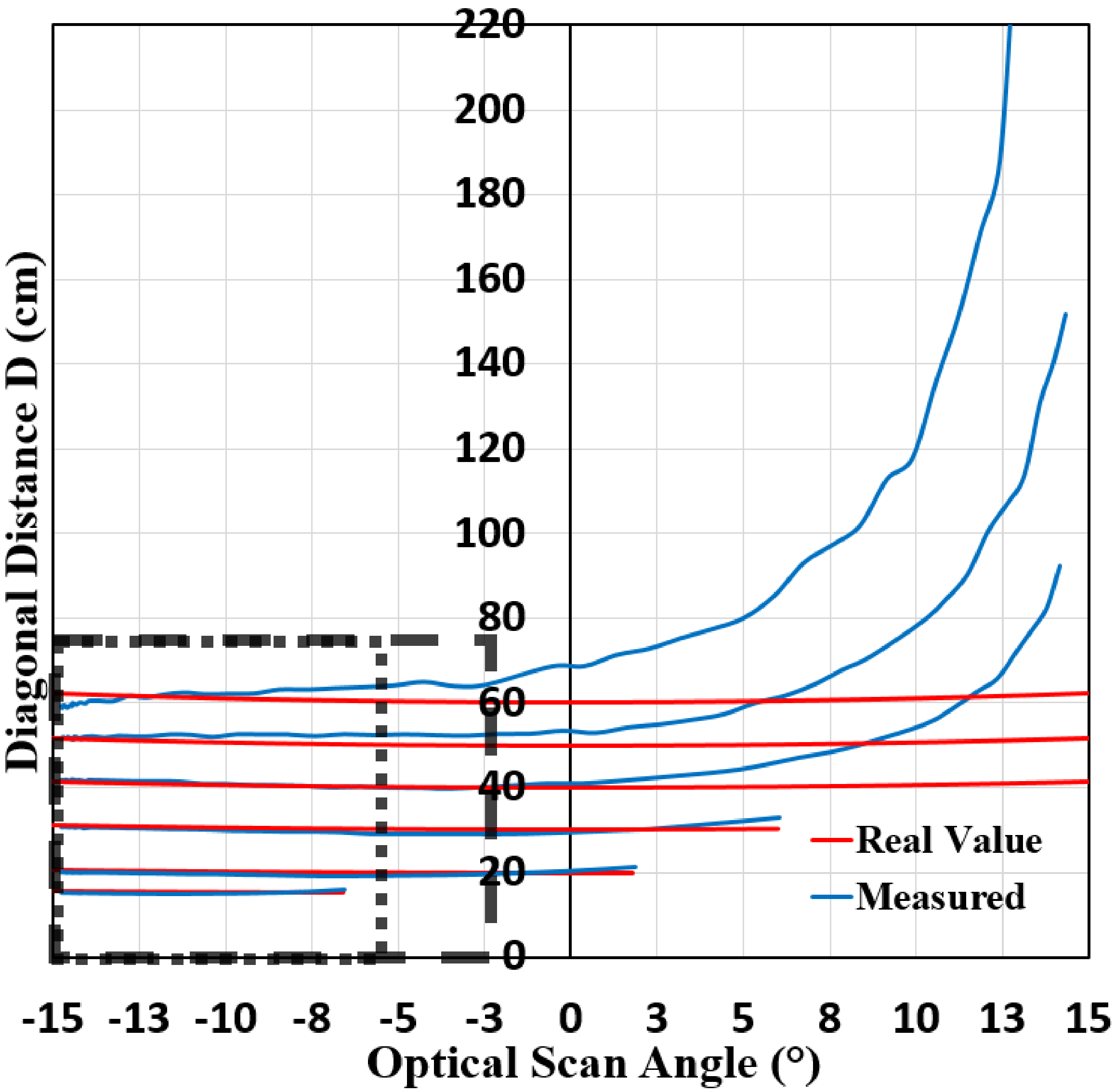

Figure 5-7: Flat white board detection results using Laser 1

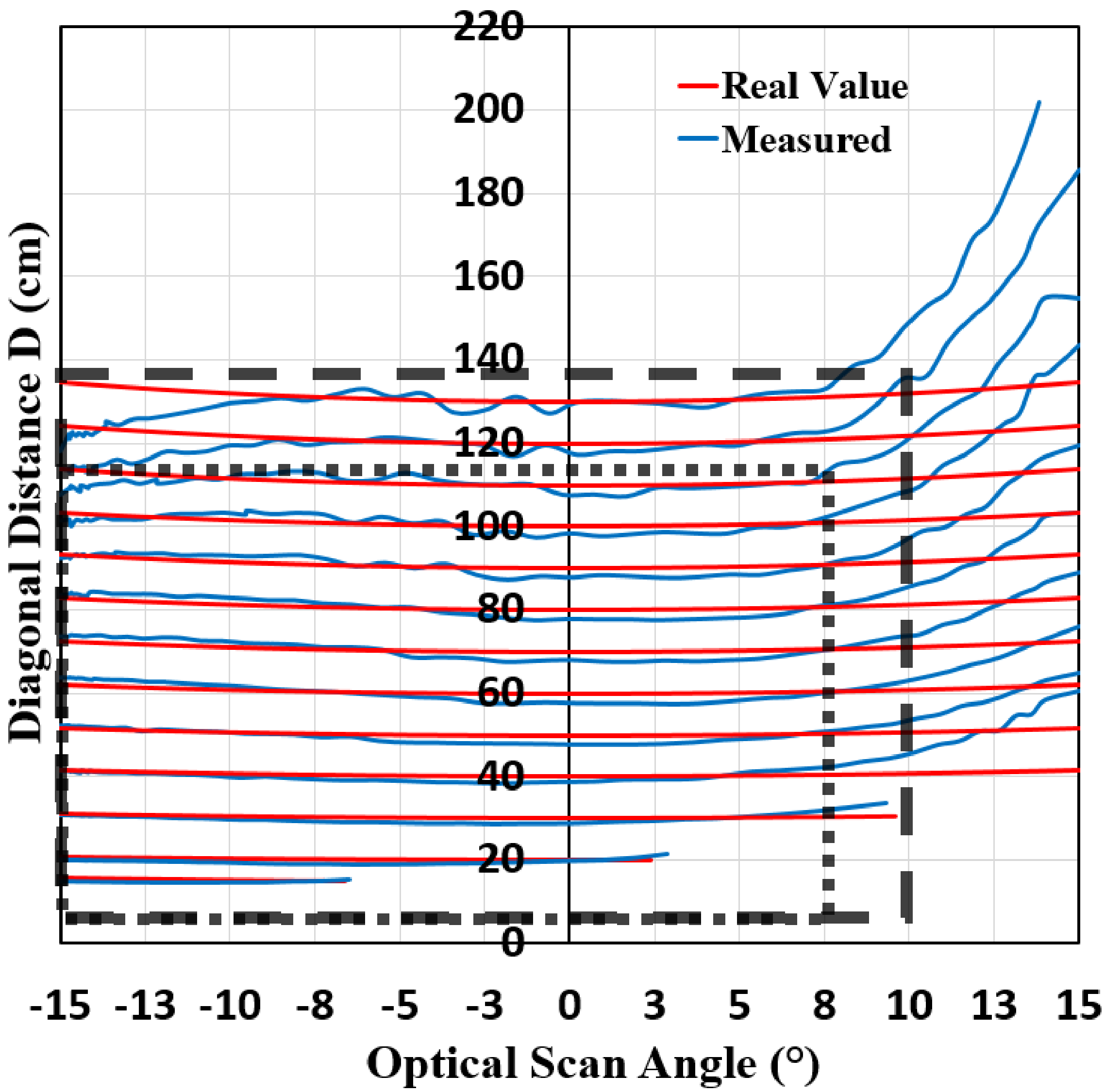

Figure 5-8: Flat white board detection results using Laser 2

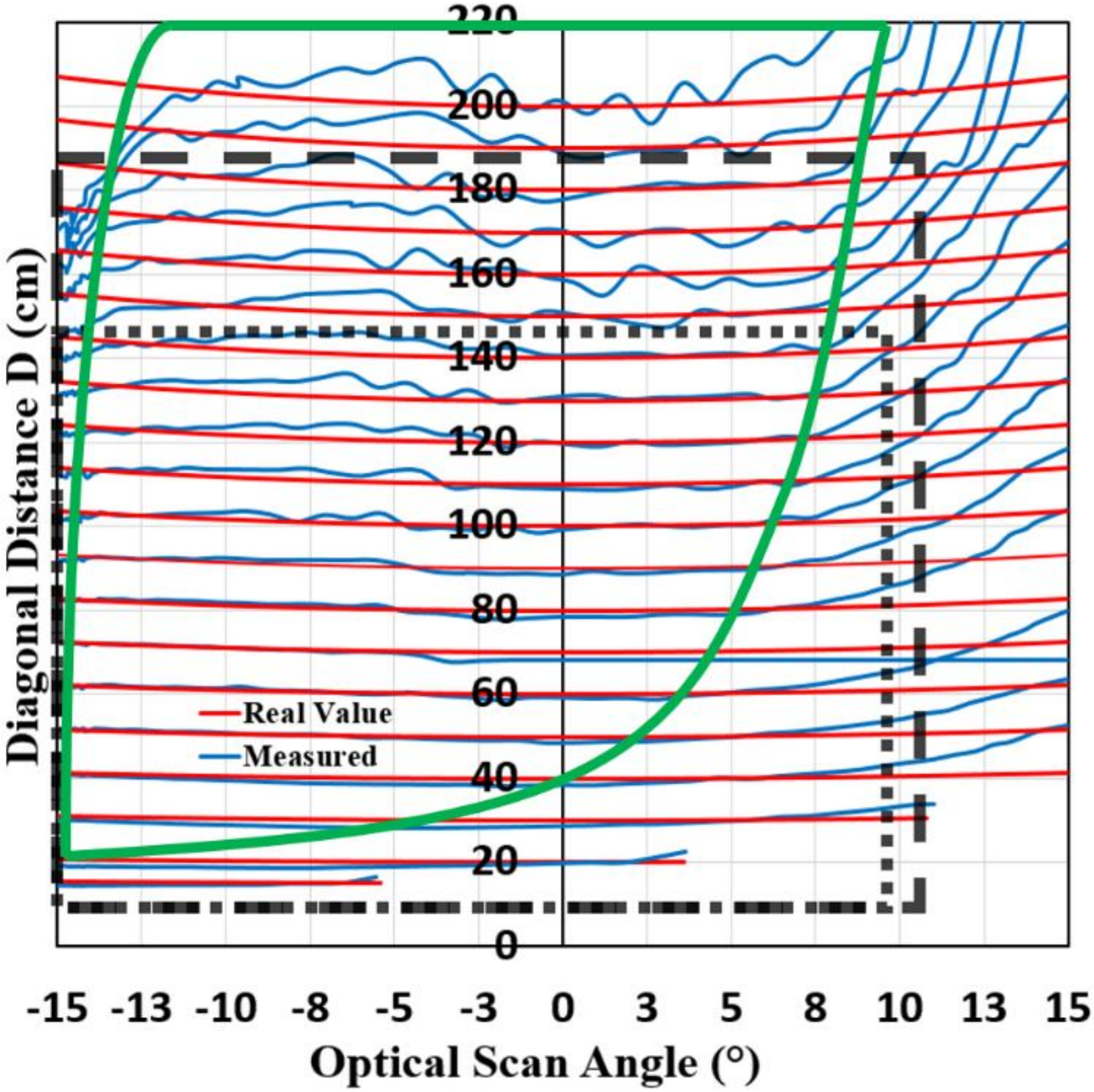

Figure 5-9: Flat white board detection results using Laser 3

The LRF's measurement error comes from the inaccuracy in PSD's measurement in X (see Figure 5-2 and Equation 5), which is mainly caused by: 1) low laser power received by the PSD; 2) aberrations; 3) misalignment; and 4) ambient light. The laser spot power imaged onto the PSD decreases with the increasing object distance. In addition, the aberration increases when the laser spot is further away from the receiving lens optical axis, due to the use of a single lens [75]. Aberrations distribute the imaged laser power over a large non-circular area on the PSD, resulting in inaccurate readings. Proper alignment between the scanned laser spot, receiving lens and PSD is crucial to ensure the scanning laser spot is imaged adequately onto the PSD.

The problem of low laser power can be improved by using a higher power laser (Laser 2 and Laser 3) to increase the detecting range and SNR (Signal-to-Noise). The use of a multiple lens optical receiver could be used to solve the problem of optical aberrations by providing improved imaging quality. However, such a multiple lens optical receiver is costly and difficult to align, thus a single lens optical setup is used in this thesis.

5.2.4 Calibration Method

A calibration method is proposed to increase the measurement accuracy. This method is explained using the measurements with Laser 1 as an example. Calibrations are conducted for the perpendicular distance ($D_{\perp}$) of 20, 30, 40, 50, 60, and 70 cm from angles of -15° to 10°. At each perpendicular distance, the error ΔX, between measured distance of the laser spot image on the PSD, i.e., $X_{measure}$ and expected value $X_{expected}$ obtained from Equations 5 and 6 is the function of $S°$ as shown in Equation 7, which can be approximated using a third-order polynomial in Equation 8. Figure 5-10 shows the example of $\Delta X \ for \ D_{\perp} = 50$ cm.

$$\Delta X = X_{expected} - X_{measure} \tag{7}$$

$$\Delta X = (a_0 S^{\circ 3} + a_1 S^{\circ 2} + a_2 S^{\circ} + a_3) \tag{8}$$

Thus, the calibration leads to 6 polynomials for 6 perpendicular distances ($D_{\perp}$) when using Laser 1. Each measurement needs to go through 3 steps to get the final result. The **1st step)**:

generating a raw perpendicular distance ($D_{\perp_0}$) according to the measurement, based on which a pre-calibrated polynomial is found, whose corresponding perpendicular distance is the closest to $D_{\perp_0}$; **2nd step)**: use the polynomial found in **1st step** and the measured S°, to calculate the ΔX and add it to the measured X, which is used to calculate new perpendicular distance ($D_{\perp_1}$). Based on this $D_{\perp_1}$, find a new pre-calibrated polynomial whose corresponding perpendicular distance is the closest to $D_{\perp_1}$; **3rd step**): use the polynomial found in **2nd step** and the measured $S^{\circ}$to calculate the ΔX and add it to the measured X, which is to be used to calculate the diagonal *D* using Equations 5 and 6.

Calibrations for measurements using Laser 2 is at the perpendicular distances ($D_{\perp}$) of 20 – 130 cm with the increment of 10 cm for the angle range of -15° to 15°. Calibration for measurements using Laser 3 is at the perpendicular distances of ($D_{\perp}$) 20 – 200 cm with the increment of 10 cm for -15° to 15°.

The calibration method improves the measurement accuracy and widens measurement angles. Measurements of an optical post (13 mm thick) at various locations are used to verify the calibration method as shown in Figure 5-11(a). Tables 9, 10 and 11 show the measured results ($D_{measured}$) and the error between the measured and real (D_{real}) values when placing the post at diagonal distances and angles for measurements using Lasers 1, 2, 3.

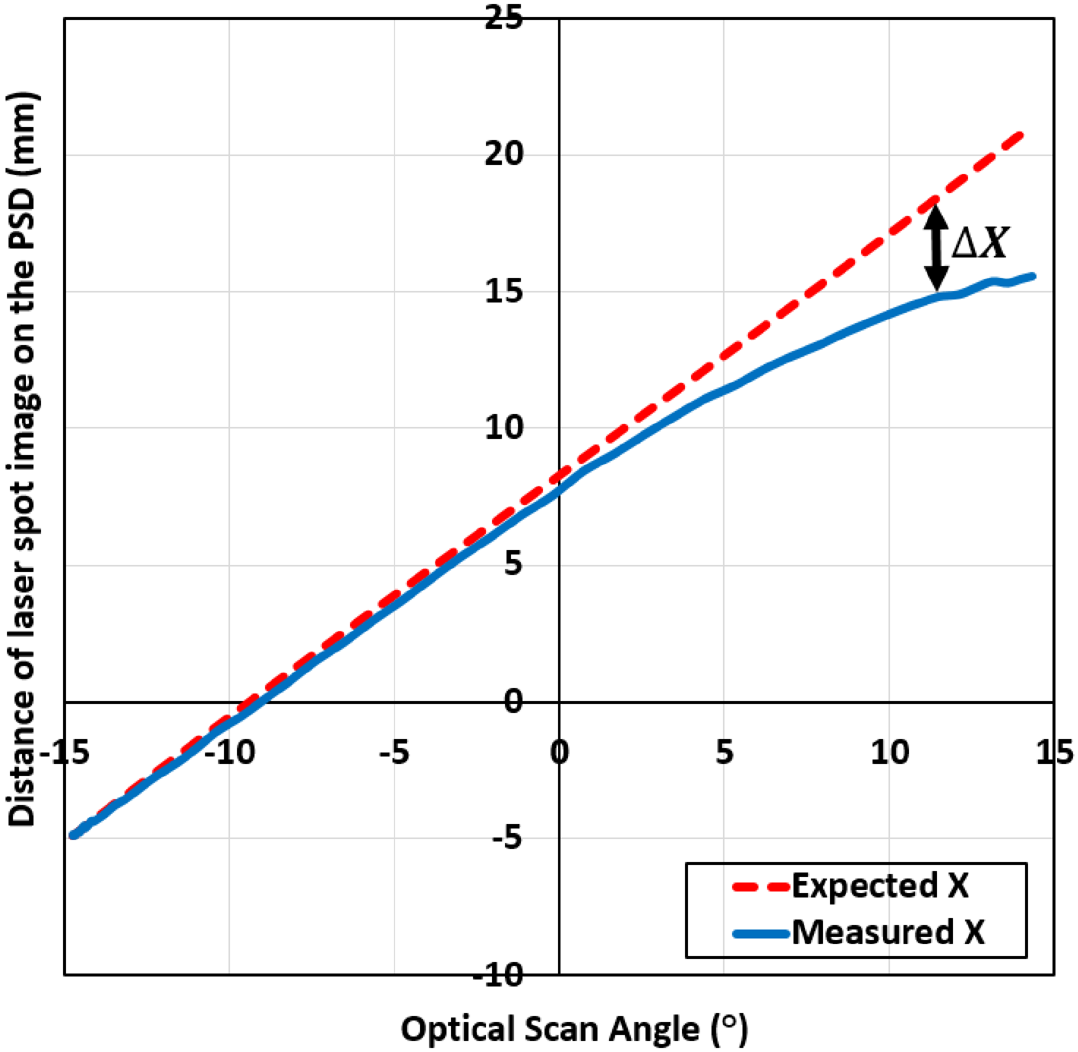

Figure 5-10: Expected (red) and experimental (blue received laser spot distance (X) with respect to optical scan angle.

Table 9: Measured results using calibration method with Laser 1

Location	S°	$D_{Measure}$ (cm)	D_{real} (cm)	Error (%)
1	-15°	26	26.7	2.7
2	-7°	43	44.4	3.3
3	0°	56	57.1	2
4	3°	36	35.6	1.1
5	8°	45	45.2	0.4

Table 10: Measured results using calibration method with Laser 2

Location	S°	$D_{Measure}$ (cm)	D_{real} (cm)	Error (%)
1	-12°	96	96.1	0.1
2	-8°	55	55.9	1.6
3	0°	48	48.1	0.2
4	6°	67	69	2.9
5	12°	65	66.7	2.6

Table 11: Measured results using calibration method with Laser 3

Location	S°	$D_{measure}$ (cm)	D_{real} (cm)	Error (%)
1	-14°	75	75.2	0.3
2	-8°	109	105	3.8
3	0°	55	54.4	1.1
4	7°	113	116.6	3.1
5	14°	85	86.7	2

(a)

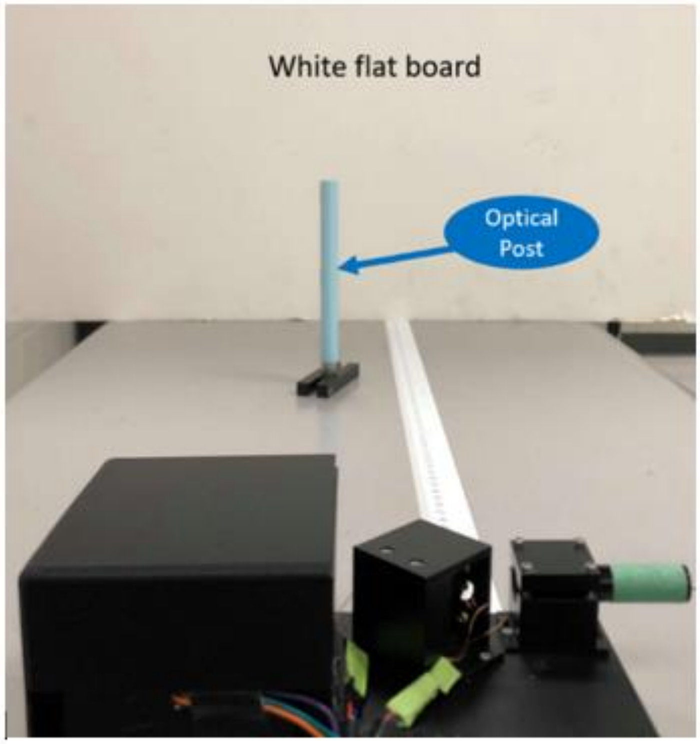

(b)

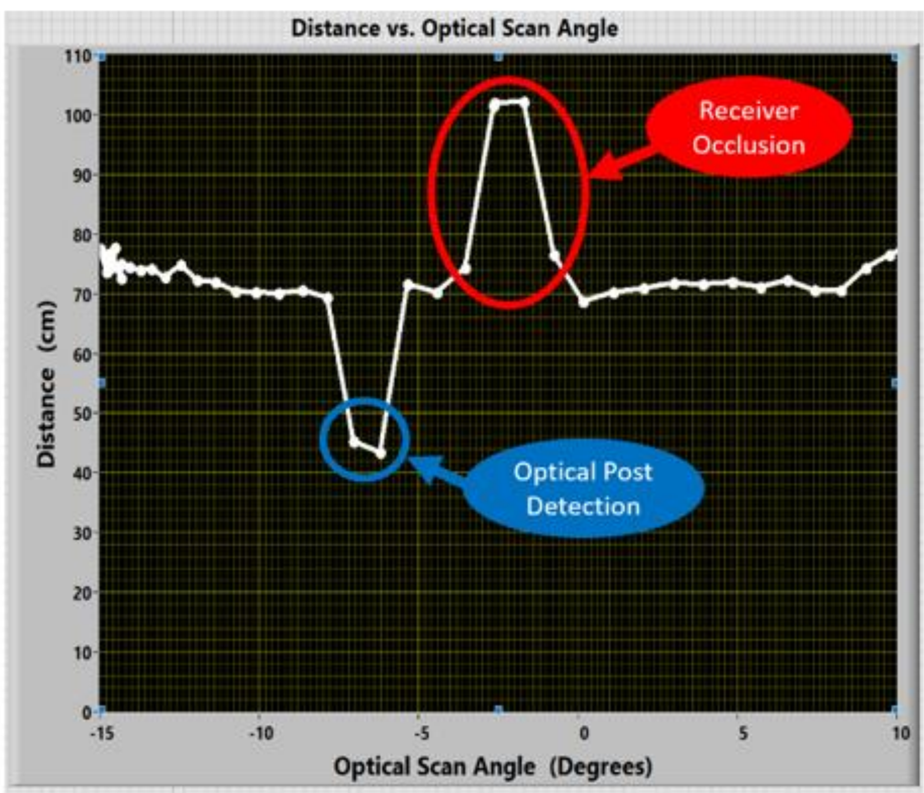

Figure 5-11: Calibrated measurements using Laser 1 and location 2 from Table 9 (a) Setup (b) LabVIEW Real-time graph.

(a)

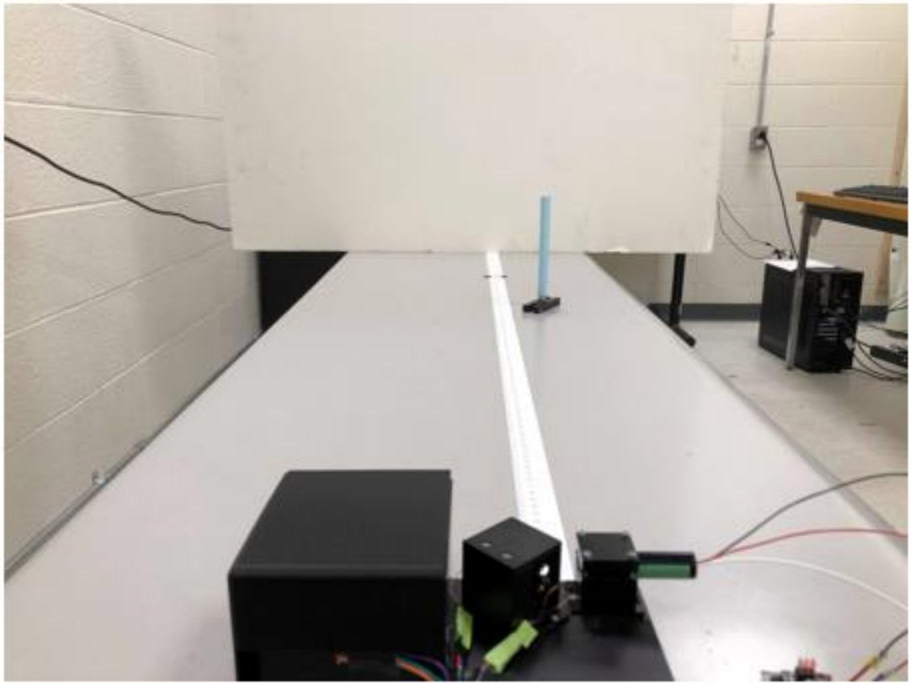

(b)

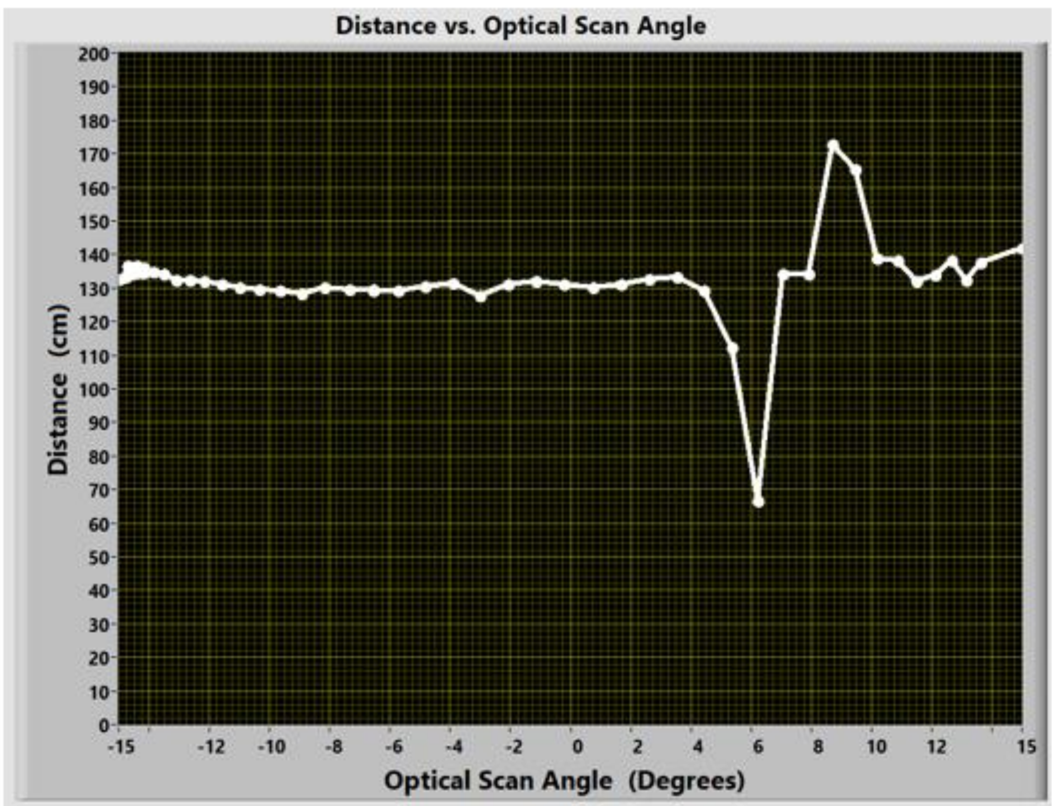

Figure 5-12: Calibrated measurements using Laser 2 and location 4 from Table 10 (a) Setup (b) LabVIEW Real-time graph.

(a)

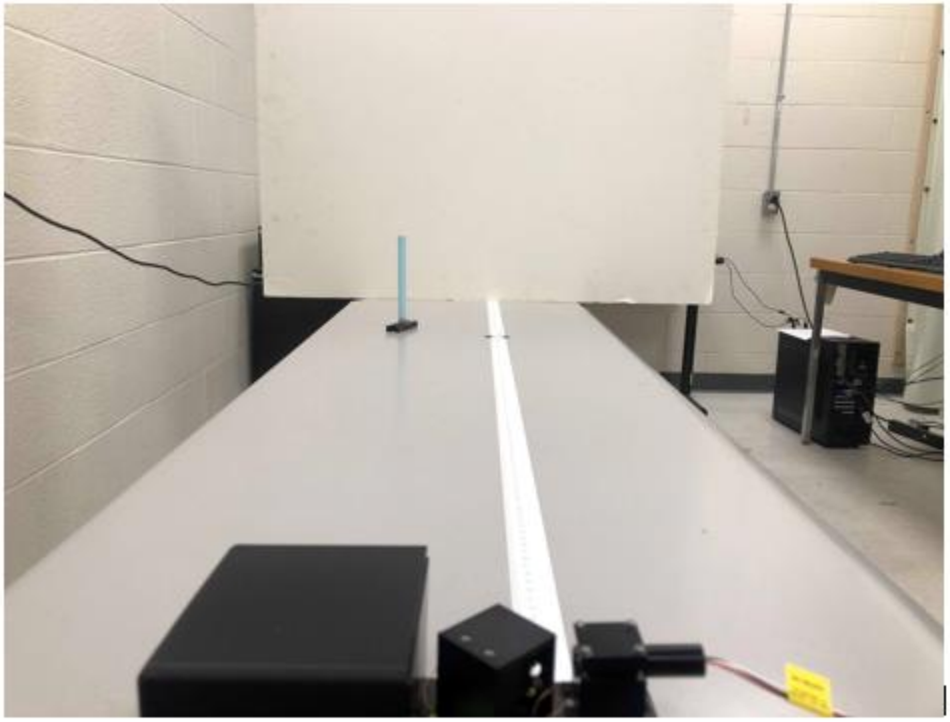

(b)

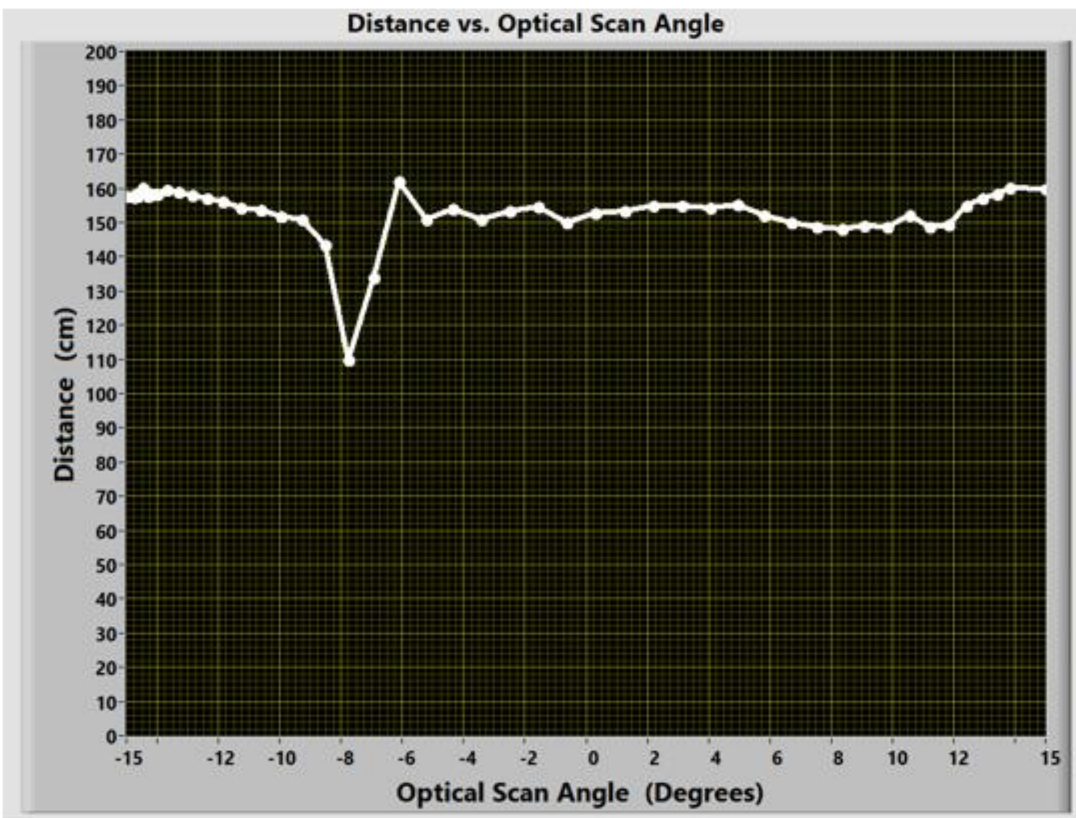

Figure 5-13: Calibrated measurements using Laser 3 and location 2 from Table 11 (a) Setup (b) LabVIEW Real-time graph.

During tests, a flat white background is placed at 70 cm, 130 cm, and 150 cm as background for Lasers 1, 2, and 3 respectively. Figure 5-11(b) shows the real-time graph of measure distance versus optical scan angle generated for the example of Laser 1, D_{real} = 44.4 cm and S° = 7° (Location 2 from Table 9). The blue circle shows the detection of the optical post and the red circle shows the occluded points [76] that are hidden behind the optical post from the receiver. This results in an error PSD reading, due to the absence or partial detection of the laser spot when scanning at that angle. To alleviate the problem of occlusion [76], an additional receiver can be used to improve detectability of the scanned laser spot. However, this is not implemented in this paper due to the increase in size and cost. Figure 5-12(a) shows the setup of testing laser 2 with the optical post placed at Location 4 from Table 10. Figure 5-12(b) shows the real-time graph of measure distance versus optical scan angle generated from the setup in Figure 5-12(a). Figure 5-13(a) shows the setup of testing laser 3 with the optical post placed at Location 2 from Table 11. Figure 5-13(b) shows the real-time graph of measure distance versus optical scan angle generated from the setup in Figure 5-13(a).

With the calibration method, the measuring range using Laser 1 is 15 – 70 cm with ≤ 4% error for -15° to 10°; Measurement using Laser 2 has a measuring range of 15 – 130 cm with ≤ 4% error for -15° to 15°; Measurement using Laser 3 has a measuring range of 15 – 200 cm with ≤ 4% error for -15° to 15° (becomes 5°~9° because a smaller is PSD used). The improvement brought by the calibration method is significant. The laser scanning range measurement performance of each laser using the calibration method is tabulated in Table 12.

Table 12: Laser scanning range measurement performance using the calibration method

Laser	Measuring Range	FOV	Relative Error
1	10 – 70 cm	-15° to 10°	≤ 4%
2	15 – 130 cm	±15°	≤ 4%
3	15 – 200 cm	±15°*	≤ 4%

* becomes 5°~9° because a smaller is PSD used

5.2.5 Experimental Results 2 (Eye-Safety Not Considered – No Modulation)

Higher powered lasers can be used without modulation (continuous mode without eye-safety considered) for laser scanning rangefinding applications that are far below eye-level (below chest and/or waist level) or operated in an environment that involves the laser directed away from the user's eyes. The laser class for all three laser are 3B, therefore pose no hazard for diffuse view and skin burns. Such applications include low-profile AGV's (Vacuum cleaning robot or automated warehouse delivery cart) or profilometry & 3D scanning.

Experimental tests have been performed using Laser 3 (highest powered laser of the 3 lasers) in continuous mode, which provided greater scanning resolution within range measurements. Range measurements can only be collected when the laser is turned on, which is limited once the laser is modulated. Operating the laser in continuous mode during scanning allowed for more range measurements to be collected per scanning cycle. The sampling rate of range measurements is limited by the faster response times of the PSD and FPGA module, instead of the pulse modulation frequency. The calibration method has been used during measurements, which yielded the same measuring range and accuracy of Laser 3 shown in Table 12 (15 – 200 cm with ≤ 4% error for -15° to 15°).

During tests, a flat white board (used in previous tests) was placed as a background, 200 cm away. A smaller optical scanning FOV of 20° (±10°) at 10 Hz was tested, further improving the scanning measurement resolution, i.e., sampled range measurements distributed throughout a smaller scanned FOV, resulting in denser measurements per frame. This allowed for smaller/thinner objects to be detected, such as a soldering wire (0.4 mm) and Q-Tip (2.5 mm). The sampling rate of range measurements was 10 kHz, programmed using the same FPGA module and LabVIEW. This yielded 1000 range measurement points collected at a refresh rate of 10 Hz, 10 times more points compared to the tests conducted with the lasers modulated for eye-safety (100 points at 10 Hz). The range measurements were plotted on a real-time LabVIEW graph similar to the previous experiments of distance (cm) versus optical scan angle (°).

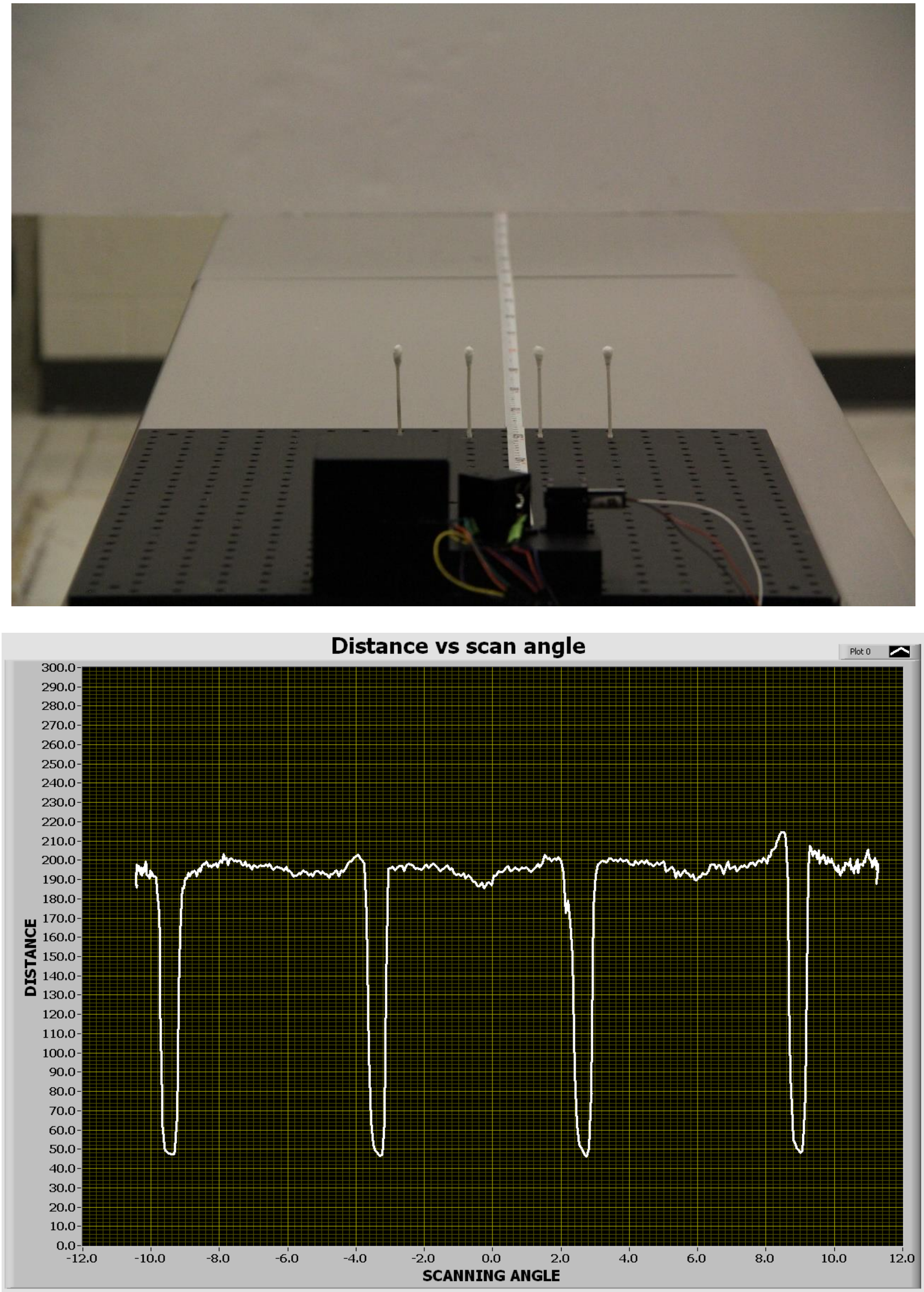

Figure 5-14: (top) setup of 4 Q-tips at 50 cm (bottom) LabVIEW real-time graph

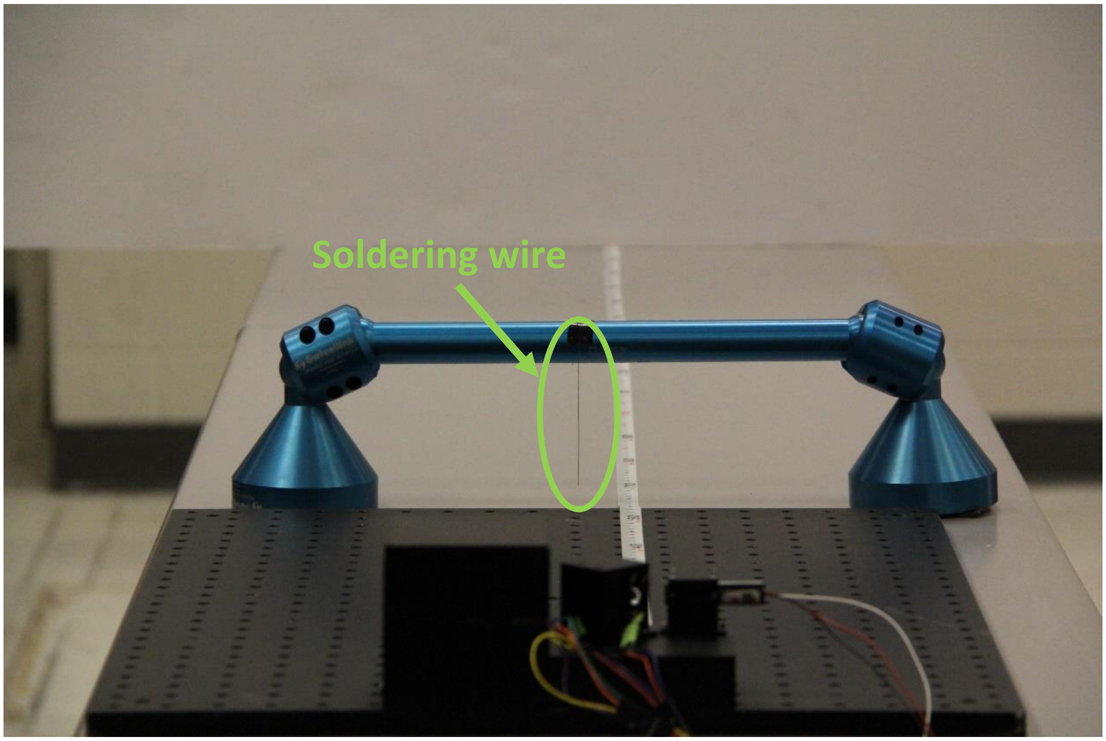

Figure 5-15: (top) setup of a soldering at 60 cm (bottom) LabVIEW real-time graph

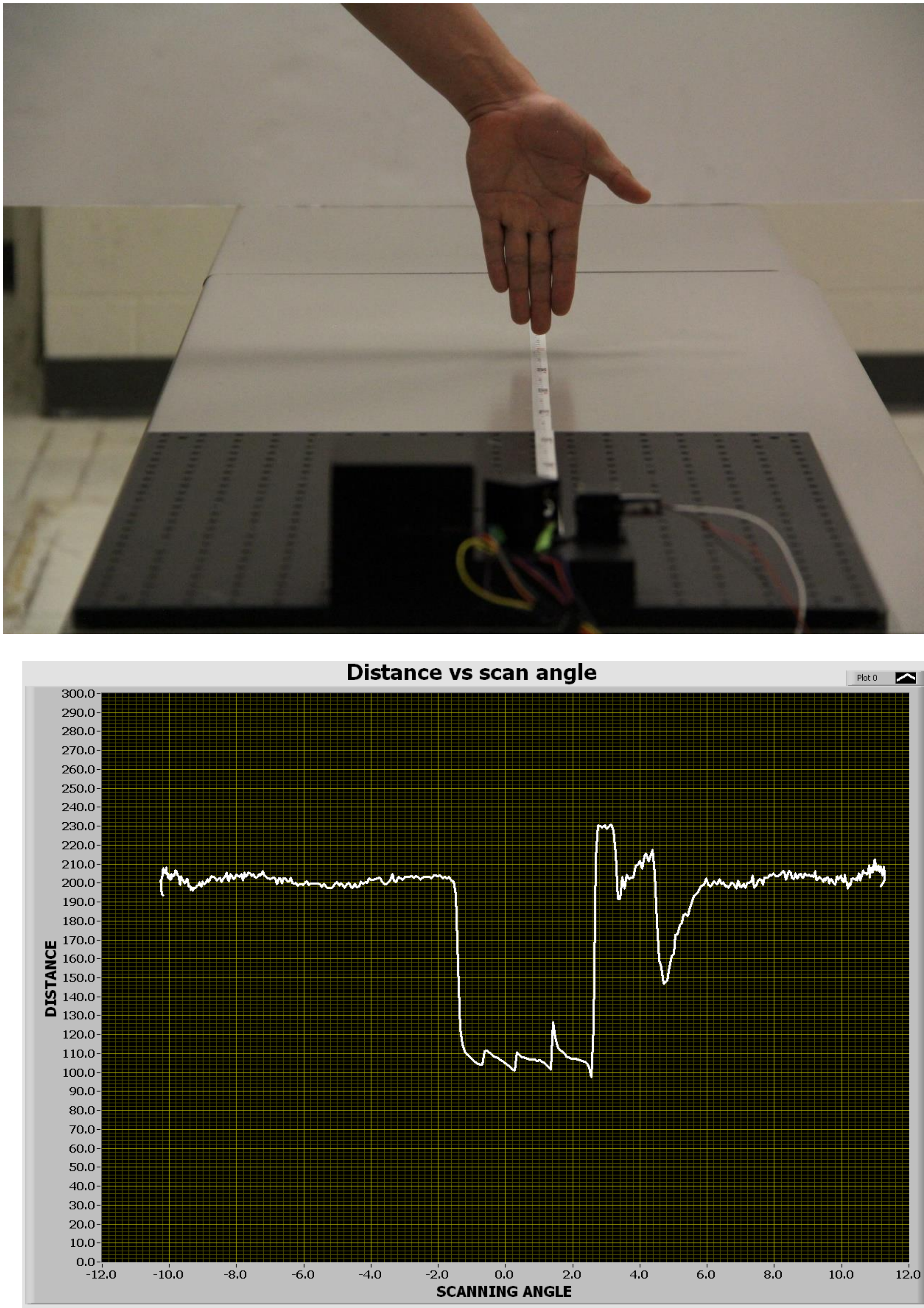

Figure 5-16: (top) setup of hand (fingers closed) at 100 cm (bottom) LabVIEW real-time graph

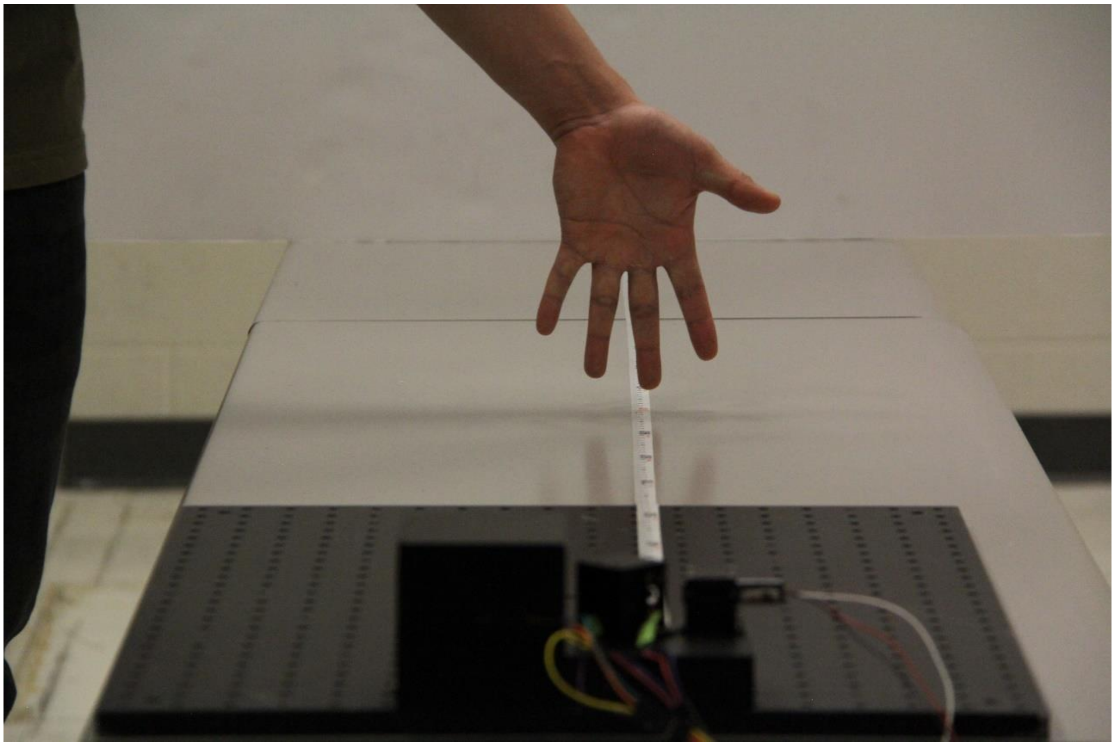

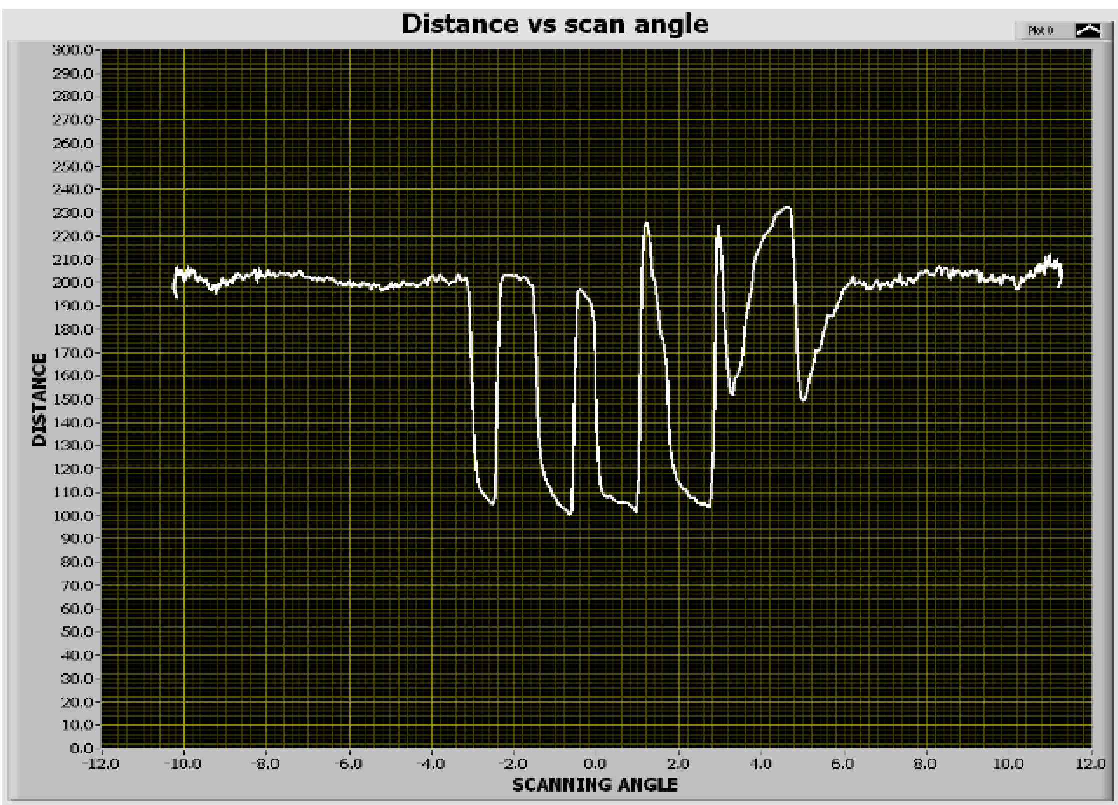

Figure 5-17: (top) setup of hand (fingers open) at 100 cm (bottom) LabVIEW real-time graph

Figure 5-14 (top) shows the setup of 4 Q-tips evenly spread out, all placed at a perpendicular distance ($D_{\perp}$) of 50 cm away. The corresponding LabVIEW real-time graph generated shows the detection of the 4 Q-tips, presented in Figure 5-14 (bottom). The range measurements of all 4 Q-tips are approximately 48~50 cm, close to the real measurement of ≈50 cm.

Figure 5-15 (top) shows the setup of a soldering wire (supported by the blue apparatus, out of the detectable FOV) placed at a perpendicular distance ($D_{\perp}$) of 60 cm away. The corresponding LabVIEW real-time graph generated shows the detection of the soldering, presented in Figure 5-15 (bottom). The range measurements of the soldering wire is approximately 59~60 cm, close to the real measurement of ≈50 cm.

Figure 5-16 (top) and 5-17 (top) shows the setup of a hand with closed and open fingers respectively, both at a perpendicular distance ($D_{\perp}$) of 100 cm away. The corresponding LabVIEW real-time graph generated shows the detection of both the closed and open hand, presented in Figure 5-16 (bottom) and 5-17 (bottom) respectively. The range measurements of both the closed and open hand is approximately 100~105 cm, close to the real measurement of ≈100 cm.

The problem of occlusion (explained in section 5.2.4 and shown in Figure 5-11) wasn't observed during the detection of the relatively thinner objects such as the soldering wire (0.4 mm) and soldering wire (2.5 mm). This is due to the thin size of the objects which didn't create much of an obstruction towards receiver. Conversely, occlusion was evident during the test of the open and closed hand, which is seen as a range measurement spike immediately to the left of the hand detection on the graphs. This is due to the hand being a relatively larger obstruction towards the receiver, which results in the scanning laser spot to fall undetected behind it. The triangulation method for rangefinding isn't immune to the problem of occlusion and potentially causes inaccuracies within readings. The alleviation of this problem has already been discussed in section 5.2.4.

Chapter 6. Conclusion & Future Work

6.1 Contributions

1. Developed an electromagnetic FPCB micromirror based scanner intended for laser rangefinding applications. The FPCB micromirror has a large aperture (8 mm x 5.5 mm) and high flatness (ROC = ~15m), that overcomes conventional MEMS micromirrors' limitation of small aperture (less than 5 mm). Subsequently high powered lasers with large beam sizes and good collimation can be used in micromirror based scanning LRF for better performance. Laser scanning fatigue test have been performed, reaching up to 1.2 billion scanning cycles. This indicates good reliability and durability of the FPCB material for extended long period operation. 2 configurations of the electromagnetic FPCB micromirror scanner has been developed. Both configurations have unique scanning advantages of their own.
    a. The first configuration has a relatively more flexible torsion beam (consisting of copper) which provides a maximum optical scanning FOV of 60^o ($\pm30^o$) at resonance of ≈100 Hz, using a relatively lower voltage. The first configuration is best suited for scanning requirements of a moderately wide optical angle for low to medium speeds (10-100 Hz).
    b. The second configuration has a relatively stiffer beam which is comprised of only polyimide, which provides a wider maximum optical scanning FOV of 100^o ($\pm50^o$) at higher resonance of ≈200 Hz. The second configuration is best suited for scanning requirements of a wide optical angle (≥ 60^o FOV) for relatively higher speeds (≥ 100 Hz).

2. The modelling and prototyping results of the 1st and 2nd configuration designs of the electromagnetic FPCB micromirror scanner have been performed and presented in this thesis. In addition, a journal paper presenting the research results of the 1st configuration design and its application in scanning laser rangefinding, has been submitted and under currently under review by the "Journal of Micromechanics and Microengineering".

Furthermore, a journal paper has been published presenting the research results and performance of the 2^{nd} configuration design to the "Journal of Micromachines"

3. Developed a scanning laser rangefinding prototype using the first configuration design of the electromagnetic FPCB based micromirror scanner, which has been experimentally tested with results presented in this thesis and in a journal paper under review. The prototype developed in thesis has achieved performance better than those (micromirror based LRF or claimed to be used for LRF) reported in literature [46, 77,78]
    a. Three infrared lasers of varying powers have been tested and operated with modulation meeting eye safety standards of class 1M, during scanning laser rangefinding prototyping. The scanning laser rangefinding prototype developed in this thesis meets laser eye safety requirements (Class 1) and has achieved a larger scanning angle and longer detecting distance than those in literature. The scanning laser rangefinding prototype can perform up to a 30^{o} optical scan FOV, collecting 100 range measurement at 10 Hz, up to a range of 200 cm.
    b. Tests and results using the highest powered laser (Laser 3) has been operated in continuous mode (without modulation), providing greater scanning resolution and detection of thinner objects such as a Q-tip and soldering wire.

4. Developed calibration method, improving the measurement accuracy and range of measurements for the scanning laser rangefinding prototype.

5. Developed an FPGA LabVIEW program to collect range measurement data and modulate the lasers for eye safety. The program is also responsible for calibrating collected measurement results and generating a real-time graph of distance measurements versus optical scan angle.

6.2 Future Work

1. Use of the Time-of-Flight (TOF) method for potential further range detection capabilities will be pursued.
2. Use of a high speed PSD amplifier, allowing for the detection of faster pulsed lasers for eye safety.
3. Use of a CMOS image sensor for potential accuracy improvement of position detection of the scanning laser spot.
4. Use of a multiple lens optical receiver for improved imaging quality of the scanned laser spot onto the image sensor for reading.
5. Addition of a second scanning FPCB micromirror to achieve scanning detection in 2 dimensions.
6. Optimization of mechanical parts and housing designs for an improved compact and lightweight design of the overall scanning laser rangefinding prototype.

Appendix A: LabVIEW FPGA & Real-Time Program

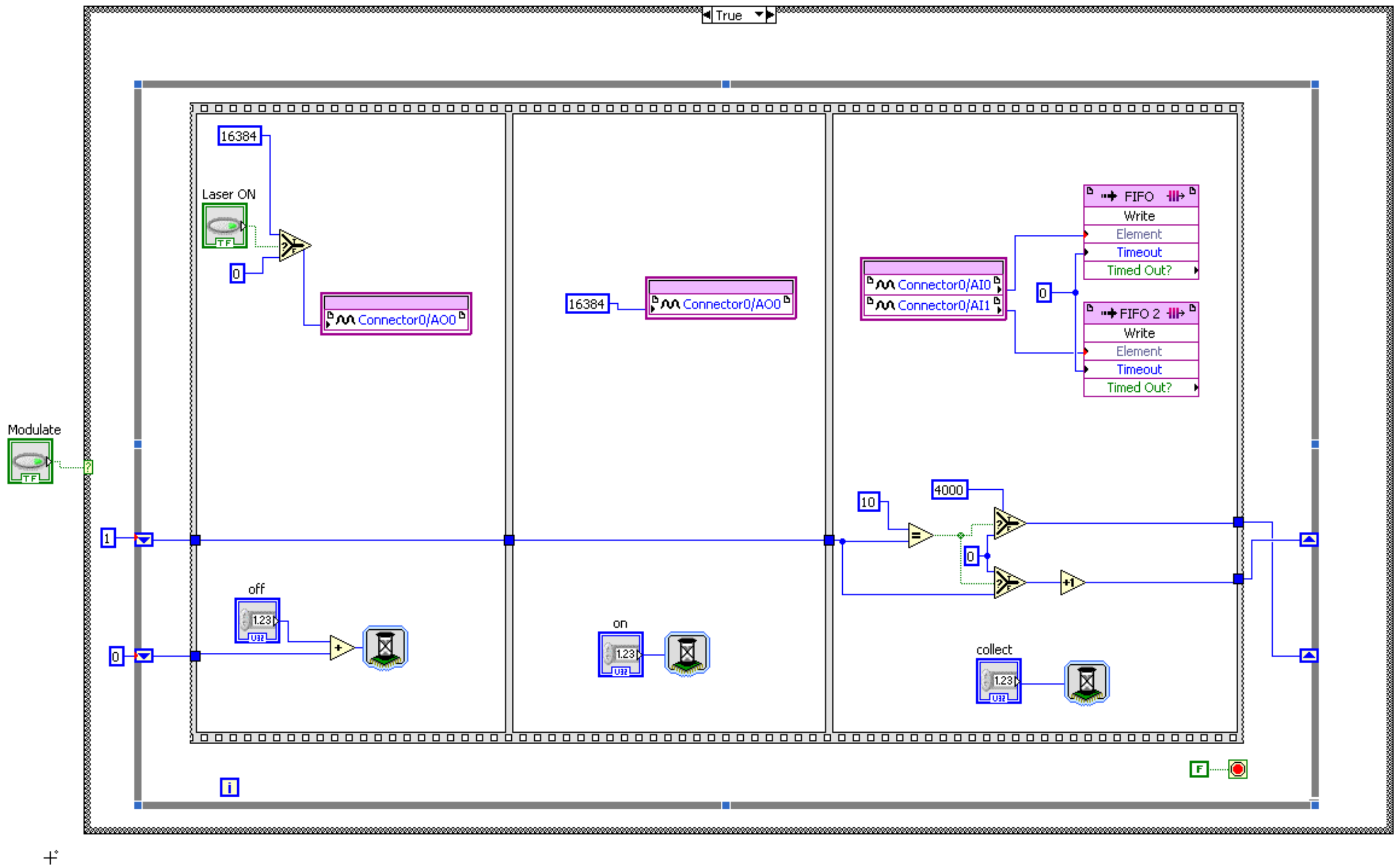

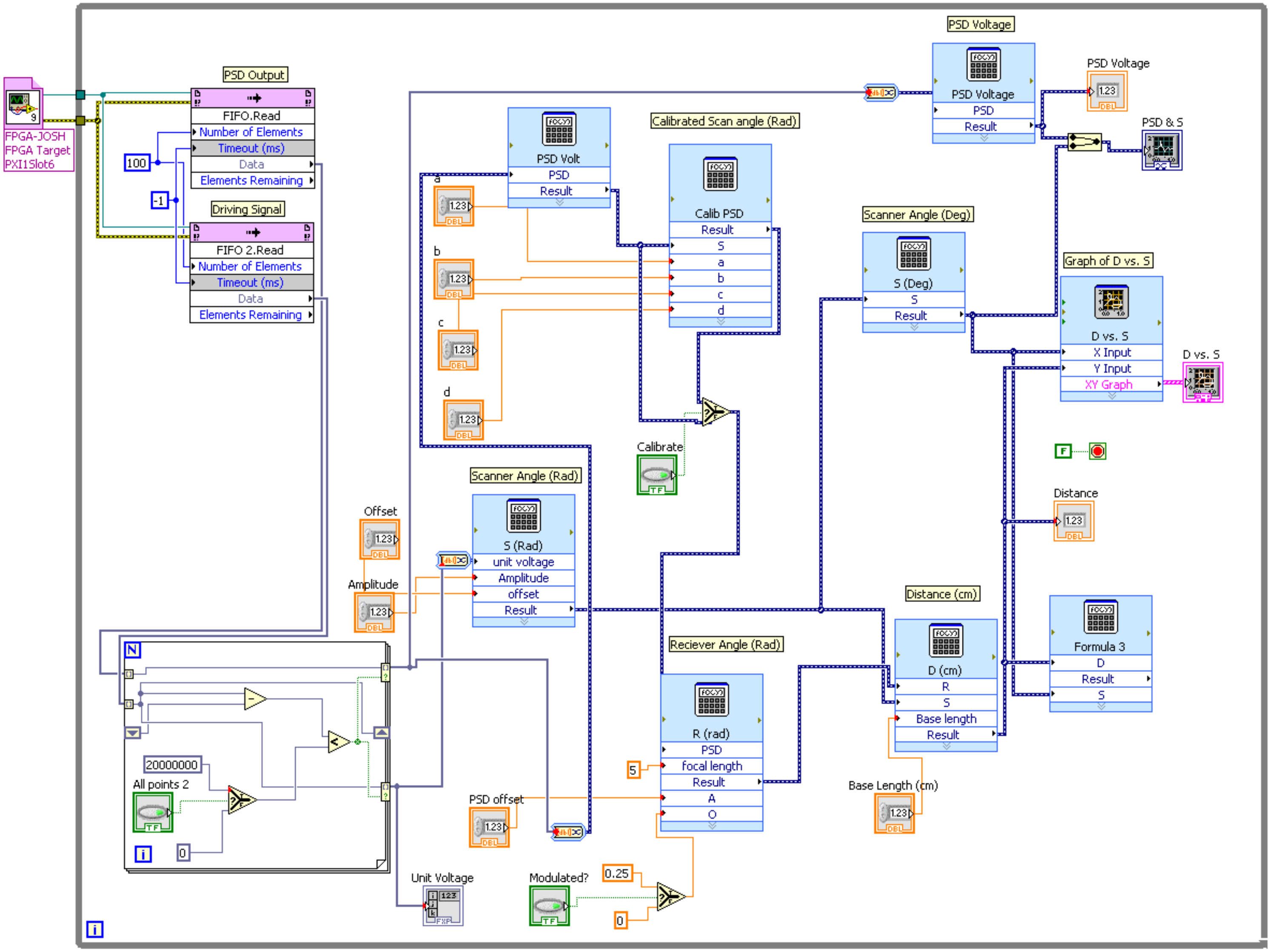
FPGA-JOSH
FPGA Target
PXI1Slot6
PSD Output
FIFO.Read
Number of Elements
Timeout (ms)
Data
Elements Remaining
100
-1
Driving Signal
FIFO 2.Read
Number of Elements
Timeout (ms)
Data
Elements Remaining
PSD Volt
PSD
Result
a
b
c
d
Calibrated Scan angle (Rad)
Calib PSD
Result
S
a
b
c
d
PSD Voltage
PSD Voltage
PSD
Result
PSD Voltage
PSD & S
Scanner Angle (Deg)
S (Deg)
S
Result
Graph of D vs. S
D vs. S
X Input
Y Input
XY Graph
D vs. S
Calibrate
Distance
Scanner Angle (Rad)
S (Rad)
unit voltage
Amplitude
offset
Result
Offset
Amplitude
Distance (cm)
D (cm)
R
S
Base length
Result
Formula 3
D
Result
S
Reciever Angle (Rad)
R (rad)
PSD
focal length
Result
A
O
5
Base Length (cm)
PSD offset
20000000
All points 2
0
Unit Voltage
Modulated?
0.25
0

Appendix B: Mechanical Part Drawings

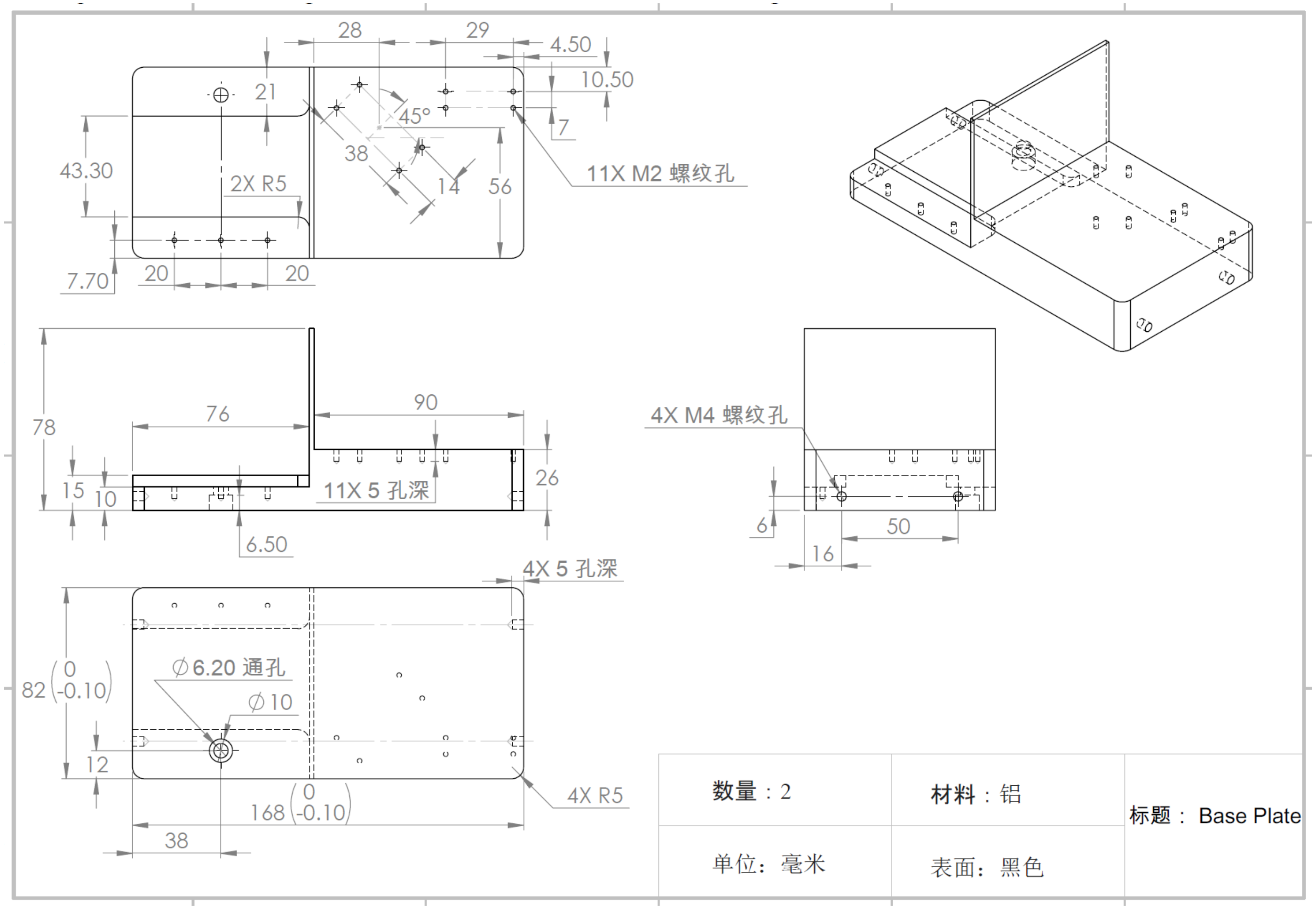

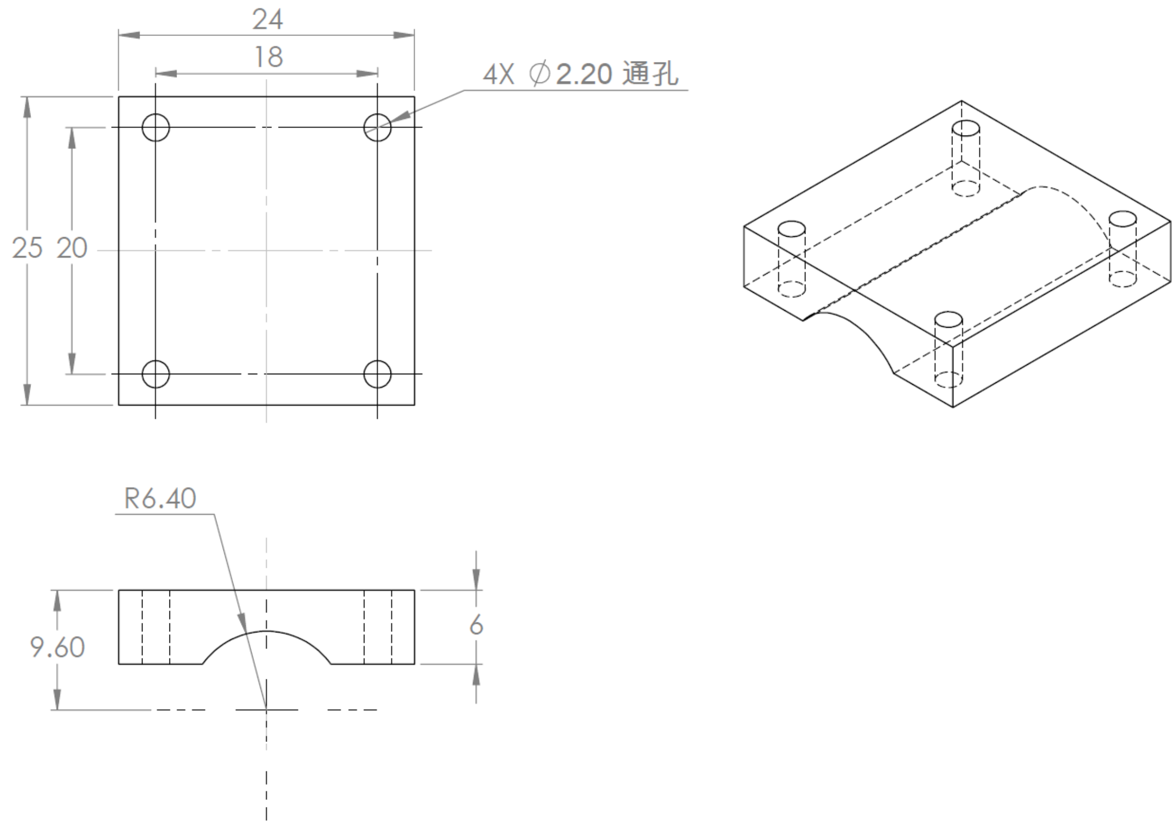

数量：2	材料：铝	标题：Laser Clamp
单位：毫米	表面：黑色	

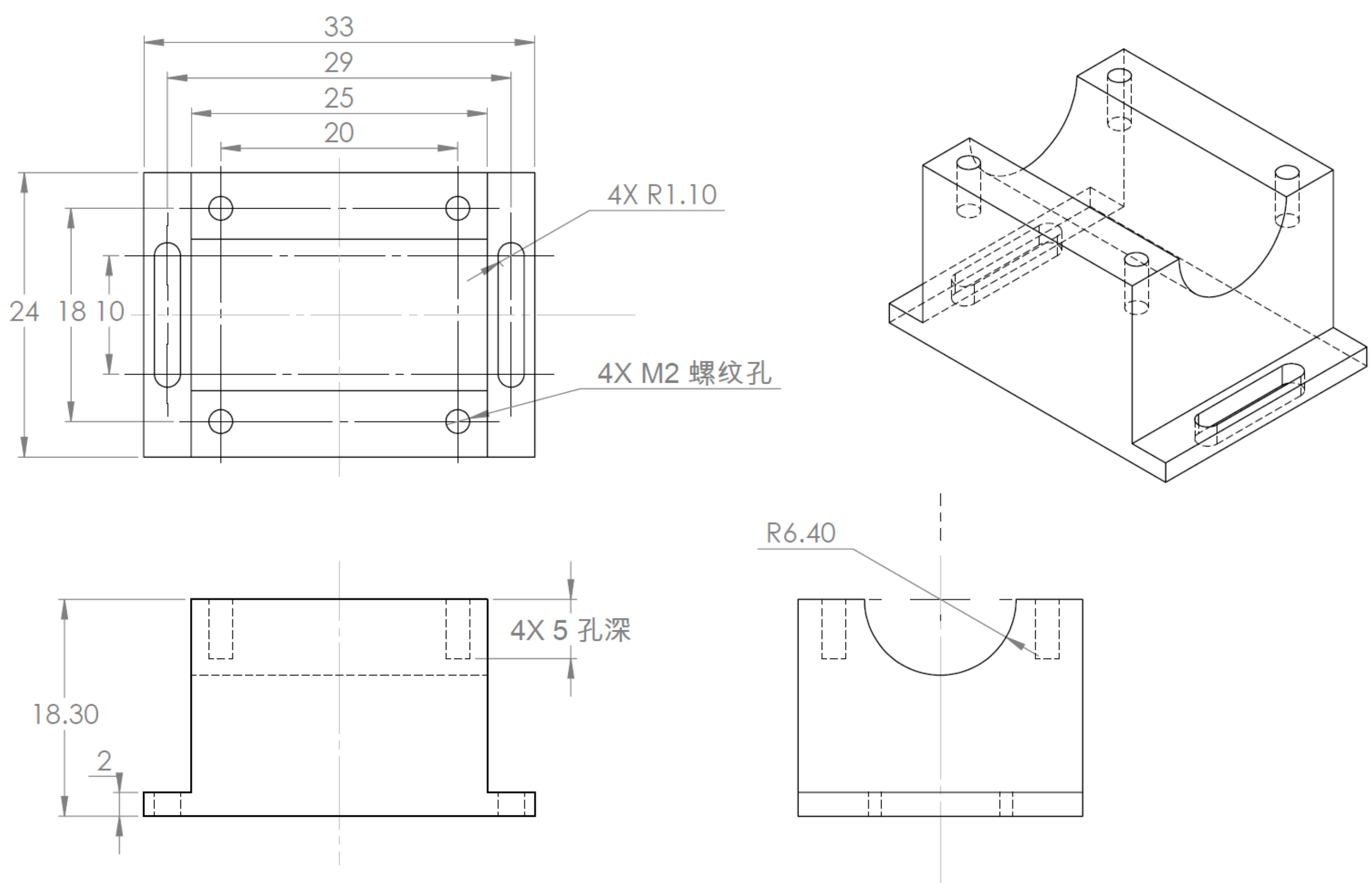

数量：2	**材料**：铝	**标题**： Laser holder base
单位：毫米	表面：黑色	

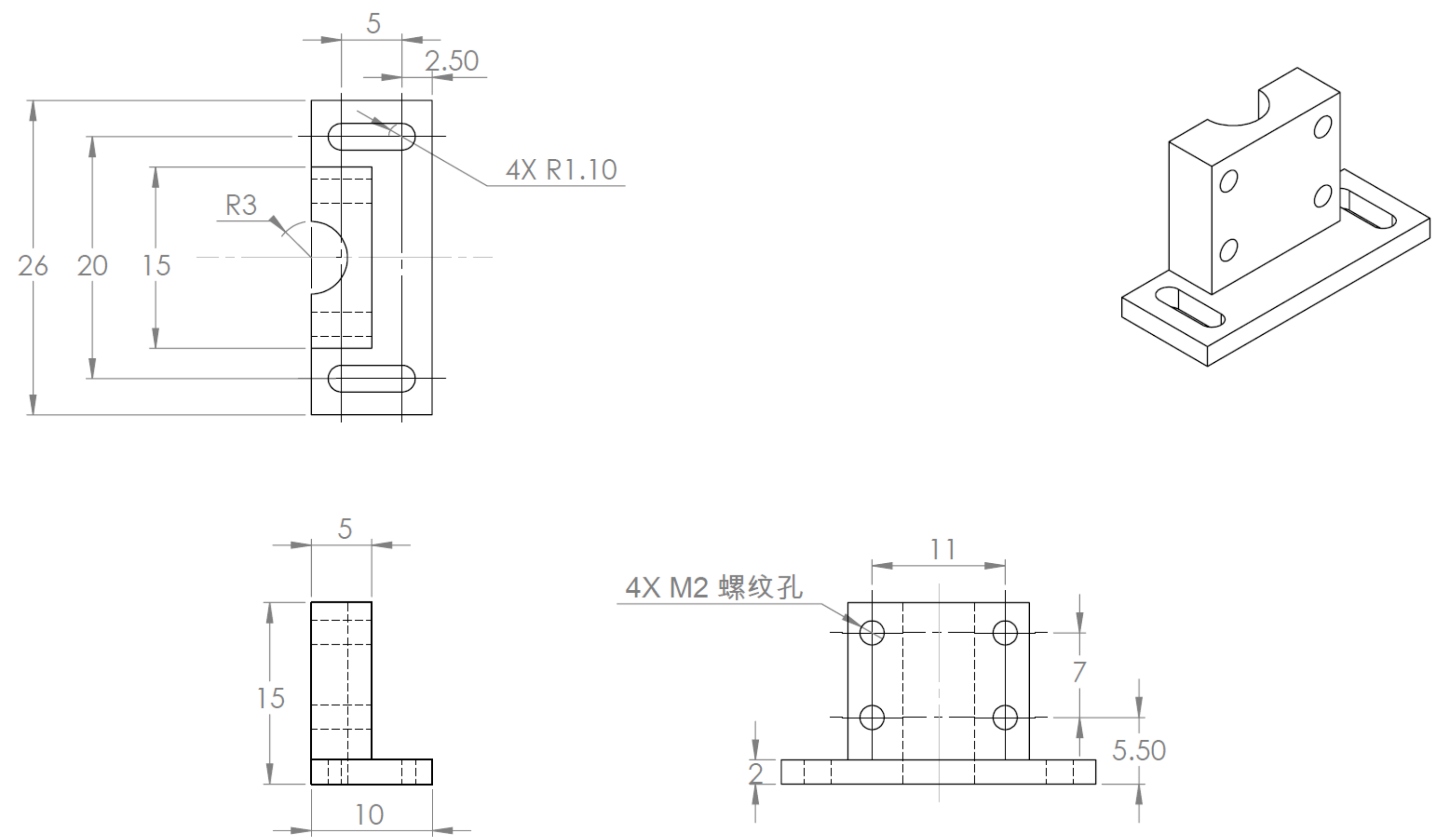

数量：4	材料：铝	标题： Middle solenoid support
单位：毫米	表面：黑色	

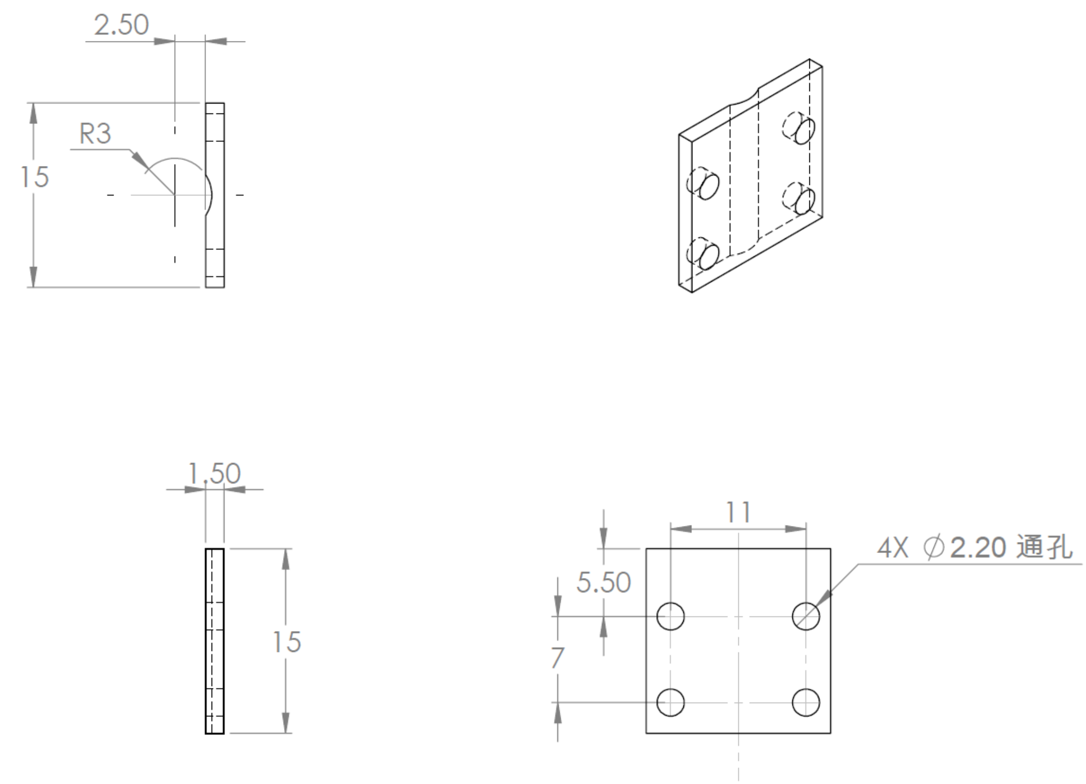

数量：4	材料：铝	标题： Solenoid Clamp
单位：毫米	表面：黑色	

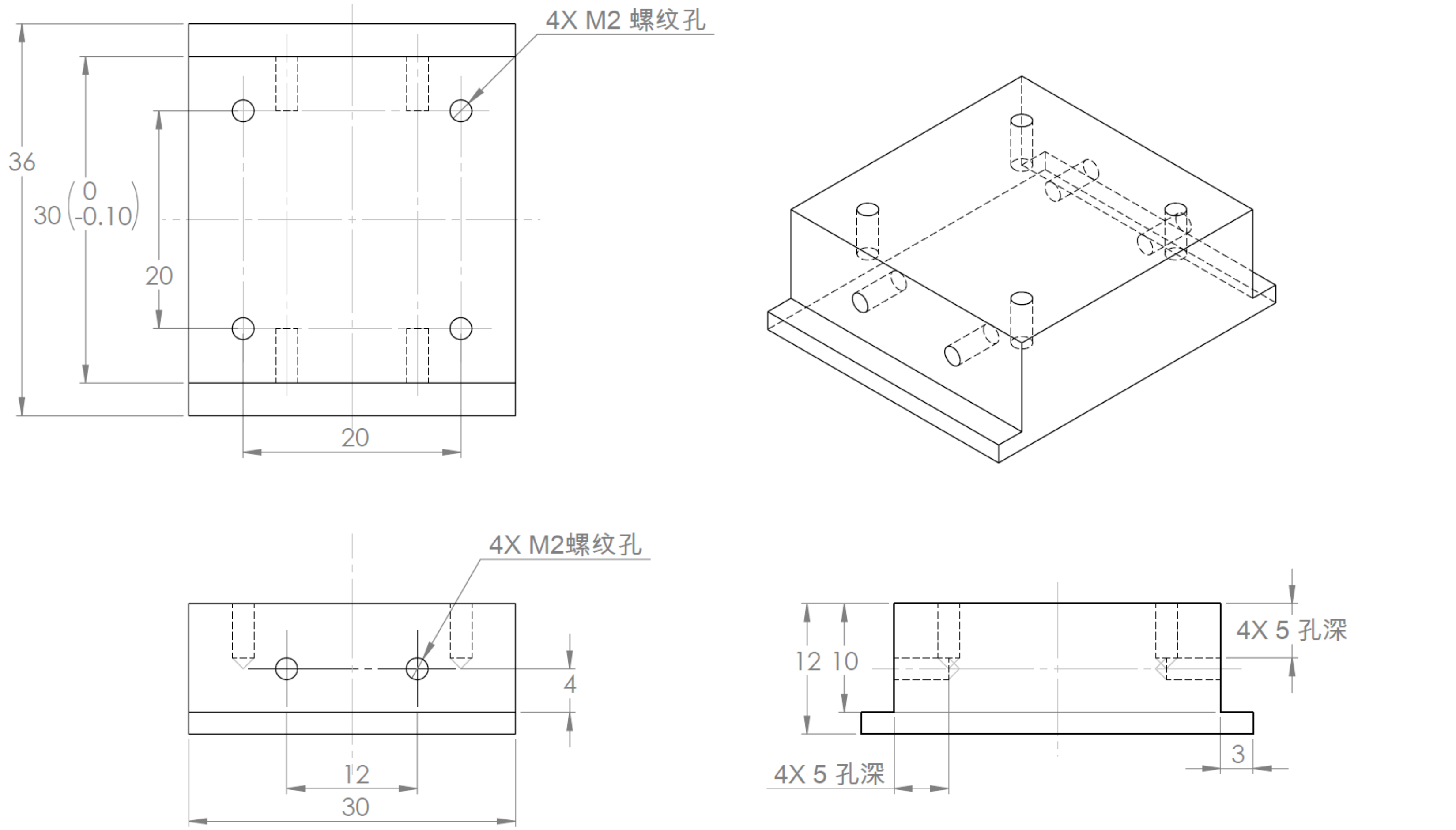

数量：2	材料：铝	标题：Solenoid Slider
单位：毫米	表面：黑色	

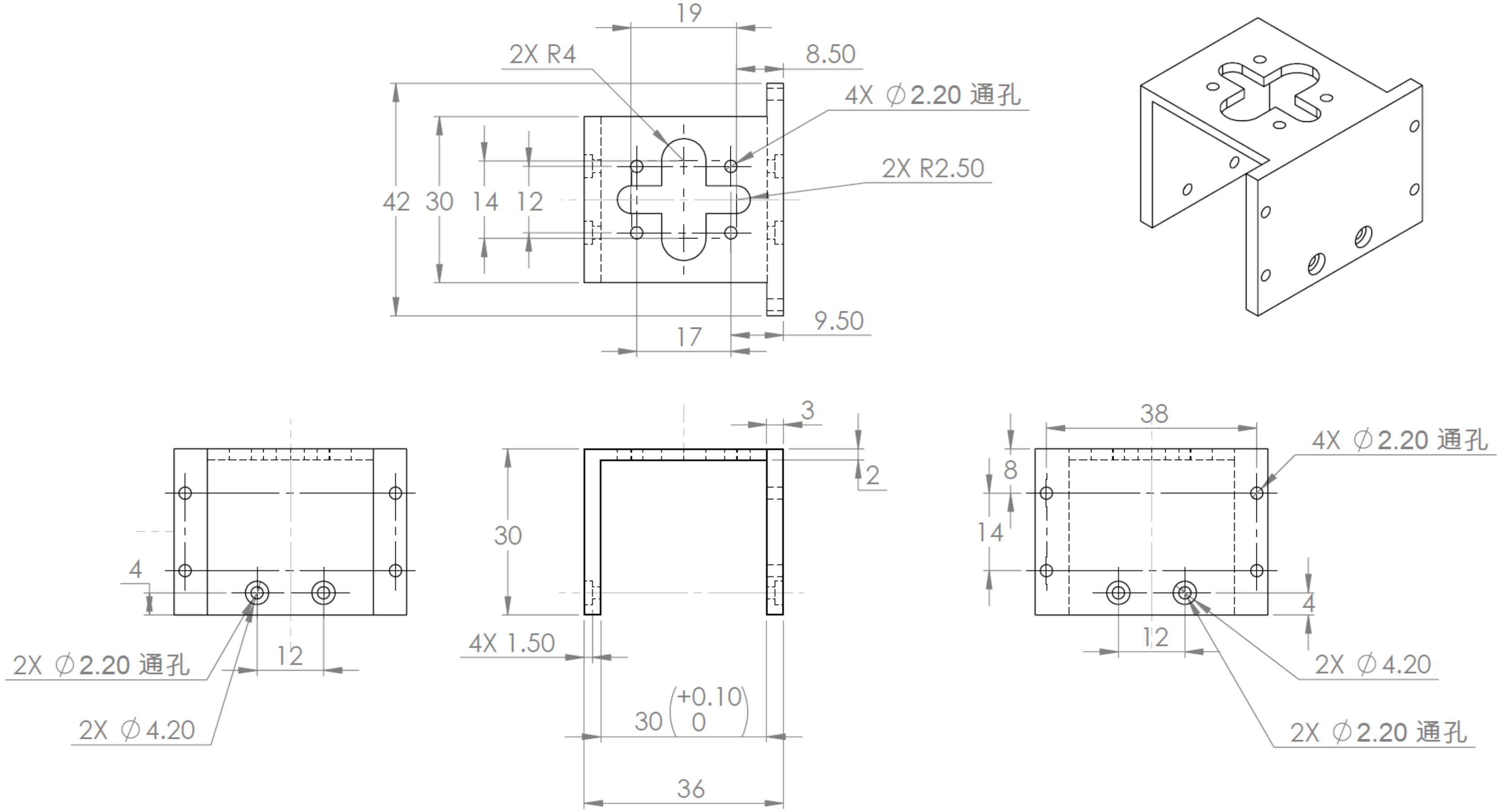

数量：2	材料：铝	标题： Mount
单位：毫米	表面：黑色	

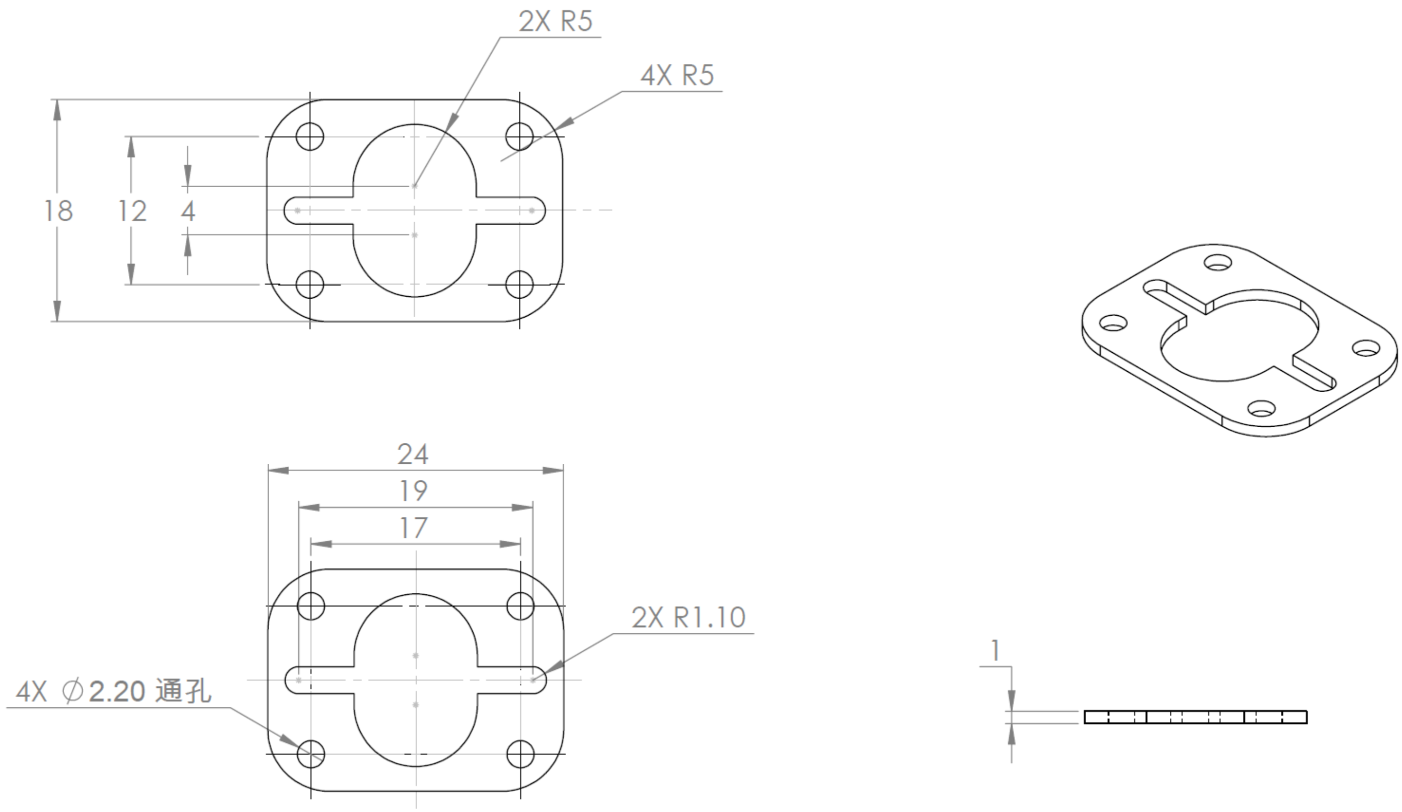

数量：2	材料：铝	标题：FPCB Holder
单位：毫米	表面：黑色	

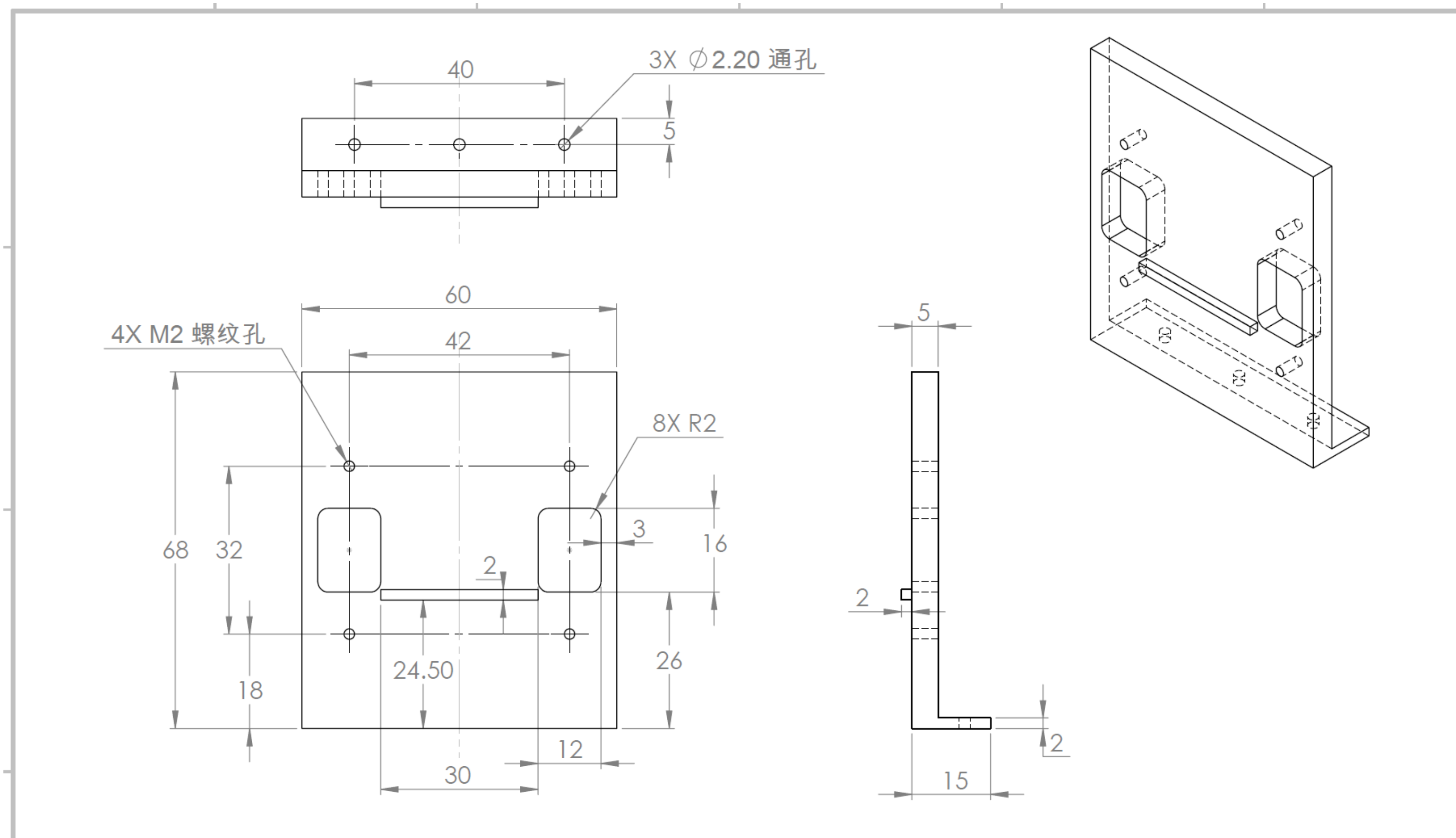

数量：2	材料：铝	标题：PSD Holder
单位：毫米	表面：黑色	

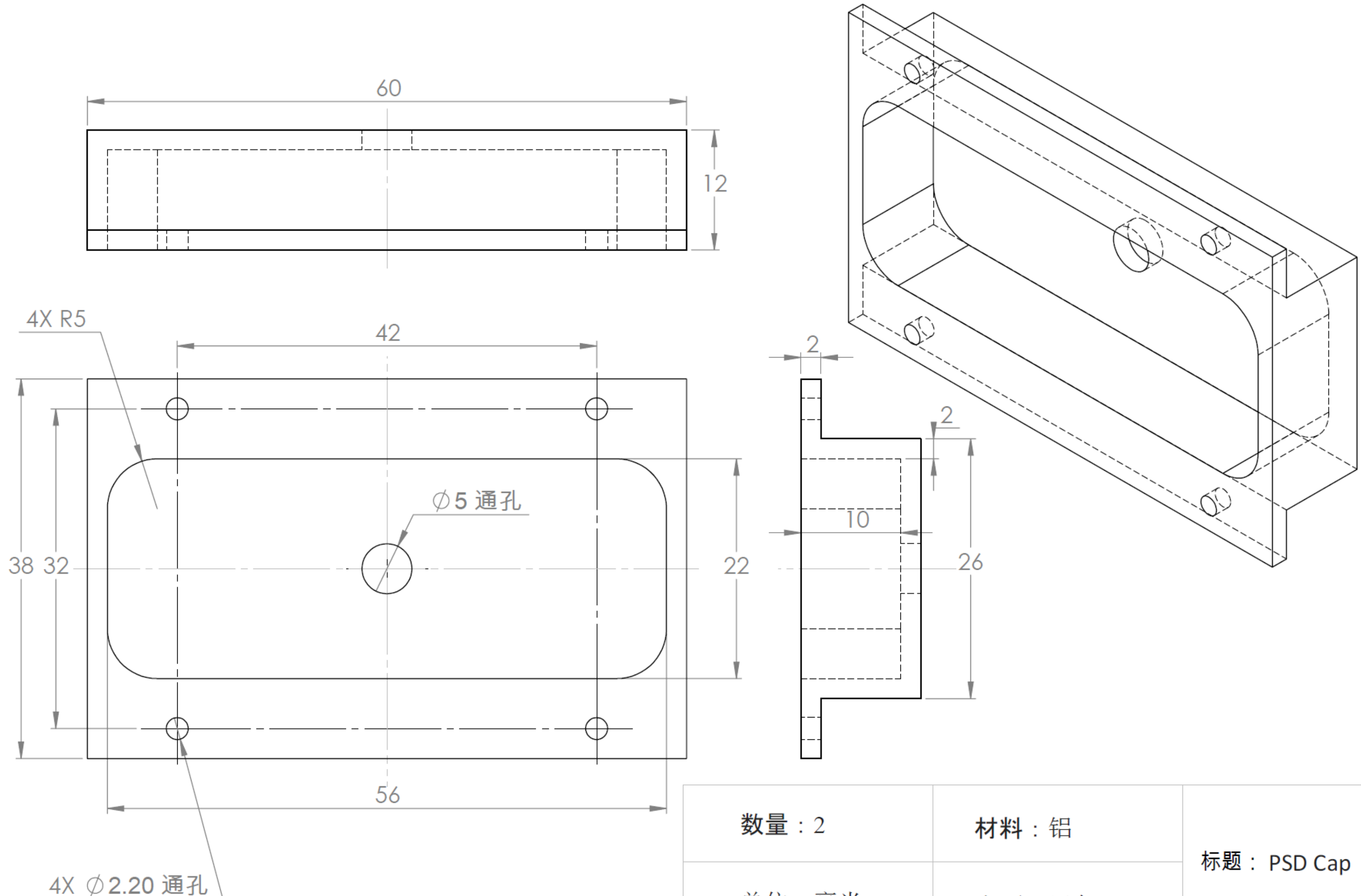

数量：2	**材料**：铝	标题： PSD Cap
单位：毫米	表面：黑色	

Appendix C: Laser Safety Calculations

The scanned pulsed lasers used in this paper have the following parameters:

Wavelength (λ): 850 nm (Infrared)

Pulse frequency (f): 1 kHz

Beam Diameter: ≤ 5 mm

Beam Divergence: ≤ 1.5 mrad

Scan FOV: 30°

Laser Power (P):

1. **Laser 1:** 2-mW
2. **Laser 2:** 20-mW
3. **Laser 3:** 100-mW

Pulse Width (t):

1. **Laser 1:** 170 µs
2. **Laser 2:** 3.2 µs
3. **Laser 3:** 650 ns

The wavelength of 850 nm passes through the ocular media of the eye and is focused into a spot on the retina, potentially resulting in a retinal burn. The worst case scenario assumed is a collimated laser spot being focsed into a small spot on the retina, for an eye accomodated towards infinity. An eye accomodated towards infiintiy focuses the smallest spot on the retina for a collimated lasers, regardless of laser spot size. The worst case limiting aperture size (fully dialated pupil) and aperture distance used for laser safety calculations are 7 mm and 100 mm respectively [72]. The worst case exposure time (T) is 10 seconds for unintentional viewing of near-infrared (700 – 1000 nm) wavelengths [52, 79]. For a laser to be class 1 or 1M, the single pulse energy of the lasers must not exceed the most restrictive limit of the following 3 AEL (Accessible emision limit) criteria [52]:

1. **Single Pulse AEL**
2. **Average single pulse AEL**
3. **Corrected single pulse AEL**

A scanning factor (S) and beam size factior (B) has been considered within calculation using the same methods in [73,80,81].

Only a portion of the laser power is collected by the eye when the laser spot size is larger than the limitng aperture. The beam sizes of all lasers are smaller than the limiting aperture of 7 mm (fully dialated pupil). Therfore 100 % of the single pulse energy enters the pupil, thus B = 1.

The angle of acceptance of a fully dialated pupil (7 mm) at the limiting aperture distance of 100 mm is approxiamtely equal to 4°. The scanning factor (S) is equal to the ratio of the angle of accpetance of a fully dialated pupil and the scanning FOV. Therefore the scanning factor is S = 4°/30° = 0.13.

The single pulse energy (joules) of a laser is calculated by the product of the beam size factor (B), Peak power (P), and pulse width (t), as seen in the following equation,

$$E_{Pulse} = B \cdot P \cdot t \;\; in \;\; Joules \qquad (6)$$

Using Eq.5 the calculated single pulse energies for each respective laser is,

Laser 1: 340 nJ

Laser 2: 64 nJ

Laser 3: 65 nJ

The AEL of a laser is calculated using Table 1 from [72]. The value of C_4 is 1 for small source emittance. The value of $C_6$is 1.995, determined using "Notes to Tables 1-4" from [72] for 850 nm wavelength.

The AEL of a single pulse (Joules) with pulse widths (t) within (18 µs < t ≤ 10 s) are determined using the following equation,

$7 \times 10^{-4}\, t^{0.75} C_4 C_6$ (Joules) (7)

As for pulse widths (t) within (1 ns < t ≤ 18 µs) are determined using the following equation,

$2 \times 10^{-7} C_4 C_6$ (Joules) (8)

Single Pulse AEL calculation (Criteria 1)

Using Eq. 6 for t = 170 µs, the **Single Pulse AEL for Laser 1 is 2.08 µJ**.

Using Eq. 7 for t = 3.2 µs, the **Single Pulse AEL for Laser 2 and Laser 3 is 399 nJ**.

Using Eq. 7 for t = 650 ns, the **Single Pulse AEL for Laser 3 is 399 nJ**.

Average Single Pulse AEL calculation (Criteria 2)

The average single pulse AEL is calculated by finding the AEL for the worst case exposure duration (T = 10 s) and dividing it by the number of pulses (N) the eye is exposed to within that duration.

The number of pulses (N) is calculated using the following equation,

$$N = S \cdot T \cdot f \qquad (9)$$

The number of pulses the eye is exposed to within the worst case exposure time of 10 seconds is 1337 pulses for all lasers.

All lasers are pulsed at the same frequency and associated with a worst case exposure time (T) of 10 s. Therefore, using Eq. 6 and Eq. 8, the **Average single pulse laser AEL for all lasers is 5.87 µJ**.

Corrected Single Pulse AEL calculation (Criteria 3)

The corrected single pulse AEL of a laser is calculated by multiplying the Single Pulse AEL (Criteria 1) by a correction factor $N^{-0.25}$.

The Corrected Single Pulse AEL for each laser is:

Laser 1: 344 nJ

Laser 2: 66 nJ

Laser 3: 66 nJ

Criteria 3 (Corrected single pulse AEL) is most restrictive AEL from the three criteria's tested. Therefore, this limit will be used to compare with the actual single pulse energies of each laser calculated earlier.

Laser 1's single pulse energy of 340 nJ is less than the most restrictive AEL limit of 344 nJ. Therefore, Laser 1 is classed as 1.

Laser 2's single pulse energy of 64 nJ is less than the most restrictive AEL limit of 66 nJ. Therefore, Laser 2 is classed as 1.

Laser 3's single pulse energy of 65 nJ is less than the most restrictive AEL limit of 66 nJ. Therefore, Laser 3 is classed as 1.

The lasers are classed as 1 instead of 1M, since the laser spot sizes are already smaller than the limiting aperture of 7 mm. Therefore, magnifying optics cannot further increase the hazard of the beam.

References

[1] Lepej, P., Lakota, M., & Rakun, J. (2017). Robotic real-time 3D object reconstruction using multiple laser range finders. *Advances in Animal Biosciences*, *8*(2), 183–188.

[2] Roh, H. C., Sung, C. H., & Chung, M. J. (2013). Rapid SLAM using simple map representation in indoor environment. *The 19th Korea-Japan Joint Workshop on Frontiers of Computer Vision*.

[3] Beraldin, J. A., Blais, F., Rioux, M., Cournoyer, L., Laurin, D. G., & Maclean, S. G. (1997). . *Visual Information Processing VI*, 28–46.

[4] The Safety of Controllers, Sensors, and Actuators - Book 5 Automated Vehicle Safety. (2019). doi: 10.4271/9780768002966

[5] Tong, J., Zhou, J., Liu, L., Pan, Z., & Yan, H. (2012). Scanning 3D Full Human Bodies Using Kinects. *IEEE Transactions on Visualization and Computer Graphics*, *18*(4), 643–650. doi: 10.1109/tvcg.2012.56

[6] Scaramuzza, D., Harati, A., & Siegwart, R. (2007). Extrinsic self calibration of a camera and a 3D laser range finder from natural scenes. *2007 IEEE/RSJ International Conference on Intelligent Robots and Systems*, 4164–4165.

[7] Franca, J., Gazziro, M., Ide, A., & Saito, J. (2005). A 3D scanning system based on laser triangulation and variable field of view. *IEEE International Conference on Image Processing 2005*.

[8] Vasconcelos, F., Barreto, J. P., & Nunes, U. (2012). A Minimal Solution for the Extrinsic Calibration of a Camera and a Laser-Rangefinder. *IEEE Transactions on Pattern Analysis and Machine Intelligence*, *34*(11), 2097–2107.

[9] Perrin, S., Cassinelli, A., & Ishikawa, M. (n.d.). Gesture recognition using laser-based tracking system. *Sixth IEEE International Conference on Automatic Face and Gesture Recognition, 2004. Proceedings.*

[10] Jeon, S., Fujita, H., & Toshiyoshi, H. (2015). A mems-based interactive laser scanning display with a built-in laser range finder. *2015 Transducers - 2015 18th International*

Conference on Solid-State Sensors, Actuators and Microsystems (TRANSDUCERS), 859–862.

[11] Jeught, S. V. D., & Dirckx, J. J. (2016). Real-time structured light profilometry: a review. *Optics and Lasers in Engineering*, *87*, 18–31. doi: 10.1016/j.optlaseng.2016.01.011

[12] Konolige, K., Augenbraun, J., Donaldson, N., Fiebig, C., & Shah, P. (2008). A low-cost laser distance sensor. *2008 IEEE International Conference on Robotics and Automation*, 3002–3008.

[13] Wang, R., Li, X., & Wang, S. (2014). A laser scanning data acquisition and display system based on ROS. *Proceedings of the 33rd Chinese Control Conference*, 8433–8437.

[14] Loor, R. D., Penning, L., & Slagle, R. (2014). Polygon Laser Scanning. *Laser Technik Journal*, *11*(3), 32–34.

[15] J. Vrbancich, W. Lieff and J. Hacker, Demonstration of two portable scanning LiDAR systems flown at low-altitude for investigating coastal sea surface topography, Remote Sens., 3 (9) (2011) 1983-2001.

[16] P. A. Hwang, W. B. Krabill, E. J. Walsh and R. N. Swift, Airborne scanning lidar measurement of ocean waves, Nav. Res. Lab. (1999) 2-21.

[17] N. Chen, B. Potsaid, J. T. Wen, S. Barry and A. Cable, Modeling and control of a fast steering mirror in imaging applications, 2010 IEEE International Conference on Automation Science and Engineering, CASE 2010 (2010) 27-32.

[18] Cvecek, K. (2015). Evaluation of Scanner-Based Focus Finding Methods on Rough Surfaces. *Journal of Laser Micro/Nanoengineering*, *10*(3), 304–309. doi: 10.2961/jlmn.2015.03.0012

[19] Ye, L., Zhang, G., & You, Z. (2017). Large-Aperture kHz Operating Frequency Ti-alloy Based Optical Micro Scanning Mirror for LiDAR Application. *Micromachines*, *8*(4), 120.

[20] Zuo, H., & He, S. (2016). FPCB Micromirror-Based Laser Projection Availability Indicator. *IEEE Transactions on Industrial Electronics*, *63*(5), 3009–3018. doi: 10.1109/tie.2016.2516965

[21] Francis, S. (2017, December 5). Suning launches 'basically unmanned' automated warehouse with plans to use 1,000 robots. Retrieved from

https://roboticsandautomationnews.com/2017/12/04/suning-launches-basically-unmanned-automated-warehouse-with-plans-to-use-1000-robots/15272/.

[22] Leap Motion replaces keyboard and mouse with gesture recognition. (n.d.). Retrieved from https://atelier.bnpparibas/en/smart-city/article/leap-motion-replaces-keyboard-mouse-gesture-recognition.

[23] Admin. (2019, August 7). 3D Photogrammetry VS 3D Laser Scanning, Who Wins? Retrieved from https://www.avrspot.com/3d-photogrammetry-3d-laser-scanning/

[24] Laser profilometer / 3d / in-line by EOPTIS Srl: DirectIndustry. (n.d.). Retrieved from https://www.directindustry.com/prod/eoptis-srl/product-159534-1683916.html.

[25] Eep. (2020, January 3). Regular Motor Maintenance To Avoid Failure (and Prolong Its Lifespan). Retrieved from https://electrical-engineering-portal.com/regular-motor-maintenance-to-avoid-failure-and-prolong-its-lifespan.

[26] Holmström, S. T. S., Baran, U., & Urey, H. (2014). MEMS laser scanners: A review. *Journal of Microelectromechanical Systems*, *23*(2), 259–275. https://doi.org/10.1109/JMEMS.2013.2295470

[27] Solgaard, O., Godil, A. A., Howe, R. T., Lee, L. P., Peter, Y. A., & Zappe, H. (2014). Optical MEMS: From micromirrors to complex systems. *Journal of Microelectromechanical Systems*, *23*(3), 517–538. https://doi.org/10.1109/JMEMS.2014.2319266

[28] Georgehelser. (2017, December 31). georgehelser. Retrieved from https://precisionlaserscanning.com/2017/12/mems-mirrors-vs-polygon-scanners-for-lidar-in-autonomous-vehicles/.

[29] SignalTronix. (n.d.). SignalTronix.com Specialty, OEM, Industrial Motion Control, Electro-Optics, Electronics. Retrieved from http://signaltronix.com/.

[30] Galvanometer Optical Scanners Information. (n.d.). Retrieved from https://www.globalspec.com/learnmore/optics_optical_components/optoelectronics/optical_scanners.

[31] Wang, S., Wei, X., Weng, Y., Zhao, Y., & Jiang, Z. (2018). A novel single-axis MEMS tilt sensor with a high sensitivity in the measurement range from 0° to 360°. *Sensors (Switzerland)*, *18*(2). https://doi.org/10.3390/s18020346

[32] Yoo, H. W., Druml, N., Brunner, D., Schwarzl, C., Thurner, T., Hennecke, M., & Schitter, G. (2018). MEMS-based lidar for autonomous driving. *Elektrotechnik Und Informationstechnik*, *135*(6), 408–415. https://doi.org/10.1007/s00502-018-0635-2

[33] Yangyang, W., & Qian, K.-Y. (2019). 2-D Scanning LiDAR with MEMS Mirror and STM32. *IOP Conference Series: Materials Science and Engineering*, *563*, 032051. https://doi.org/10.1088/1757-899x/563/3/032051

Hu, Q., Pedersen, C., & Rodrigo, P. J. (2016). Eye-safe diode laser Doppler lidar with a MEMS beam-scanner. *Optics Express*, *24*(3), 1934. https://doi.org/10.1364/oe.24.001934

[34] C. Da Liao and J. C. Tsai, "The evolution of MEMS displays," IEEE Trans. Ind. Electron., vol. 56, no. 4, pp. 1057–1065, Apr. 2009.

[35] J. Chong, S. He, and R. Ben Mrad, "Development of a vector display sys- tem based on a surface-micromachined micromirror," IEEE Trans. Ind. Electron., vol. 59, no. 12, pp. 4863–4870, Dec. 2012.

[36] L. Li, V. Stankovic, L. Stankovic, L. Li, S. Cheng, and D. Uttamchandani, "Single pixel optical imaging using a scanning MEMS mirror," J. Micromech. Microeng., vol. 21, no. 2, Art. ID 025022, 2011.

[37] F. Chao, S. He, J. Chong, R. Ben Mrad, and L. Feng, "Development of a micromirror based laser vector scanning automotive HUD," in Proc. IEEE Int. Conf. Mechatron. Autom. (ICMA'11), 2011, pp. 75–79.

[38] C. Fan and S. He, "A two-row interdigitating-finger repulsive-torque elec- trostatic actuator and its application to micromirror vector display," J. Microelectromech. Syst., vol. 24, no. 6, pp. 2049–61, Dec. 2015.

[39] Zuo, H., & He, S. (2018). Double stage FPCB scanning micromirror for laser line generator. *Mechatronics*, *51*(March), 75–84. https://doi.org/10.1016/j.mechatronics.2018.03.005

[40] Kaushik, N., Sasaki, T., Nakazawa, T., & Hane, K. (2018). Simple retinal imaging system using a MEMS scanning mirror. Optical Engineering, 57(09), 1. https://doi.org/10.1117/1.oe.57.9.095101

[41] Aoyagi, I., Shimaoka, K., Kato, S., Makishi, W., Kawai, Y., Tanaka, S., … Hane, K. (2011). 2-Axis MEMS scanner for laser range finder. *International Conference on Optical MEMS and Nanophotonics*, 39–40. https://doi.org/10.1109/OMEMS.2011.6031035

[42] Rao, K., Wei, X., Zhang, S., Zhang, M., Hu, C., Liu, H., & Tu, L. C. (2019). A MEMS micro-g capacitive accelerometer based on through-silicon-wafer-etching process. *Micromachines*, *10*(6). https://doi.org/10.3390/mi10060380

[43] V. Milanović, "*Multilevel-Beam SOI-MEMS Fabrication and Applications,*" *IEEE/ASME Journal of Microelectromechanical Systems*, vol. 13, no. 1, pp. 19-30, Feb. 2004.

[44] V. Milanović, D. T. McCormick, G. Matus, "*Gimbal-less Monolithic Silicon Actuators For Tip-Tilt-Piston Micromirror Applications,*" *IEEE J. of Select Topics* in Quantum Electronics, Volume: 10, Issue: 3, May-June 2004, Pages: 462 – 471

[45] Maxplanckpress. (2000, June 26). Why is silicon so brittle? Retrieved from https://www.eurekalert.org/pub_releases/2000-06/M-Wiss-2606100.php.

[46] BRADEN SMITH,* BRANDON HELLMAN, ADLEY GIN, ALONZO ESPINOZA AND YUZURU TAKASHIMA, "Single chip lidar with discrete beam steering by digital micromirror device," OPTICS EXPRESS, Vol. 25, 2017, pp. 1-14

[47] Schlarp, J., Csencsics, E., & Schitter, G. (2019). Optical scanning of a laser triangulation sensor for 3D imaging. *IEEE Transactions on Instrumentation and Measurement*, *XX*(XX), 1–1. https://doi.org/10.1109/tim.2019.2933343.

[48] Mirrorcle Technologiues Inc., https://www.mirrorcletech.com/index.html, browsed on Dec 27, 2019.

[49] Qi, X., Wang, S., Jiang, J., Liu, K., Wang, X., Yang, Y., & Liu, T. (2019). Fiber Optic Fabry-Perot Pressure Sensor with Embedded MEMS Micro-Cavity for Ultra-High Pressure Detection. *Journal of Lightwave Technology*, *37*(11), 2719–2725. https://doi.org/10.1109/JLT.2018.2876717

[50] Groschup, R., & Grosse, C. U. (2015). MEMS microphone array sensor for air-coupled impact-echo. *Sensors (Switzerland)*, *15*(7), 14932–14945. https://doi.org/10.3390/s150714932

[51] Sneak Peak: New Capabilities for Micro Scanning and Projection Mirrors. (2018, August 2). Retrieved from https://www.coventor.com/blog/sneak-peak-new-capabilities-for-micro-scanning-and-projection-mirrors/.

[52] MAR1100 - MEMS 2D LASER SCANNING MIRROR. (2019, December 31). Retrieved from http://www.maradin.co.il/products/mar1100-mems-2d-laser-scanning-mirror/.

[53] Periyasamy, K. G. K., Zuo, H., & He, S. (2019). Flexible printed circuit board magnetic micromirror for laser marking/engraving. *Journal of Micromechanics and Microengineering*, *29*(8), ab1fc1. https://doi.org/10.1088/1361-6439/ab1fc1

[54] Periyasamy, K. G. K., Tan, V. J., He, S., & Kourtzanidis, N. (2019). External Electromagnet FPCB Micromirror for Large Angle Laser Scanning. *Micromachines*, *10*(10), 667. https://doi.org/10.3390/mi10100667

[55] Zuo, H., & He, S. (2017). FPCB ring-square electrode sandwiched micromirror-based laser pattern pointer. *IEEE Transactions on Industrial Electronics*, *64*(8), 6319–6329. https://doi.org/10.1109/TIE.2017.2674594

[56] Pull-in Voltage. (n.d.). Retrieved from https://www.sciencedirect.com/topics/engineering/pull-in-voltage.

[57] Faraday's Experiments and Applications. (n.d.). Retrieved from http://ffden-2.phys.uaf.edu/webproj/212_spring_2017/Sterling_Stasak/Part 2/Physics of Magnets.html.

[58] Tan, V., & He, S. (2019). Electromagnetic FPCB micromirror scanning laser rangefinder. 2019 International Conference on Optical MEMS and Nanophotonics (OMN). Daejeon, Korea.

[59] Static and Dynamic simulations: ANSYS MechanicalWorkbench. 2017. Available online: https://www.ansys.com/products

[60] Laser Gold Spectral Reflectance Graphical Data. (n.d.). Retrieved from https://www.epner.com/processes-and-products/laser-gold/laser-gold-tech-data/reflectivity/laser-gold-spectral-reflectance-graphical-data/.

[61] Solaris. (2017). *American Wire Gauge Conductor Size Table*. *1*, 53–55. Retrieved from http://www.solaris-shop.com/content/American Wire Gauge Conductor Size Table.pdf

[62] Yu, D. Y. W., & Spaepen, F. (2004). The yield strength of thin copper films on Kapton. *Journal of Applied Physics*, *95*(6), 2991–2997. https://doi.org/10.1063/1.1644634

[63] Kapton Characteristics. Available online: https://dielectricmfg.com/knowledge-base/kapton/ (accessed on 19 July 2019).

[64] Schubert, P. J., & Nevin, J. H. (1985). Polyimide-Based Capacitive Humidity Sensor. *IEEE Transactions on Electron Devices*, *ED-32*(7), 1220–1223. https://doi.org/10.3390/s18051516

[65] Dupont. (2012). DuPont ™ Kapton ®. Http://Www.Dupont.Com/Content/Dam/Dupont/Products-and-Services/Membranes-and-Films/Polyimde-Films/Documents/DEC-Kapton-Summary-of-Properties.Pdf, 50, 1–7. Retrieved from http://www.dupont.com/content/dam/dupont/products-and-services/membranes-and-films/polyimde-films/documents/DEC-Kapton-summary-of-properties.pdf%0Ahttp://www.dupont.com/content/dam/dupont/products-and-services/membranes-and-films/polyimde-films/documents/

[66] 1996_-_K_Sager_-_Humiditydependentmechanicalpropertiesofpolyimidefi[retrieved_2019-10-17].pdf. (n.d.).

[67] Cavedo, F., Norgia, M., Pesatori, A., & Solari, G. E. (2016). Steel Pipe Measurement System Based on Laser Rangefinders. *IEEE Transactions on Instrumentation and Measurement*, *65*(6), 1472–1477.

[68] Guidi, G., Russo, M., Magrassi, G., & Bordegoni, M. (2010). Performance Evaluation of Triangulation Based Range Sensors. *Sensors*, *10*(8), 7192–7215.

[69] Range Sensing in Confined Environments. (1999). Sensor Modelling, Design and Data Processing for Autonomous Navigation World Scientific Series in Robotics and Intelligent Systems, 13–39.

[70] Kennedy, W. P. (2016). Optical Triangulation. *Position Sensors*, 335–352.

[71] Pears, N. (1994). Optical Triangulation Range Sensors for Vehicle Manœuvres. *World Scientific Series in Robotics and Intelligent Systems Advanced Guided Vehicles*, 85–106.

[72] Publication, G. S. (2001). Edition 1.2 – Part 1: Equipment classification, requirements and user's guide. 54.

[73] Buckley, E. (2012). Detailed eye-safety analysis of laser-based scanned-beam projection systems. *IEEE/OSA Journal of Display Technology*, *8*(3), 166–173.

[74] *Laser Safety Facts*, https://www.lasersafetyfacts.com/laserclasses.html.

[75] Smith, W. (2001). Aberrations 3.1. *Modern Optical Engineering*, 61–90.https://doi.org/10.1109/JDT.2011.2170955

[76] Costineanu, D., Fosalau, C., Damian, C., & Plopa, O. (2008). Triangulation-based 3D image processing method and system with compensating shadowing errors. *16th IMEKO TC4 Int. Symp.: Exploring New Frontiers of Instrum. and Methods for Electrical and Electronic Measurements; 13th TC21 Int. Workshop on ADC Modelling and Testing - Joint Session, Proc.*, (figure 3), 460–463.

[77] Jeon, S., Fujita, H., & Toshiyoshi, H. (2015). A MEMS-BASED INTERACTIVE LASER SCANNING DISPLAY WITH A BUILT-IN LASER RANGE FINDER Research Center for Advanced Science and Technology , University of Tokyo , Japan Institute of Industrial Science , University of Tokyo , Japan Laser range finder based on . 859–862.

[78] S. Jeon, H. Fujita, and H. Toshiyoshi, "A MEMS Interactive Laser Projection Display with a Built-in Laser Range Finder",in Proceedings of the IEEE Optical MEMS and Nanophotonics 2013, Kanazawa, Japan, August 18-22, 2013, pp. 15-16.

[79] Health, E. (2007). Laser Safety Training Guide. *Environmental Health and Safety*, (September). Retrieved from http://www.princeton.edu/ehs

[80] Bronzi, D., Zou, Y., Villa, F., Tisa, S., Tosi, A., & Zappa, F. (2016). Automotive Three-Dimensional Vision through a Single-Photon Counting SPAD Camera. *IEEE Transactions on Intelligent Transportation Systems*, *17*(3), 782–795. https://doi.org/10.1109/TITS.2015.2482601

[81] Velodyne. (2007). *Hdl ^{TM} - 64e, RESOURCE MANUAL, Laser Safety Parameters*.